Master's thesis

NTNU
Norwegian University of Science and Technology
Faculty of Engineering
Department of Energy and Process Engineering

Sander Kynell Arstad

Digital Twin - Transient Flow Conditions

Master's thesis in Mechanical Engineering
Supervisor: Lars Eirik Bakken
Co-supervisor: Erik Langørgen
June 2022

NTNU
Norwegian University of
Science and Technology

Sander Kynell Arstad

Digital Twin - Transient Flow Conditions

Master's thesis in Mechanical Engineering
Supervisor: Lars Eirik Bakken
Co-supervisor: Erik Langørgen
June 2022

Norwegian University of Science and Technology
Faculty of Engineering
Department of Energy and Process Engineering

NTNU
Norwegian University of
Science and Technology

Preface

I would like to to thank my supervisor, Lars Eirik Bakken for guiding me through this thesis, with a ready smile and an open door at all times. I would also like to thank Erik Langørgen, my co-supervisor, and senior engineer at the NTNU laboratory for his indispensable help and experience in conducting the experiments.

Finally, I would like to thank my fellow students, “the lads”, for the exciting sessions we had together.

Abstract

A Digital Twin is a relatively new concept, requiring a lot of effort, but with promises of great rewards in terms of sustainability and profits. NTNU's turbomachinery research department is slowly building up their own digital twin for their full-scale single-stage centrifugal compressor. Work towards this ambition has been ongoing for years, and this thesis is part of that work.

Focusing on providing experimental data, essential for further development on the current digital model, the primary objective of this thesis has been to develop a compressor curve covering a wide range, which the digital model can be modeled after. To ensure the validity of such a curve, secondary objectives with focus on ensuring the legitimacy of the results were also developed.

Through a series of static and dynamic experiments, the primary objective, and all secondary objectives have been met. In addition, multiple other conclusions important for further development and experimentation have been drawn. Briefly summarised: the downstream pressure tank is an essential part of the compressor system, when experimenting with flows lower than $Q < 0.5\,\mathrm{m}^3/\mathrm{s}$; the two orifices installed at the laboratory mostly match each other well, but not near zero flow; uncertainties make it so that measurements taken within $Q \in (-0.2, 0.2)\ \mathrm{m}^3/\mathrm{s}$ can only be considered suggestive; with the current setup, it is not possible to use the differential pressure over the compressor bull-nose to measure anything meaningful; logging frequency should be at least $10\,\mathrm{Hz}$ for experiments where $Q < 0.5\,\mathrm{m}^3/\mathrm{s}$; certain areas with low response have little to no impact on the compressor map-curves; and finally, it could be beneficial to reduce the length of the differential pressure tubes.

The experiments presented in this thesis were explicitly conducted using the "compressor test-rig" at the turbomachinery laboratory at NTNU. Matlab was used to interpret the results from those experiments, and extensive effort has gone into creating near-automatic scripts. A short uncertainty analysis of Type B was also orchestrated, to help with the legitimacy of the results.

Sammendrag

En digital tvilling er et relativt nytt konsept. Det er noe som krever mye innsats, men med løfter om store belønninger både med tanke på bærekraft og fortjeneste. NTNUs forskningsavdeling for turbomaskineri bygger sakte opp sin egen digitale tvilling for sin fullskala ett-trinns sentrifugalkompressor. Arbeidet mot denne ambisjonen har pågått i årevis, og denne oppgaven er en del av det arbeidet.

Med fokus på å dokumentere eksperimentelle data, som er avgjørende for videre utvikling av dagens digitale modell, har hovedmålet med denne oppgaven vært å utvikle en kompressorkurve som dekker et bredt spekter. Noe den digitale modellen kan modelleres etter. For å sikre gyldigheten av en slik kurve ble det også utviklet sekundære mål hvis formål var å sikre resultatenes legitimitet.

Gjennom en rekke statiske og dynamiske eksperimenter har hovedmålet og begge sekundære mål blitt oppfylt. I tillegg har flere andre konklusjoner som er viktige for videre utvikling og eksperimentering blitt trukket. Kort oppsummert: trykktanken nedstrøms kompressoren er en viktig del av systemet når man eksperimenterer med strømninger lavere enn $Q < 0.5\,\mathrm{m}^3/\mathrm{s}$; de to "orifice"-platene installert på laboratoriet samsvarer stort sett med hverandre godt, men ikke nær nullstrøm; usikkerheter gjør at målinger tatt innenfor $Q \in (-0.2, 0.2)\ \mathrm{m}^3/\mathrm{s}$ bare kan betraktes som pekepinner, og ikke "sikre sannheter"; med det nåværende oppsettet er det ikke mulig å bruke differensialtrykket over kompressorens "bull-nose" for å måle noe meningsfullt; loggingsfrekvensen bør være minst $10\,\mathrm{Hz}$ for eksperimenter der $Q < 0.5\,\mathrm{m}^3/\mathrm{s}$; visse områder med lav respons har liten eller ingen innvirkning på kompressorkartkurvene; og til slutt, det kan være fordelaktig å redusere lengden på rørene til differensialtrykkmålerne.

Eksperimentene som presenteres i denne oppgaven ble kun utført ved bruk av "kompressor-testriggen" ved turbomaskin-laboratoriet ved NTNU. Matlab ble brukt til å tolke resultatene fra disse eksperimentene, og mye arbeid er lagt i å lage kodene nesten helt automatiske. En kort usikkerhetsanalyse av "Type B" ble også gjennomført for å hjelpe med legitimiteten til resultatene.

Contents

List of Tables

List of Figures

Nomenclature

Table 1: List of symbols and abbreviations

Symbol	Unit	Elaboration
C		Variable/Unknown
D	$[\mathrm{m}]$	Outer/larger diameter
H	$[\mathrm{J/kg, J}]$	Head OR Enthalpy
P	$[\mathrm{kW}]$	Power
Q	$[\mathrm{m^3}]/\mathrm{s}$	Volumetric flow rate
R	$[\mathrm{J}/(\mathrm{kg\ K})]$	Specific Gas Constant
T	$[\mathrm{K}]$	Temperature
Z	$[-]$	Compressibility factor
c	$[\mathrm{m/s}]$	Absolute velocity
f	$[-]$	Friction factor OR Correction factor
h	$[\mathrm{j/kg}]$	Specific enthalpy
m	$[\mathrm{kg}]$	Mass
$\dot{m}$	$[\mathrm{kg/s}]$	Mass flow rate
p	$[\mathrm{N/m^2, Pa}]$	Pressure
r	$[\mathrm{m}]$	Radius
v	$[\mathrm{m^3/kg}]$	Specific volume
w	$[\mathrm{m/s}]$	Relative velocity
ϵ	$[\mathrm{m}]$	(Pipe) Roughness
η	$-$	Efficiency
κ	$-$	Isentropic exponent
μ	$[\mathrm{kg}/(\mathrm{m\ s})]$	Dynamic Viscosity
ν	$[\mathrm{m^3/kg}]$	Specific volume
ρ	$[\mathrm{kg/m^3}]$	Density
τ	$[\mathrm{Nm}]$	Torque
ω	$[\mathrm{rad/s}]$	Rotational speed

Subscript	Unit	Elaboration
1		Inlet
2		Outlet
s		Isentropic
A		Condition A/Operation point A
B		Condition B/Operation point B
$Const$		Constant (factor)
Lin		Linear (factor)
$Or1$		Orifice 1
$Or2$		Orifice 2
θ		Circumferential direction

Abbreviation	Unit	Elaboration
CFD		Computational Fluid Dynamics
DCS		Distributed Control System
DP		Differential Pressure
DV		Discharge Valve
EOS		Equation(s) of State
GMF		Gas Mass Fraction
LHS		Left Hand Side
OP		Output
PID		Proportional- Integral- Derivative
Pos.		Position
PV		Process Variable
reg.curve		Regression Curve
RPM		Rounds Per Minute
SP		Setpoint
Th.dyn.Eq		Thermodynamic Equilibrium

1. Introduction

The intention of this thesis is to continue the previous work at NTNU of creating a digital twin of the centrifugal compressor in the NTNU wet gas compressor laboratory. This target is met by providing more experimental data, particularly of the compressor surge region. All of the experimental research presented in this thesis is obtained from the single-stage centrifugal compressor at NTNU, operating on air near atmospheric conditions.

This chapter provides the background for the thesis and describes the motivation, as well as presenting the scope of the work and the structure of the thesis.

1.1 Background

Mankind's society has always been completely dependant on its energy supply. Until the invention of the steam engine in the 18th century, this energy supply has been limited to mostly manual labour, apart from some relatively simple machines. With the advent of the steam engine, mankind was no longer reliant on muscles to do work, and societal productivity exploded as a consequence [1]. Today, the many environmental challenges that came as an aftermath of that explosion of productivity is a huge issue mankind is still struggling with, leading to a substantial pressure in the energy-sector to become more energy efficient, and more environmental-friendly. Even though many new technologies have been invented, most energy sources are still highly dependant on the expansion and compression of fluids. For many of these sources, the centrifugal compressor is a vital component.

Centrifugal compressors are expensive to build and maintain, but are nonetheless an essential component of the modern energy industry. Therefore, it is only natural that these components are constantly being examined for ways to make them more efficient. One way, is by digitising the compressor system, enabling remote- and sub-sea operation. Sub-sea operations prolong the service life of existing platforms substantially, since they need a lower reservoir pressure to operate, compared to conventional methods [2]. As an example, the Åsgard field's productive life is expected to increase by 15 years, following Equinor's installation of sub-sea compressors [2]. Because producing oil and gas from existing fields is cheaper, associated with less risk, and is more environmental-friendly than restarting on a new field, extending the productive life of a reservoir is one way to reduce environmental impact in the oil and gas sector. Therefore, even though digital monitoring and control has been used to operate a centrifugal compressor since the 1980's, digital models and simulations continue to be vital to regular operation of compressor systems [3], and advancing development of digital tools continues. NTNU is among those who continue to experiment and develop some of these tools.

The latest idea in this endeavour, is NTNU's attempts to create a Digital Twin – a high-fidelity digital model, a direct copy of the physical entity, capable of reporting current conditions; predicting scenarios, and likely outcomes of an action; and automatically operate, and implement situational changes to the physical compressor, to achieve a target set by an operator. The work in this thesis is one step – not the first, nor will it be the last – in a larger march towards this end goal. A complete digital twin. It is with this goal in mind that the scope of the work has been defined.

1.2 Scope of work

Initially, the main goal of the thesis was to document and validate the digital twin transient model's ability to replicate transient responses. The current digital model/"twin" is created in HYSYS dynamics, a simulation software provided by AspenTech. To some degree, this model has already been examined in Arstad's project work [4]. But, in order to do a more substantial documentation, access to the source code is needed, because the model has not been updated since the aforementioned project work was written. For various reasons, it was not possible to gain access to the source code for this thesis. Therefore, the main goal was changed in concurrence with the supervisor to focus on experimental research. Thereby, contributing to the development of the dynamic simulation tool by providing experimental data instead.

To this end, the main goal of this experimental work is the following:

- Create a complete, continuous compressor curve from negative flow to compressor-choke.

The primary objective is quite explicit, and leaves little room for interpretation. In order to ensure the validity of the compressor curve (if it is created), two secondary objectives were defined as well, in accordance with the supervisor. These two secondary objectives must be completed alongside the primary objective. They are:

1. Evaluate recommendations and standards for flow measurements at transient conditions.
2. Utilise the compressor test-rig to validate transient flow measurements.

While these two secondary objectives might sound similar at first, they are separate, and can be reached independently. The first of these secondary objectives is interpreted to mean that standards for flow measurements should be examined, with particular focus on how their transient response is across the region examined for the primary objective. That means for regular operation, reduced flow, and reversed flow. The second of the secondary objectives is interpreted to mean that different measurements taken during transient flow conditions must be validated. This will be achieved through a combination of an uncertainty analysis, some comparison to previous experiments, and regular analysis of both static and dynamic flows.

1.3 Thesis structure

The thesis is divided into different chapters. Each chapter focuses on a specific topic, described shortly below. Because this thesis builds on the preceding project work (found here [4]), some parts relevant for both have been copied to this thesis from the project work without being altered. This was done with the supervisors permission. Other parts have been altered, but most of this thesis is original. The parts that have been copied or altered will be mentioned below, and in the introduction to the relevant sections.

Chapter 1 – Introduction Introduces the thesis, its motivation, scope, and structure.

Chapter 2 – Theory Provides some relevant background theory. section 2.1 is unchanged from the project work, section 2.2 is mostly unchanged, while the rest of the chapter is original to this thesis.

Chapter 3 – NTNU Testing Facility Describes the setup at the laboratory at NTNU, available equipment, how ISO5167 was used experimentally, and how Matlab was used to interpret the results. Section 3.1 contains some parts from the project work, but is mostly original to this thesis. Section 3.3 has been updated, but still share many similarities with the Project Work. The rest is new.

Chapter 4 – Uncertainty Analysis Goes beyond the theory and details specifically how the uncertainty analysis was completed. Little explicit results are given here, because most depend on experimental conditions.

Chapter 5 – Experimental Campaign Describes all the experiments made, the type of dynamic experiment made, and defines some flow regions.

Chapter 6 – Results and Discussion Contains the results and discussion. Herein the static experiments, the dynamic experiments, combined experiments, and the results of the uncertainty analysis.

Chapter 7 – Conclusion Concludes the document.

Bibliography Includes the bibliography.

Appendices Includes all appendices for this thesis. Structured as best as possible.

2. Theory

In this chapter, fundamental theory needed to operate the current digital model is presented. Some basic compressor theory including Schultz, and how to calculate mass flow in a pipe using an orifice plate. This is not meant to be a complete summary of all theory necessary in turbomachinery. Additionally, some general theory about uncertainty analysis, and a part about the significance of thermal equilibrium is included in this chapter.

2.1 Centrifugal Compressor theory

As the compressor in the NTNU-test rig is a centrifugal compressor, only centrifugal compressors will be the focus of this document. The following section will give a concise description of such a compressor, along with some theory mainly focused on polytropic analysis and affinity laws.

Centrifugal compressors are compressors that use centrifugal forces to increase the pressure of a fluid. A schematic of a centrifugal compressor can be found in Figure 2.1. The rotating part of the compressor is called the *impeller*, and it is followed by a *diffuser*. The compressor's purpose is to increase pressure, and therefore the energy of the flow. To achieve this, the impeller accelerates the flow by spinning it outwards, increasing the angular momentum of the fluid and static pressure. It works by dragging fluid through the *eye* of the impeller, and into the *inducer section* where the velocity of the flow is increased. At the inlet of this section, the flow has a relative velocity w_1 at angle β_1 to the angle of rotation. Though there is no clear, distinct border where the inducer section ends, it is often said to end where the flow starts to turn into the radial direction. Bordering the flow along the curved surface $a - b$ in Figure 2.1, is the *hub*. On the opposite side of the flow, along the surface $c - d$ is the *shroud*. Exiting the impeller, the flow is very kinetic. The diffuser converts this kinetic energy into potential energy by decreasing the velocity of the flow, accomplishing this typically through diffuser vanes, or by free diffusion. [5]

Power P, delivered by centrifugal compressors – or alternatively, the rate at which work is done upon the fluid, by the impeller running at angular velocity ω – is given in Equation 2.1a.

$$P = \dot{W}_{compressor} = \tau\ \omega = \dot{m}\ (U_2\ c_{\theta 2} -\ U_1\ c_{\theta 1}) \tag{2.1a}$$

Making the specific work (work done on every unit mass of fluid):

$$\frac{P}{\dot{m}} = \frac{\dot{W}_{compressor}}{\dot{m}} = H = U_2\ c_{\theta 2} -\ U_1\ c_{\theta 1} > 0 \tag{2.1b}$$

Equation 2.1b is also known as *Euler's pump, or compressor equation*. Since $U = \omega\ r$, increasing the difference between the entry-radius r_1, and the exit-radius r_2 will increase the work done on the fluid by the compressor. This reveals a great advantage centrifugal compressors have over other types of compressors. While for example axial compressors can only increase the circumferential velocity c_θ, centrifugal compressors can increase circumferential velocity *and* rotational radius to increase the work done by a single stage.

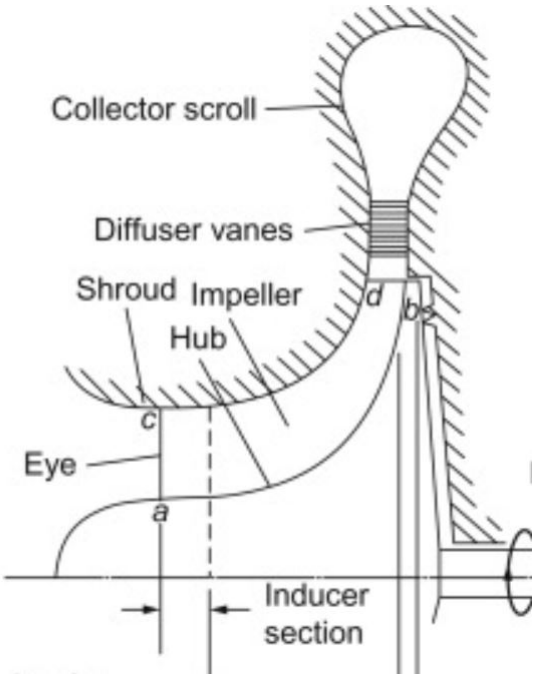

Figure 2.1: Centrifugal compressor stage schematic. From Dixon [5].

If the compressor is fitted with a torque meter – a device for measuring torque – it is possible to calculate the head in two different ways, as Equation 2.1a and Equation 2.1b show. This can be of great help to validate any results.

2.1.1 Performance Analysis

When analysing the performance of a centrifugal compressor, one can either choose an isentropic approach, or a polytropic approach. In this paper, focus will be put on the polytropic analysis as it makes for easier relation of test results from one compressor to other compressors, or from one fluid medium to other fluid mediums. This relationship between isentropic and polytropic analysis is explained in Schultz. [6]

Polytropic Analysis

Polytopic compression is the sum of infinitesimal isentropic compression steps along the actual compression path determined by the compressors efficiency. Equation 2.2 expresses the gradient of isobars, and it clearly shows that isobars diverge with increasing temperature. Figure 2.2 illustrates this phenomenon, where the upper isobaric line has a much steeper gradient than the lower one. It should be noted that real isobars will not be linear in an entropy-enthalpy diagram as Figure 2.2 might suggest. [7, 6]

$$\left(\frac{\delta h}{\delta s}\right)_p = T \tag{2.2}$$

Because of these two factors; isobars diverge with increasing temperature, and polytropic compression being the sum of infinitesimal isentropic compression steps along the actual compression path, the polytropic head will always be larger than the isentropic head for a compression process. Additionally,

because thermodynamic properties are altered along the path, the polytropic process will relate relatively better to the actual process when these variations are big, or when the path is long. [7, 6]

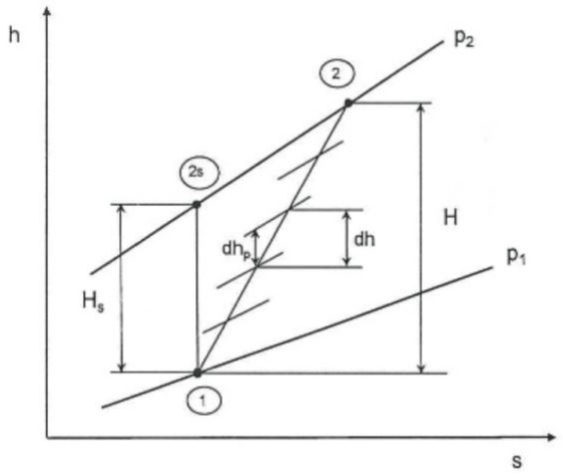

Figure 2.2: Compression process, from Bakken [7]

Figure 2.2 shows how isentropic and polytropic compression processes relate. H_s is the isentropic head, $H_p = \sum dh_p$ is the polytropic head, while $H = \sum dh$ is the actual head. The polytropic process follows the real compression process quite closely, compared to the isentropic process, but it is still significantly less than the actual head.

With constant efficiency, the generalised polytropic process is defined in Equation 2.3;

$$p\, v^n = const \tag{2.3}$$

However, to properly calculate performance for real gas behaviour, one must use the *polytropic volume exponent*, n_v instead. This exponent brings some real gas behaviour into the calculations when utilising basic pressure-volume relationships. At constant efficiency, the polytropic volume exponent is derived from Equation 2.3 [7, 6];

$$\begin{aligned} p\, v^{n_v} &= const \\ \iff \ln p + n_v\ \ln v &= const \\ \implies n_v &= -\frac{d(\ln p)}{d(\ln v)} \\ &= -\frac{v}{p}\left(\frac{\delta p}{\delta v}\right)_{\eta_p} \end{aligned} \tag{2.4}$$

So if one may assume the efficiency is constant from suction to discharge, and with known suction and discharge conditions, Equation 2.4 may be written as Equation 2.5;

$$n_v = \frac{\ln \frac{p_2}{p_1}}{\ln \frac{v_1}{v_2}} \tag{2.5}$$

where subscript 1 and 2 refers to inlet and outlet, respectively, p is the pressure, and v the specific volume.

Since the polytropic (volume) exponent varies throughout the compression cycle, an exact analytical

solution of polytropic head is impossible. If it is assumed constant, it is possible to solve the polytropic head equation given in Equation 2.6, below. [7, 8]

$$H_p = \int_1^2 v\, dp \quad \approx \frac{n_v}{n_v - 1} \left[p_2 v_2 - p_1 v_1 \right] \tag{2.6}$$

But because of this assumption, the solution will only ever give an approximate solution of the integral. To make the approximation better, one might, as proposed by Schultz, multiply it with a correction factor.

Similar to the manner in which this polytropic head is approximated, the isentropic head is also approximated. So similar, in fact, that the same correction factor, f is introduced in polytropic calculation of head as well. For more information about this correlation it is referred to Schultz [6] where it is explained in detail. The *polytropic head factor*, as Schultz calls it, is given by Equation 2.7.

$$f = f_s = \frac{h_{2s} - h_1}{\frac{\kappa_v}{\kappa_v - 1} \left[p_2 v_{2s} - p_1 v_1 \right]} \tag{2.7}$$

where subscript $2s$ refers to isentropic values at level 2, and h is specific enthalpy. By also introducing $p\, v = Z\, R\, T$ and Equation 2.3, the head may be calculated by Equation 2.8;

$$H_p \approx f\, \frac{n_v}{n_v - 1}\, \frac{Z\, R_0\, T}{MW} \left[\left(\frac{P_2}{P_1} \right)^{\frac{n_v - 1}{n_v}} - 1 \right] \tag{2.8}$$

It should be noted that the polytropic head factor usually accounts for a 0.1-0.5% change in H_p. [6]

Affinity laws

Affinity laws relate the covariance of rotational speed (ω), head (H), volumetric flow rate (Q), and power (P). The affinity laws, sometimes called fan laws, enables the creation of multiple compressor curves for one compressor if one curve has been found. Alternatively, it is possible to create a new performance curve in one compressor, by comparing it to a single curve in another dynamically similar compressor with the same impeller diameter. It should be noted that a prerequisite of using the affinity laws is that the compressor efficiency remains constant [9]. If the impeller diameter is kept constant, the affinity laws can be stated as the following relations:

$$\frac{Q_A}{Q_B} = \frac{\omega_A}{\omega_B} \tag{2.9a}$$

$$\frac{H_A}{H_B} = \left(\frac{\omega_A}{\omega_B} \right)^2 \tag{2.9b}$$

$$\frac{P_A}{P_B} = \left(\frac{\omega_A}{\omega_B} \right)^3 \tag{2.9c}$$

where subscripts A and B refer to an arbitrary operation point A and B upon which the analysis is based.

It is emphasised that these are not always true; some deviations will occur, as Ueland found in his studies [10]. They should be considered more as guidelines than actual laws. But, as they mostly are a good indicator, and easy to use, HYSYS also uses these to some extent [11].

Many other curves may be calculated using the main compressor curve that is the focus of this thesis, by using affinity laws. Thus, by only plotting one curve, the entire region could be covered, though affinity laws are, as mentioned, not always true.

2.1.2 Compressor Operation

A compressor is a component of a larger system with valves, separators, and tubes to connect it all. Many more components than mentioned are typical, and in one way or another, they all interact with each other. The performance of the compressor for instance, is closely linked with the upstream and downstream conditions. Figure 2.3 shows where the performance curve meets the system resistance curve; consequently determining the operating point of the compressor. Changing conditions slightly will move the system resistance curve, and given that the compressor speed remains constant, the operating point will shift along the operation line.

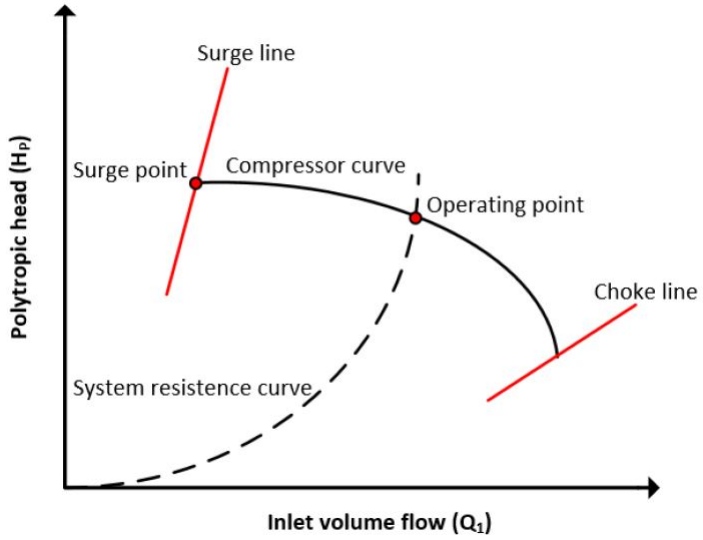

Figure 2.3: Showing a performance curve of a compressor in operation in a system. Operating point is determined by the crossing of the system resistance curve, and the compressor operation curve, called *compressor curve* in the figure, for a given compressor RPM. Figure borrowed from Randen [12].

Compressor Choke

If the volume flow steadily increases, it will lower the pressure delivered by the compressor until the *choke line* is reached. At this point, it is physically impossible to increase the flowrate any further, because somewhere the flow has reached sonic speeds. To reach this condition by only operating the compressor and its associated valves is not easy, as the pressures in the process volumes downstream the compressor also determines the exit pressure of the compressor. In order to move towards the choke

line, more volume needs to be pressurised at an altogether lower pressure. Pressure must first decrease downstream the compressor through other processes. When the downstream pressure is decreased, the operating point will move towards the choke line, as the compressor will force more volume flow through to compensate for the lack of back pressure. If the downstream pressure is not decreased, the operating point will not move towards the choke line, demonstrating that the system resistance curve is aptly named. [12, 5]

Compressor Surge

Opposite from the choke line is the Surge line. Surge occurs when the flow through the compressor is too low, or when the delivered head required becomes too high. Avoiding surge is also about controlling the system resistance (if compressor speed is maintained). Contrary to choke, surge is not at all difficult to achieve. If the compressor is operating near the surge line due to process demand, a slight increase in downstream pressure, like a small closing of the discharge valve can send the compressor spiralling into surge, because the compressor is unable to match the pressure level. [12, 13]

Surge is usually classified in two classes depending on the severity. The least severe kind is called a mild surge. Mild surge is generally detailed by a complete loss of flow rate, and a severe reduction in delivered head, but noteworthy no reversal of flow. The other kind is called deep surge, and is the same as mild surge, along with a complete reversal in flow. If nothing is done, flow will be reversed until the pressure across the compressor has been equalised. When this happens, the compressor will begin to build a pressure difference again and return to the same point where the conditions caused the flow to reverse. The compressor will keep pulsating back and forth rapidly and aggressively unless the governing operating mechanisms intervene. Either by shutting it down, or lowering the pressure difference in the system. If a compressor reaches deep surge, it may receive substantial mechanical damage. Avoiding surge is an important aspiration for any process involving a centrifugal compressor. [13]

2.2 Mass flow

Mass flow cannot be measured directly in any practical way. It is not possible to measure it with a weight-scale and a stop-watch. Instead, mass flow has to be measured indirectly. According to the ISO-standard NS-EN ISO 5167-2:2003 [14], mass flow can be calculated by measuring a pressure difference in the flow over a known geometry.

This section will detail how ISO 5167 measures mass flow through an orifice.

2.2.1 Orifice

An orifice is a very simple device for measuring mass flow. Even though many different types of orifices exist, they are quite similar in operation and mass flow calculations. The main difference between all the types is where the pressure measurements are taken. At the NTNU facility, the orifice is constructed with so-called *corner taps* (pressure is measured at the base of the flange).

According to the NS-EN ISO 5167-2:2003 standard [14], mass flow through an orifice is calculated by Equation 2.10.

$$\dot{m} = \frac{C}{\sqrt{1-\beta^4}}\,\epsilon\,\frac{\pi}{4}\,d^2\,\sqrt{2\Delta p \rho_1} \tag{2.10}$$

where C is the discharge coefficient given by (2.11), β is the diameter ratio given by $\beta = \frac{d}{D}$, where d is the smaller diameter of the orifice plate, and D is the larger diameter of the pipe, ϵ is the expansion factor given by Equation 2.13, $\Delta p = p_1 - p_2$ is the differential pressure across the plate, and ρ_1 is the upstream density, preferably calculated by $\rho_1 = \frac{p_1}{Z_1\,R\,T_1}$.

$$\begin{aligned} C = {} & 0.5961 + 0.0261\beta^2 - 0.216\beta^8 + 0.000521\left(\frac{10^6\beta}{\mathrm{Re}_D}\right)^{0.7} \\ & + (0.0188 + 0.0063\mathrm{A})\beta^{3.5}\left(\frac{10^6}{\mathrm{Re}_D}\right)^{0.3} \\ & + (0.043 + 0.080e^{-10\,L_1} - 0.123e^{-7\,L_1})\,(1 - 0.11\mathrm{A})\,\frac{\beta^4}{1-\beta^4} \\ & - 0.031(M_2' - 0.8M_2'^{1.1})\beta^{1.3}, \end{aligned} \tag{2.11}$$

In Equation 2.11, L_1 is the distance to the upstream tap, and M_2' is the distance to the downstream tap. For more detailed information about how these measurements are to be taken, it is referred to the standard [14]. Additionally in Equation 2.11, Re_D is the Reynolds number based on to the pipe diameter D and pipe flow velocity v given below, and A is given by Equation 2.12;

$$Re_D = \frac{D\,v}{\nu} = \frac{D\,v\,\rho}{\mu}$$

$$A = \left(\frac{19000\,\beta}{\mathrm{Re}_D}\right)^{0.8} \tag{2.12}$$

$$\epsilon = 1 - (0.351 + 0.256\beta^4 + 0.93\beta^8)\,\left[1 - \left(\frac{p_2}{p_1}\right)^{\left(\frac{1}{\kappa}\right)}\right] \tag{2.13}$$

If the orifice is constructed with corner taps, which is the case for the orifice plate in use at NTNU, $L_1 = M_2' = 0$. Equation 2.11 then simplifies to Equation 2.14 below.

$$\begin{aligned} C = {} & 0.5961 + 0.0261\beta^2 - 0.216\beta^8 + 0.000521\left(\frac{10^6\beta}{\mathrm{Re}_D}\right)^{0.7} \\ & + (0.0188 + 0.0063\mathrm{A})\beta^{3.5}\left(\frac{10^6}{\mathrm{Re}_D}\right)^{0.3} \end{aligned} \tag{2.14}$$

After calculating mass flow using Equation 2.10, volumetric flow is calculated with Equation 2.15.

$$Q = \frac{\dot{m}}{\rho} \tag{2.15}$$

2.3 Uncertainty analysis

Correct and accurate measuring during any experiment should not be taken lightly. The experiment is only as reliable as the most unreliable data obtained during it. While that might be enough of a challenge in steady state experiments, transient experiments require a little more of the equipment. Not only must the sensors have a high enough resolution to record small differences, and be accurate enough to record these reliably; the sensors must also have a fast enough response time to register the transient fluctuations.

A brief review of the measuring equipment used during the experiments in this thesis will be presented in this section. The theory is based on the following sources: [15, 16, 17].

2.3.1 Basic definitions

Equation 2.16 is used to determine the quantity Y (called the *measurand*) being measured. It expresses that the measurand is not determined directly, but by an N number of other quantities $X_1, X_2, \ldots, X_N$ through a functional relationship f. This relationship is called the *measurement equation*.

$$Y = f(X_1, X_2, \ldots, X_N) \tag{2.16}$$

All X_i quantities that contribute to a significant uncertainty should be found in the measurement equation f. Additionally, these quantities should include different sources of variability, such as different instruments, relevant correction factors, et cetera.

When the appropriate equations have been considered, an estimation y may be made for Y, using input estimations $x_1, x_2, \ldots, x_N$ for the input quantities $X_1, X_2, \ldots, X_N$, yielding the relation seen in Equation 2.17.

$$y = f(x_1, x_2, \ldots, x_N) \tag{2.17}$$

The uncertainty of the estimated result y is a result of the uncertainties inherent in the input estimates $u(x_i)$. And so, the standard uncertainty $u(y)$ of y is directly dependant on the variation of the input quantities. The standard uncertainty $u(y)$ is also the estimated standard deviation of y. Based on a first-order Taylor series approximation of Equation 2.16, the combined variance $u_c^2(y)$ can be calculated with Equation 2.18. This equation is also called *the law of propagation of uncertainty*.

$$u_c^2(y) = \sum_{i=1}^{n} \left(\frac{\partial f}{\partial x_i} \right)^2 u^2(x_i) + 2 \sum_{i=1}^{N-1} \sum_{j=i+1}^{N} \frac{\partial f}{\partial x_i} \frac{\partial f}{\partial x_j} u(x_i, x_j) \tag{2.18}$$

The partial derivatives of f with respect to x_i are called *sensitivity coefficients*.

If all input quantities are independent, the law of propagation of uncertainty can be reduced to Equation 2.19. And by taking the positive square root of the combined variance $u_c^2(y)$, the combined standard uncertainty $u_c(y)$ can be found. Given that the input quantities are independent, combined standard uncertainty is thus found by Equation 2.20.

$$u_c^2(y) = \sum_{i=1}^{n} \left(\frac{\partial f}{\partial x_i} \right)^2 u^2(x_i) \tag{2.19}$$

$$u_c(y) = \sqrt{\sum_{i=1}^{n} \left(\frac{\partial f}{\partial x_i} \right) \, u^2(x_i)} \tag{2.20}$$

Albeit combined standard uncertainty u_c is very helpful for expressing many measurement results, some applications require a span in which the measurand Y can be comfortably asserted to lie. *Expanded uncertainty* U is the measure of uncertainty used to indicate this span, and is obtained by Equation 2.21.

$$U = k \, u_c(y) \tag{2.21}$$

where k is the *coverage factor*. The coverage factor is determined by the distribution and level of confidence linked to the span. Thus, it is believed with k level of confidence that $Y = y \pm U$. In other words, the chance that Y is within the interval generated by $y \pm U$, where y is the estimation of Y, and U is the expanded uncertainty.

2.3.2 Type B analysis

Type B analysis involves defining some variation limits, and looking for a distribution between those limits. Based on the type of distribution and on the variation limits, an uncertainty analysis is made. Since no measurements are without error, it is impractical – and often quite unnecessary – to find the actual value of a certain measurement. It is instead more efficient to operate with confidence intervals. Confidence intervals give a certain confidence that the actual value is within the given interval. When a level of confidence is selected, all uncertainties must be determined at the same level of confidence.

Based on industry practices [18, 19, 20], selecting $95\,\%$ as the level of confidence for this thesis is appropriate. With an assumption that all distributions are normal distributions, such a confidence-level results in a coverage factor of $k = 1.960$. With a global confidence-level now selected, specific sensitivity analysis may take place. This specific calculation is presented in section 2.3.

2.4 Thermal equilibrium

In this section, the effects of thermal equilibrium will be briefly discussed.

When changing the operating conditions of the compressor, it will no longer be in thermal equilibrium. It can be said the compressor system is in thermal equilibrium when the rate at which heat is being exchanged between components is constant. Therefore, when changing the operating conditions, and thus also the amount of heat generated, or the amount of heat being moved, the compressor system will no longer be in thermal equilibrium. One may achieve thermal equilibrium by not changing operating conditions, and waiting for it to occur naturally. The time this takes varies, and is dependant on how significantly the operating conditions has been changed.

Thermal equilibrium, or rather the lack thereof, can easily give incorrect data. Figure 2.4 shows two sets of curves. The black lines are all recorded when thermal equilibrium was achieved, while the blue was recorded without waiting for it to occur. The horizontal black curve and the blue curve should overlap after about $Q \approx 0.75\,\mathrm{m}^3/\mathrm{s}$.

Unfortunately, it is not possible to achieve thermal equilibrium for conditions with no- or very little flow. This is because the equipment cannot endure low-flow conditions for prolonged amounts of time,

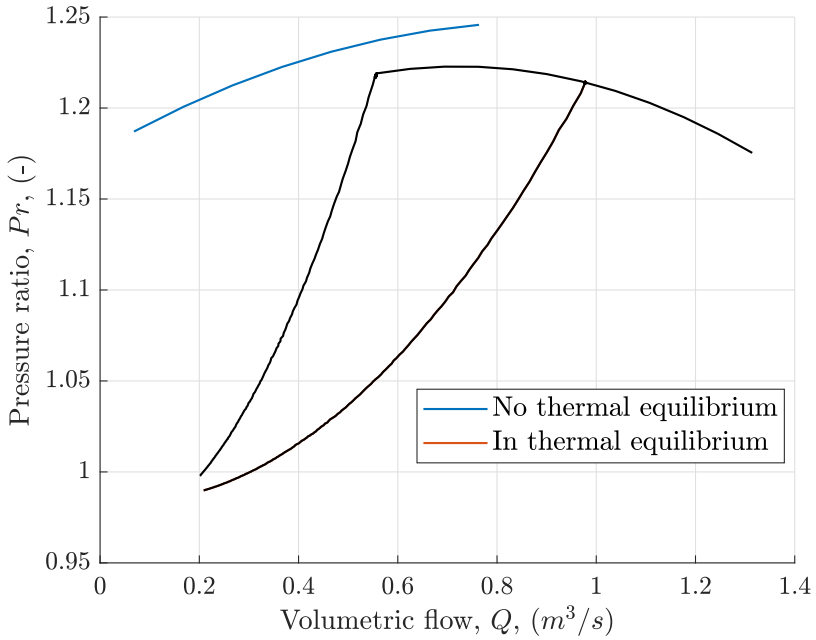

Figure 2.4: Showing the profound effect the lack of thermal equilibrium can have on sensor-readings. The blue curve should be a continuation of the black curve, starting at $Q \approx 0.75\,\mathrm{m}^3/\mathrm{s}$. This could potentially be problematic, if they are severely unmatched, it becomes difficult to defend the efficacy of static tests for describing a dynamic situation, and vice versa.

while it takes prolonged amounts of time before thermal equilibrium may be achieved. Consequently, all results concerning low-flow where temperature measurements are involved should be taken with a degree of scepticism.

3. NTNU Testing Facility

In this chapter the laboratory at NTNU is detailed. This includes layout, quantified measurements, sensors available, and a detailed description of the Matlab script used to analyse the experimental data, and compare it with simulations.

Most of the section detailing the laboratory setup is the same as from the project work [4], as the layout has not been radically changed. The only real difference is that the Venturi-nozzle from previous years has been exchanged for a second orifice with $\beta = 0.5660$.

The section detailing the Matlab script also retains some parts from the project work, as the same scripts has been used for this project. However, these scripts have been radically changed. Though they work by the same principle, a lot more detail has been added, and the scripts have increased in size by a factor of more than 2. Additionally, more scripts have been created. Different from the project work is that these scripts have not been added as an attachment to this thesis – they are now too long for that to serve any practical purpose. Instead, these scripts have been added to the .zip-file (hopefully) attached to this thesis. As with the project work, the scripts are described in this chapter, Section 3.3.

3.1 Test facility setup

This section details the test facility setup during the experiments of this thesis. An illustration of the setup as it was during the experiments detailed in this thesis, is shown in Figure 3.1.

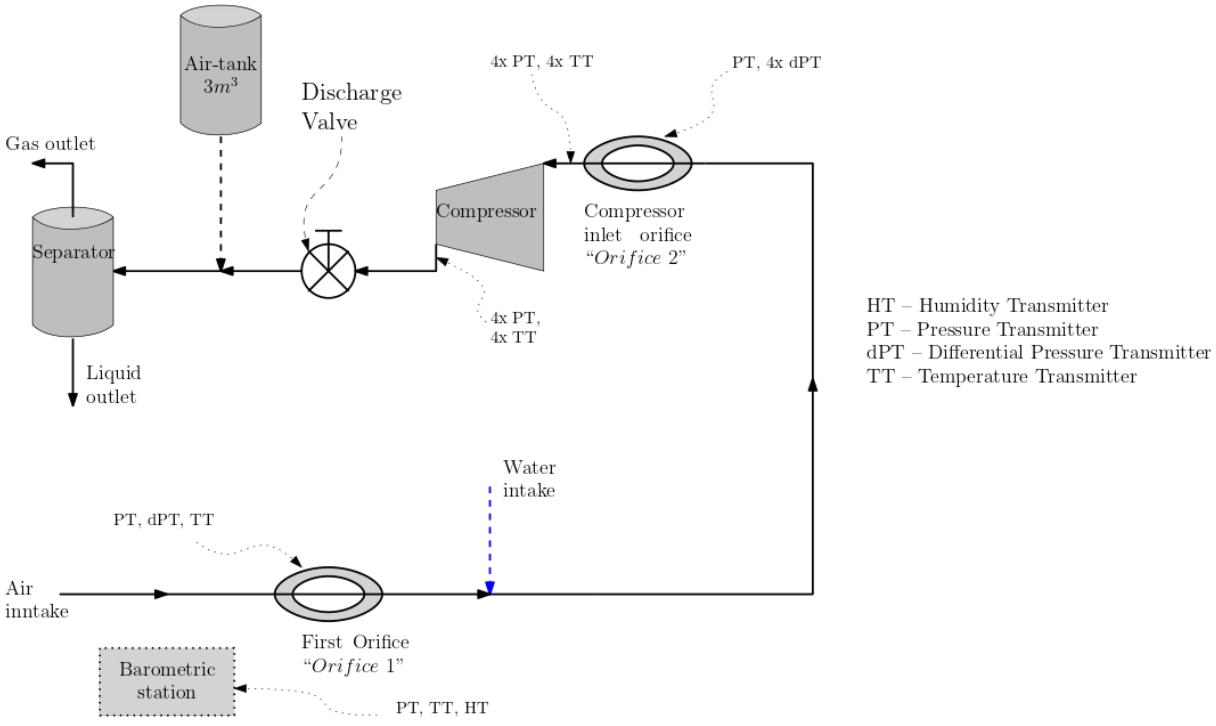

Figure 3.1: NTNU gas compressor test facility layout. The water intake was connected, but never utilised for experiments related to this thesis.

A full-scale single-stage centrifugal compressor is at the heart of the laboratory. Hundseid and Bakken explains the environment in detail in their work [21]. It is operated in mainly atmospheric conditions with a customisable air and water mix as operating fluid. For the experiments related to this thesis, only air was used. The compressor has IGVs, but these were fixed to 0° angle of attack, and the diffuser-section of the compressor is vane-less. The compressor has an acrylic glass inlet pipe, and additional visualisation windows in the diffuser and volute-sections for flow pattern studies.

The barometric station in Figure 3.1 measures the atmospheric conditions of the compressor system. It is located slightly downstream of the inlet, near the first orifice, and is fixed on the piping, but the sensors are all registering the conditions in the environment, rather than the conditions inside the piping.

"Orifice 1*"* from Figure 3.1 is the first of the two orifices, and is located approximately $25\,\mathrm{m}$ upstream of the compressor [12]. The water intake illustrated in the figure was connected but never used. Orifice 1 has a diameter ratio of $\beta = 0.6401$. Table 3.1 shows all sensors used on the first orifice throughout experimental campaign. Orifice 1 is an orifice with corner tappings. Therefore, mass flow to the compressor may be calculated using Equation 2.10 and notably, Equation 2.14.

Sensor "name"	Range (mbar)	Type	Comment
DP25	$[-25, 25]$	Protran PR3202	Connected for all experiments
DP250	$[-250, 250]$		
DP smar	$[-50, 100]$	PCE-28	

Table 3.1: All DP-sensors used on orifice 1 during the course of the experiments. No sensors were added, as it was felt this orifice was covered enough.

The 90° bends seen in the figure reflect the bends in the compressor lab, the figure is not scaled properly, meaning the relative distance between the components in the figure do not reflect reality.

"Orifice 2*"* from the same figure is located approximately 1 to $2\,\mathrm{m}$ in front of the bull nose of the compressor. For the very first experiments, orifice 2 only had two DP-sensors, because the other DP sensors had not arrived yet. For most experiments, however, four DP sensors were used. The properties of the different DP sensors used on orifice 2 is shown in Table 3.2. Orifice 2 has a diameter ratio of $\beta = 0.5660$. Orifice 2 is an orifice with corner tappings. Therefore, mass flow to the compressor may be calculated using Equation 2.10 and notably, Equation 2.14.

Sensor "name"	Range (mbar)	Type	Comment
DP25	$[-25, 25]$	Protran PR3202	Connected for all experiments
DP50	$[-50, 50]$		Used from $30.03.2022$
DP250	$[-250, 250]$		Connected for all experiments
DP smar (2)	$[-50, 250]$	PCE-28	Used from $30.03.2022$

Table 3.2: All DP-sensors used on orifice 2 during the course of the experiments. All sensors were in used from, and including $30.03.2022$.

The "*Discharge Valve*" from Figure 3.1 represents the discharge valve of the system. This valve has an electric actuator on it that can be controlled from the control panel, allowing automatic adjustment. Automatically and remotely adjusting the discharge valve provides great repeatability. Scenarios can be programmed before hand, and played out when the compressor is in operation. Alternatively, the discharge valve can be adjusted directly from the control panel, allowing complete control to the operator.

Specifications of this valve may be found in Table 3.3d.

The "*air-tank*" in Figure 3.1 is a 3000 L tank, which purpose is to increase the downstream fluid volume to better replicate real operating conditions. This air-tank was used for some of the experiments described in this thesis, and is the tank in question when it is referred to the "downstream pressure tank". Sometimes, experiments where this tank was used are referred to as *"S-volume"* tests, or profiles. It should be noted that the facility is able to support an anti-surge recycle loop. However, as the anti-surge loop was disconnected, and not used for this thesis, it is not drawn in the figure.

The entire facility is focused around the compressor, which may be seen on the centre-top of Figure 3.1. Dimensions of this compressor can be found in Table 3.3a, and an overview of the operating conditions in Table 3.3b. Attached to this compressor is an electric motor. Specifications of this motor may be found in Table 3.3c.

Inlet hub diameter	250 mm
Diffuser width	20 mm
Diffuser ratio	1.7
Impeller outlet diameter	400 mm
Outlet pipe diameter	200 mm

(a) Compressor main dimensions.

Working fluid	Air/water
Suction conditions	Atmospheric
Air-flow range	0 kg/s - 3 kg/s
Water-flow range	0 kg/s - 5 kg/s
GVF range	99.93 % - 100 %
GMF range	40 % - 100 %

(b) Main rig features.

Available power	450 kW
Maximum speed	11 000 rpm
Number of poles	3
Shaft coupling	Gearless
Control	Variable speed drive (VSD)

(c) Electric motor.

Manufacturer	FISHER
Rating	ANSI CL150
C_ν, 100 %	3000
Size	10 inches
Valve characteristic	Modified equal %
Valve type	V-ball, 90 degrees

(d) Discharge valve

Table 3.3: Tables detailing some specifications of the test facility and its setup. Exactly the same as Uelands tables 4.1 - 4.4 [10].

As this is a research facility, it is equipped with far more sensors and measuring devices than a corresponding industrial configuration. This is done to better grasp the many phenomena at play, and gain a deeper understanding of operation and control. Moreover, the instruments fitted are better calibrated, with a higher sampling rate and accuracy than what is typical of the industry [13]. Table 3.4 shows an overview of the different sensors used as input parameters for the digital model designed in HYSYS. How the digital model uses these sensor outputs is not relevant for this thesis. For more information about how that link works, it is referred to the project work [4].

Parameter	Accuracy	Range	Freq. [Hz]	Description
		Barometric station		
Pressure	$\pm 0.15\,\mathrm{mbar}$	-	1	Absolute
Temperature	$\pm 0.2\,\mathrm{C}$	-	1	Absolute
Humidity	$\pm 1\,\%$	-	1	Relative, %
		Orifice plate		
Pressure	$\pm 0.018\,\mathrm{bar}$	-	(2,10)	Absolute
Temperature	$\pm 0.122\,\mathrm{C}$	-	(2,10)	Absolute
Pressure	$\pm 0.54\,\mathrm{mbar}$	$[-50, 250]\,\mathrm{mbar}$	(2,10)	Differential
		Water injector		
Pressure	$\pm 3.3\,\mathrm{mbar}$	-	(2,10)	Absolute
		Venturi		
Pressure	$\pm 0.018\,\mathrm{bar}$	-	(2,10)	Gauge
Pressure	$\pm 0.54\,\mathrm{mbar}$	$[-50, 100]\,\mathrm{mbar}$	(2,10)	Differential
		Compressor		
$4\times$ Pressure	$\pm 0.3\,\%$	-	(2,10)	Inlet, absolute
$4\times$ Temperature	$\pm 0.122\,\mathrm{C}$	-	0.05	Inlet, absolute
Torque	± 0.48	-	(2,10)	-
Speed	$\pm 5\,\mathrm{rpm}$	-	(2,10)	-
$4\times$ Pressure	$\pm 0.3\,\%$	-	(2,10)	Outlet, absolute
$4\times$ Temperature	$\pm 0.122\,\mathrm{C}$	-	0.05	Outlet, absolute
		Discharge valve		
Discharge valve position	-	$[0, 100]\,\%$	(2,10)	-

Table 3.4: Relevant instrumentation, used for digital modelling. The exact same as Uelands table 4.5 [10].

3.2 Utilising ISO 5167

This section describes how the ISO 5167 standard was used in relation to this thesis. Including when it was used correctly – to the letter of its requirements – and when it was used, even as some of the conditions for its usage was knowingly unfulfilled. While the idea is explained in this section as well, most details in relation to what exactly was done, are given in Chapter 5. This section focuses mostly on why ISO 5167 was knowingly violated.

Since the primary objective in this thesis is to create a complete, continuous compressor curve from negative flow to compressor choke, it is not possible to always follow ISO 5167. Because the orifices specified in the standard have a bevelled surface, shown in Figure 3.2, they have a distinct "front-side" and a distinct "back-side", meaning orientation of the orifice matters when installing it. For this reason, the standard explicitly states it is only valid for measuring flow coming through the orifice from front-to-back. But, one phenomena that can occur during surge is backwards flow. This can happen quite suddenly and violently, as described in subsection 2.1.2. Because ISO 5167 can not be used verbatim for calculating the reversed flow during surge, some preliminary work must be done before negative flow-readings can be trusted.

In order to prepare for sudden reversed flow during experiments in reduced flow conditions, multiple experiments had to be made beforehand. Specific details will be discussed later in Chapter 5, but the idea will also be covered in this section, to explain how it violates the standard, and why it was still

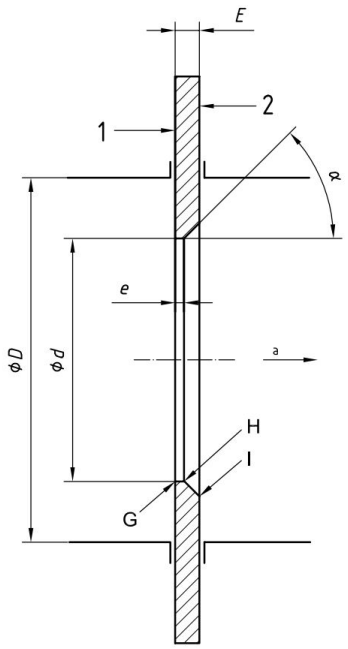

Key
1 upstream face A
2 downstream face B
[a] Direction of flow.

Figure 3.2: Figure from ISO 5167-2 [14]. Showing a schematic of what the standard defines as a ”standard orifice”. Notice the bevelled incline on the downstream-side (The line-segment formed between points *H* and *I*).

considered appropriate.

Since the laboratory has two orifices, one can be used as a reference for the other if they are first validated against each other. Therefore, the first experiments needed to solve the riddle of reversed flow were regular tests where the two orifice plates were compared to each other. The first orifice has already been validated by earlier experiments in the laboratory, and is considered to show the “true” volumetric flow for regular flow conditions [10, 12, 9, 21].

With the orifices validated against each other, a correction factor for reversed flow was developed. This was done by purposefully installing the second orifice reversed for the next couple of experiments. Otherwise, these experiments were conducted in regular fashion (detailed in Section 5.1), using ISO 5167-2 to calculate the flow during the experiments for both orifices. Since the orifice plate is bevelled on the downstream side, as shown in Figure 3.2, reversed flow will theoretically not give the same DP for a given flow as expected. Therefore, ISO 5167 is not valid for reversed flow. But since there is no viable alternative, using ISO 5167 with a correction factor is the best that can be done.

Because it was judged to have an insignificant impact on the result, the temperature sensor used to calculate the density at the second orifice was not moved at all when the orifice was flipped. During the experiments this temperature sensor registered the same trends and temperatures as the earlier tests, leading to an identical density for all practical purposes.

To summarise, the mass flow equations from ISO 5167 was mostly used according to the specifications given in the standard, but for some experiments it was knowingly violated. This was mostly because there was no other alternative. However, the equations were not used verbatim. A correction

factor has been calculated to help adjust the mass flow calculations to a truer representation. Details of this adjustment is given in Subsection 6.1.3.

3.3 Analysing Experimental Results

This section will describe the different Matlab scripts used to read and interpret the experimental data. Raw data from the different sensors need to be processed before they can be analysed. For every experiment, the data logger collected all data in one *.tdms*-file. Matlab was then used to access the different scripts, and produce the results presented in Chapter 5. The first parts mostly consist of descriptions from the project work, albeit updated to fit the newest editions of the script. The scripts described here work mostly on the same principle as during the project work, but most details have been changed, and a lot of work has gone into improving and expanding them, as well as creating the new, third script.

Script name	**Main features**	**Discussed in subsection**
"NTNUExperimentalReader"	Depending on input, selects one *.tdms* file to be read. Translates the parameters in the *.tdms* files into workable variables in Matlab. Plotting raw sensor-outputs.	3.3.1
"TransientResponse_LABEQ"	Calls the *"NTNUExperimentalReader"*-script. Calculates all values for the selected *.tdms*-file. Writes raw-data and calculated data to one excel document.	3.3.2
"ExperimentalDataPlotter"	Uses compiled data from the excel document (mentioned for the above script) to calculate everything not already covered.	3.3.3

Table 3.5: An overview of most important Matlab scripts, and a description of their most important features.

3.3.1 NTNUExperimentalReader – script

The "*NTNUExperimentalReader*"-script reads all the experimental results from the chosen *.tdms*-file and makes the data easily accessible, by giving custom variable-names to different parameters. This script can also plot raw data from all different sensors, to easily inspect the raw data for any anomalies, if requested by the operator. Simply put, the script is choosing a file containing experimental results for a given test, doing a lot of data extraction and naming, and finally some simple plotting.

An automatic function for finding and flagging strange sensor-readings is also a part of the script, though should not be considered perfect, and was not used very extensively for this thesis. The function was written for the project work, but was still used for temperature readings in this work. It was not used more extensively, because the response seen in most of the experiments conducted was too erratic. Tweaking it to work was found to take more energy than it was worth. Since the function is still pretty much the same as it was in the project work, the same explanation given in the project work has been repeated, and added to this Appendix, A3.

3.3.2 TransientResponse_LABEQ – script

The "*TransientResponse_LABEQ*"-script calculates all non-measured, experiment-specific properties discussed in this thesis, outputting vectors, matrices, "structs", and plots. It is in the second script where most of the actual analysis for non-measured properties happen, and also where parts of the secondary objectives are attempted achieved. It is, however, mostly limited to only analysing one experiment at a time, not putting the results in context with the results from other experiments.

It works by calling the first script, "NTNUExperimentalReader", to define most constants and variables, defining the rest of the constants, in the *constants*-part of the script. These constants include pipe geometries, and fluid-specifics such as the specific gas constant, the kinematic viscosity, and some initial guesses of parameters to start a later iteration.

Next, under the *variables*-part, different values directly dependant on experimental values are defined. These include many arrays containing experimental data, as well as average values so that the array-values may be determined at a glance. This part of the code also ensures most arrays are of equal length, wholly dependent on the length of the pressure measurements, because these measurements are always done at a relatively high frequency. Notably, temperature measurements are done at different intervals depending on the data used, but always at a much lower frequency than pressure measurements. Thus, a generalised code had to be made to cover all these quirks. It was noticed that the temperature readings were usually stable, so it was chosen to simply copy the previous temperature measurement for multiple pressure readings, before a new temperature measurement was made again. Thereby simply extending the temperature arrays to be the same length as the pressure arrays. In order to retain some adaptability this code was written within a switch-statement, so the user can easily choose whether to use this approximation, or simply stick with average values for the entire test-period. For dynamic experiments, extending the values in the temperature array was always selected.

Subsequent the variable-part is the *Formulae*-part. This is where most "soft-sensors" are calculated, including all iterative processes. A struct is made for each of the two orifices, and all soft sensors are saved to these structs, with all the different sensors kept separate. Mass flow is calculated for both orifices, using Equation 2.10 from Section 2.2.1. Since Equation 2.10 needs a velocity measurement, iteration using a *while*-loop was used to find a converging flow velocity, and the corresponding mass flow.

Succeeding the formulae-part is a new part where sensor-specific output is generated. It was easiest to automatically create a matrix with selected experimental data, and then manually adding the matrix to a specific excel sheet when the data had been checked for anomalies. This part of the code was very important for further analysis of both static and dynamic experiments, because it included an equation set, where the user could select the relevant DP-sensors that were to be studied more closely. Depending on the experiment examined, some sensors were saturated, especially on the second orifice which saw the highest DP. This equation set allowed saturated sensors to be excluded, so as not to skew the results.

After that part follows the *Table*, and the *Plots* parts. A table containing some selected parameters is constructed and printed to the screen in the table-part, most plots are plotted in the following plots-part.

The *Uncertainty Analysis* and the *Functions* parts are after the table and plots parts. Here the formulas from the uncertainty analysis conducted in Chapter 2.3 is included. Most uncertainty parameters are saved to the struct containing the different sensors-readings for the DP sensors on the second orifice.

Lastly, some custom functions conclude the document. Not all of the functions are used, and not all are working as intended; comments explaining this are added on the relevant functions.

Importantly, for the viability of all these calculations, all experimental values are calculated as arrays throughout the script, keeping all data-points. That means all sensor readings from the experiment are kept and analysed separately (and simultaneously). As the script has some customisation options, the arrays are kept, unless a user has explicitly specified the script to use the average values instead. Using average values should be fine for static experiments. Enabling the option to switch between arrays and average values allows a closer look at the sensitivity of the measurements.

3.3.3 ExperimentalDataPlotter – script

The "*ExperimentalDataPlotter*"-script reads data stored in the same excel document *TransientResponse_LABEQ* writes to, enabling multiple experiments to be examined at once. This script is completely original to this thesis. It is in this third script where the primary objective is attempted, as well as parts of the secondary objectives.

ExperimentalDataPlotter is not programmed to work as dynamically as the other two scripts. This script requires the data, obtained through the use of the two other scripts mentioned, to be saved in a specific manner, so that this script can access it. Also, because the different sections of the script concern parts completely unrelated, the user is required to scroll through the script and toggle the parts on or off through the use of quite a few if-sentences. This must be done only once, but it must be done again if another type of analysis is wanted. As many-a different and highly-specific analysis exist in this script, it is hard to give a satisfying description of all the particulars.

Depending on the part analysed, different sheets from the excel document mentioned earlier is analysed. Most of this script is simply drawing figures, creating regression curves and combining different curves from different experiments. The only calculations happen in the *Correction Factor* part, where some correction factors are calculated for different curves. Because of this relative simplicity, there is no purpose in discussing this scirpt in any more detail.

4. Uncertainty Analysis

The uncertainty analysis that was preformed will be presented in this chapter. Results from this uncertainty analysis is given in Section 6.4. This analysis is based on the theory in Section 2.3, and will include tables describing the relative expanded uncertainty for all parameters analysed. In an attempt to maintain continuity, the layout of this chapter will be very similar to Randen's layout [12]. Since some of the factors he thoroughly analysed in his thesis are still relevant for the current laboratory setup, his analysis of those will not be repeated, only referred to. No experimental results are presented here, so there is little in terms of specifics. For results of the uncertainty analysis, it is referred to Section 6.4.

With the installation of the new orifice plate – known as orifice 2 – an uncertainty analysis must be made to ensure the validity of the new component. As the purpose of the orifice plates is to measure the mass flow rate during the course of the experiments, the uncertainty of the mass flow calculations should be analysed. As Randen [12] made an uncertainty analysis of orifice 1 earlier, an orifice plate with $\beta = 0.6401$, this paper will only focus on the new component. Because both are orifice plates, the process presented in this paper will be nearly identical to what Randen did.

According to the standard ISO 5167-1:2003 [22], the practical working formula for analysing the uncertainty of the mass flow, $\delta\dot{m}$, is given by Equation 4.1:

$$\frac{\delta\dot{m}}{\dot{m}} = \sqrt{\left(\frac{\delta C}{C}\right)^2 + \left(\frac{\delta\epsilon}{\epsilon}\right)^2 + \left(\frac{2\beta^4}{1-\beta^4}\right)^2 \left(\frac{\delta D}{D}\right)^2 + \left(\frac{2}{1-\beta^4}\right)^2 \left(\frac{\delta d}{d}\right)^2 + \frac{1}{4}\left(\frac{\delta\Delta p}{\Delta p}\right)^2 + \frac{1}{4}\left(\frac{\delta\rho_1}{\rho_1}\right)^2} \tag{4.1}$$

The uncertainty to the discharge coefficient (C), and the expansibility factor (ϵ) is found in ISO 5167-2 [14]; the parameters: β, D, and d are constants, dependant only on the laboratory setup; with the last parameters Δp, and ρ_1 being dependant on operating conditions, and the measuring sensors in the laboratory. Some of these parameters are dependant on others, and therefore they will be presented in the order stipulated below.

Parameter	**Presented in section**
Differential pressure (Δp)	4.1
Density (ρ_1)	4.2
Diameter ratio (β), including pipe diameter (D), and orifice diameter (d)	4.3
Expansibility factor (ϵ)	4.4
Discharge coefficient (C)	4.5

Table 4.1: Table of contents for the uncertainty analysis.

4.1 Differential pressure (Δp)

At some point during the experiments, there were as many as four different differential pressure sensors on the second orifice, as mentioned in Table 3.2, in Section 3.1. Three of them were of the type Protran PR3202 from ESI Technology Limited, with ranges $\pm 25\,\mathrm{mbar}$, $\pm 50\,\mathrm{mbar}$, $\pm 250\,\mathrm{mbar}$; referred to as DP25, DP50, and DP250 respectively. Giving a total span of $50\,\mathrm{mbar}$, $100\,\mathrm{mbar}$, and $500\,\mathrm{mbar}$. Specifications provided by the manufacturer may be found in Appendix A1.1. The last sensor was of the PCE-28 type, with the range $\Delta p \in [-50, 250]\mathrm{mbar}$, a total span of $300\,\mathrm{mbar}$. This sensor is the same as the one Randen specified, although the span is larger (by $50\,\mathrm{mbar}$). Specifications for the PCE-28 may be found in the Appendix A1.2.

Because Randen has already done an uncertainty analysis for the PCE-28 sensor and the other sensors used, this section will focus solely on presenting an uncertainty analysis of the Protran sensors.

Non-linearity, hysteresis and repeatability (NLHR) error statement:
ESI Technology Limited [23], the manufacturer of the Protran sensor, has specified the NHLR uncertainty to be less than or equal to $0.3\,\%$ of the Full Span (FS) with relation to the Best Fitted, Straight Line (BFSL). Different pressure sensors will have a uniquely curved output signal due to their manufacture. Using the BFSL is a way to present the quality assured accuracy of the manufacturer [24]. Equation 2.21 gives

$$u(\Delta p_{accuracy}) = \frac{U_{accuracy}}{k} = \frac{FS \cdot U/FS}{k}$$

A practical example will be given to provide some clarity around these calculations. It is restated that FS is the Full Span of a DP-sensor. A sensor ranging from $-250\,\mathrm{mbar}$ to $250\,\mathrm{mbar}$ will thus have an FS of $500\,\mathrm{mbar}$. With the uncertainty of $0.3\,\%$ of the Full Span (uncertainty/FS), this would result in a $u(\Delta p_{accuracy}) = 0.7653\,\mathrm{mbar}$, when the coverage factor $k = 1.960$, as it is for a $95\,\%$ confidence interval. Table 4.2 show the resulting standard uncertainty because of the DP transmitter

Sensor	**Standard Uncertainty** (mbar)
DP25	0.0765
DP50	0.1531
DP250	0.7653

Table 4.2: The standard uncertainty of NHLR errors for the Protran PR3202 sensors.

Temperature effects:
According to the manufacturer, temperature will affect the readings by no more than $\pm 2.0\,\%$ of the full span pressure reading, assuming the temperature is between $-20\,^{\circ}\mathrm{C}$ and $+70\,^{\circ}\mathrm{C}$. The temperature will at all times during the experiments for the differential pressure sensors be within $T \in [20, 50]^{\circ}\mathrm{C}$, therefore, the manufacturers values may be used. Thus, $U_{Temperature} = FS \cdot (U_{Temperature}/FS)$. The calculation is the same as for the NHLR uncertainty above. The standard uncertainties due to temperature effects is presented in Table 4.3.

Zero Offset and Span Tolerance:

Sensor	Standard Uncertainty (mbar)
DP25	0.5102
DP50	1.0204
DP250	5.1020

Table 4.3: The standard uncertainty because of temperature effects for the Protran PR3202 sensors.

Zero offset is the actual signal output at zero DP. Before experiments can commence, the sensor needs to be zeroed to the operating conditions in the test facility. This can be achieved by adjusting the trimming potentiometers located beneath the enclosure lid of the sensor. At room temperature, it is possible to adjust this zeroing by about as much as $\pm 5\%$ of the full-scale range. This was done manually on all DP-sensors with a standstill test before any experiments commenced.

Total standard uncertainty

It can be assumed that the uncertainty due to temperature effects, and NHLR effects are independent of each other. Equation 2.19 and Equation 2.20 was used to find the combined standard uncertainty, and Equation 2.21 was then used to find the relative expanded uncertainty for the Protran sensors. This expanded uncertainty is presented in Table 4.4, and can be used directly for any DP measurements recorded with the corresponding sensor. For example: A DP reading for DP50 is now with $95\,\%$ certainty within the range; $\Delta p \in [x - 2.0224, x + 2.0224]\ \mathrm{mbar}$, where x is the raw reading given in mbar.

Sensor	Expanded Uncertainty (mbar)
DP25	1.0112
DP50	2.0224
DP250	10.1119

Table 4.4: The expanded uncertainty for the Protran PR3202 DP sensors.

4.2 Density (ρ)

Density is calculated at the orifice plate inlet according to Equation 4.2.

$$\rho_1 = \frac{p_1}{Z_1 R T_1} \tag{4.2}$$

where ρ_1 is the density at orifice inlet (before the orifice); p_1 is the pressure at orifice inlet; R is the fluid-specific gas constant; T_1 is the temperature at inlet; and Z_1 is the compressibility of the fluid at orifice inlet. Because the experiments are concerning air at near-atmospheric pressure levels, and near-room temperature levels, $Z = 1$. The ideal gas law is a valid equation to use for these purposes to calculate the density of the fluid. It simplifies the process immensely, and there is little to be gained from using a more accurate method, as the sensors are incapable of measuring the accuracy needed for there to be any point using these methods.

The pressure is measured with a PCE-28 absolute pressure sensor. Manufacturer specifications of the pressure sensor may be found in Appendix A1.2. The exact same sensor was used by Randen to measure

the absolute pressure on the first orifice. In this paper two such sensors exist: one for each orifice, each with the range $[0,\ 1.6\,\mathrm{bara}]$. Since these sensors have been calculated by Randen, the individual steps are not repeated, but the expanded uncertainty is recalculated, and the answer is displayed in Table 4.5.

The temperature is measured with a CTR5000 precision thermometer coupled with a CTP5000 reference thermometer. Thermometer specifications may be found in Appendix A1.3. As with the pressure sensor, the temperature sensor is the exact same as the one Randen used.

Parameter	**Sensitivity coefficient**	**Expanded uncertainty (U)**
Absolute pressure, p	Equation 4.3	$0.0277\mathrm{mbar}$
Absolute temperature, T	Equation 4.4	$0.0412\,\mathrm{K}$
Density, ρ	-	Equation 4.5, dependant on temperature and absolute pressure

Table 4.5: Expanded uncertainty for different parameters used to calculate ρ, and the expanded uncertainty for ρ itself. Based on calculations by Randen, but redone with relevant data (added 1 more year since calibration where relevant, changed temperature range for the pressure sensor to account for reversed flow etc.).

Equation 4.3 and Equation 4.4 are the sensitivity coefficients for the pressure and temperature terms respectively. The expanded uncertainty for density is calculated by using the method described in Section 2.3.

$$\frac{\partial \rho}{\partial p} = \frac{1}{R\,T} \tag{4.3}$$

$$\frac{\partial \rho}{\partial T} = -\frac{p}{R\,T^2} \tag{4.4}$$

$$U_\rho = \kappa \sqrt{\left(\frac{U_p}{\kappa}\ \frac{1}{R\,T}\right)^2 + \left(\frac{U_T}{\kappa}\ \left(-\frac{p}{R\,T^2}\right)\right)^2} \tag{4.5}$$

where U_ρ is the expanded uncertainty of density calculations given in $\mathrm{kg/m^3}$; U_p is the expanded uncertainty of pressure measurements given in Pa; U_T is the expanded uncertainty of temperature measurements given in K; κ is the coverage factor; R is the ideal gas constant; T, and p are temperature and pressure measurements respectively. Finally, ρ will be in the interval given by Equation 4.6 with $95\,\%$ confidence, with the coverage factor $\kappa = 1.960$.

$$\rho_1 = \frac{p_1}{R\,T_1} \pm \kappa \sqrt{\left(\frac{U_{p_1}}{\kappa}\ \frac{1}{R\,T}\right)^2 + \left(\frac{U_{T_1}}{\kappa}\ \left(-\frac{p}{R\,T^2}\right)\right)^2} \tag{4.6}$$

4.3 Diameter ratio

As some slight adjustments has been made to fit it to the existing piping, this new orifice plate has a practical beta factor equal to $\beta = 0.5660$, with the inner diameter being $d = 130.176\,\mathrm{mm}$, and the outer diameter $D = 0.230\,\mathrm{m}$. The outer diameter was measured by hand, while the inner diameter was given by the manufacturer. Since the outer diameter was measured by hand, it is reasonable to assume an error of about $\pm 1\,\mathrm{mm}$. The inner diameter is given by the manufacturer to have an uncertainty of no more

than about $0.1\,\%$, resulting in an expanded uncertainty of $0.1302\,\mathrm{mm}$. The sensitivity coefficients for the diameter ratio is given in the Appendix A2, Equation A.1. Thus, the total expanded uncertainty for the diameter ratio is $U_\beta = 2.5251 \cdot 10^{-3}$, and therefore $\beta = 0.5660 \pm 0.0025$ with $95\,\%$ confidence.

4.4 Expansibility factor

According to ISO 5167-2:2003 [14], the expansibility factor is calculated by Equation 2.13. This equation has been reiterated below for convenience:

$$\epsilon = 1 - (0.351 + 0.256\beta^4 + 0.93\beta^8) \left[1 - \left(\frac{p_1 - \Delta p}{p_1}\right)^{\left(\frac{1}{\gamma}\right)}\right]$$

ISO 5167-2 also says that when β, p_1, Δp, and k are assumed to be known without error, the relative expanded uncertainty of this expansibility factor is expressed as Equation 4.7.

$$\left(\frac{U\epsilon}{\epsilon}\right) = 3.5\,\frac{\Delta p}{\gamma\, p_1}\,\% \tag{4.7}$$

γ is assumed to be $\gamma = 1.401$ for all experiments, due to the small temperature and pressure changes in the system, and because the operation conditions are near atmospheric. But since β, p_1, and Δp have an associated uncertainty, their uncertainty must be added to the calculations of the expansibility factor. Their sensitivity coefficients are shown in Equation A.2 in Appendix A2, and are used in Equation 4.8, where the expanded uncertainty for the expansibility factor is calculated.

$$U_\epsilon = \kappa \sqrt{\left(\frac{U_\beta}{\kappa}\,\frac{\partial\epsilon}{\partial\beta}\right)^2 + \left(\frac{U_{p_1}}{\kappa}\,\frac{\partial\epsilon}{\partial p_1}\right)^2 + \left(\frac{U_{\Delta p}}{\kappa}\,\frac{\partial\epsilon}{\partial\Delta p}\right)^2 + \left(3.5\,\frac{\Delta p}{\gamma p_1}\,\epsilon\,\frac{1}{\kappa}\,\frac{1}{100}\right)^2} \tag{4.8}$$

4.5 Discharge coefficient

Similarly to the expansibility factor, ISO 5167-2 provides a method for calculating the uncertainty of the discharge coefficient. That method is simply $U_C/C = 0.5\,\%$ for the given β-value, but it presupposes that β, D, and Re_D is known without error. Therefore, same as above, because β, D, and Re_D are not known without error, their uncertainties are added to the expanded uncertainty, and result in Equation 4.9. The sensitivity coefficients are defined in Appendix A2, Equation A.3.

$$U_C = \kappa \sqrt{\left(\frac{U_\beta}{\kappa}\,\frac{\partial C}{\partial\beta}\right)^2 + \left(\frac{U_D}{\kappa}\,\frac{\partial C}{\partial D}\right)^2 + \left(\frac{U_{Re_D}}{\kappa}\,\frac{\partial C}{\partial Re_D}\right)^2 + \left(0.5\,C\,\frac{1}{\kappa}\,\frac{1}{100}\right)^2} \tag{4.9}$$

If $Re_D < 10^4$, a small factor of $+0.5\,\%$ must be added to the last element in Equation 4.9, according to the standard.

4.6 Flow uncertainties

After all uncertainties of elements in Equation 4.1 has been calculated, the uncertainty for mass flow may also be calculated.

With $\partial\dot{m}$ – or U_m – calculated, U_Q can be found. U_m and $\partial\dot{m}$ are the same thing. The standard uses ∂m, but in keeping with the theme through this chapter, U_m is more appropriate. Since Q is calculated by Equation 2.15, the sensitivity coefficients for Q become those expressed in Equation 4.10.

$$\frac{\partial Q}{\partial m} = \frac{1}{\rho} \tag{4.10a}$$

$$\frac{\partial Q}{\partial \rho} = -\frac{m}{\rho^2} \tag{4.10b}$$

Thus making U_Q as expressed by Equation 4.11.

$$U_Q = \kappa \sqrt{\left(\frac{U_m}{\kappa}\,\frac{\partial Q}{\partial m}\right)^2 + \left(\frac{U_\rho}{\kappa}\,\frac{\partial Q}{\partial \rho}\right)^2} \tag{4.11}$$

5. Experimental Campaign

This chapter includes details about the experimental campaign conducted at the NTNU compressor test facility, explains what is meant by the *"profile test"* in this thesis, and briefly gives definitions of the different flow regions.

5.1 List of experiments

Table 5.1 shows the different experiments made, along with what the focus of the experiment was. Also displayed in the table is a reference to the section in this chapter where data from the experiment was used as a foundation for the discussion. Some smaller tests were done earlier than 17.03, but because these mainly concerned tweaking and calibrating different sensors, they were excluded from the table.

Date of experiment	Focus of experiment	Described in section	Comment
17.03	Obtaining a regular, thermodynamically stable 9000-RPM curve	6.1.1	Static experiment
25.03	Obtaining a compressor curve for reduced flow. Not thermodynamically stable.	6.1.2	Static experiment
30.03	Experimenting with a dynamic compressor curve. Exploring early sensor readings and responses.	6.2, 6.2.1	Dynamic experiment. "Standard Profile test" determined based on this experiment. Importance of logging frequency also discovered in this test.
04.04	Examining the effects of short sensor tubes.	6.2.2	Dynamic experiment
05.04	Obtaining multiple reduced flow profiles. Two regular reduced profiles, and one with the downstream pressure tank connected.	6.2.3, 6.2.4, 6.2.5	Dynamic experiment
07.04	Reversed flow. Static curve in reversed flow, and dynamic curve in reversed flow. Not thermodynamically stable.	6.1.3, 6.2.6	Static and dynamic experiment. 5 data points for static curve taken, 4 profiles for dynamic curve.
04.05	Obtaining static samples for a complete compressor curve (except negative flow), with the downstream pressure tank connected.	6.1.2	Static experiment

Table 5.1: Displaying all significant experiments done, and when they were done, along with which sections the experiments are described in.

It should be noted that for the first two experiments mentioned in Table 5.1 (17.03 and 25.03) were preformed with a reduced amount of sensors, meaning "Option A" in Table 5.2, while all other experi-

ments mentioned in Table 5.1 was preformed with all sensors, or "Option B" in Table 5.2. "Option A" was used early on, because not all sensors for "Option B" had arrived, or been installed yet, as mentioned in Table 3.2.

DP sensor options	**Available sensors**	
	in Orifice 1	in Orifice 2
Option A	DP250, DP25, DP smar	DP250, DP25
Option B	DP250, DP25, DP smar	DP250, DP50, DP25, DP smar 2

Table 5.2: The different combination of DP sensors available on the two orifices. The same information is given by Tables 3.1, and 3.2. The PCE-28 sensors, referred to as DP smar and DP smar 2, registers DP in the range: $[-50, 100]$ mbar and $[-50, 250]$ mbar respectively. The Protran sensors registers DP in the range $\pm(name)$, so DP25 registers DP in the range $[-25, 25]$ mbar.

The first weeks of the semester were spent making preparations for the coming experiments. In the laboratory, this meant reestablishing the layout which existed during Ueland's and Randen's experiments [10, 12], with one notable exception. The Venturi-nozzle that existed during their tests was exchanged for a second Orifice with a diameter ratio of $\beta = 0.5660$, in the hopes of better capturing the flow near the compressor.

After the piping had been refitted, the sensors were selected, connected and configured. A lot more sensors were available for this experimental campaign than what was available for previous experiments. At the orifices, DP-sensors were run in parallel, ensuring that ample pressure readings over the orifices – and in extension – ample flow calculations in the system were obtained. The flow calculations were of particular interest, due to the objectives outlined at the start of this thesis.

But before the orifice plates can be used to calculate flow, the sensors attached to it must be configured. DP-sensors were mainly calibrated via a standstill test and trimming the potentiometers mentioned in Appendix A1.1. During a standstill test, a test where nothing but sensors are running, there is no flow in the tubes, and therefore the DP signal should be zero. All DP sensors were trimmed to be as close to zero as possible. Readings from temperature sensors and absolute pressure sensors were all recorded during the standstill tests to look for any outlier signal. At the end of this process, some low-scale tests were done, to check that all sensors were responding appropriately. These low-scale tests are not recorded in Table 5.1.

Preparations were also made outside of the laboratory. The Matlab scripts from Arstad's project thesis [4] was revisited, updated and improved upon considerably. A lot of effort went into improving the autonomy and readability of the Matlab scripts, and removing superfluous code and outdated functions. It was also brought up to date to work with the new-, and previous-but-renamed sensors.

Additionally, an uncertainty analysis was made, calculating the uncertainty of all the new components added since Randen's time. How this analysis was principally done has been described in Section 2.3. The results of the analysis has been included in 6.4.

5.2 The Profile test

It was necessary to standardise the tests to limit the sources of error as much as possible. Creating a standardised dynamic test made everything easier; comparing results are easier when only one thing changes from one experiment to the next (the thing being directly analysed; doing the experiments was easier as it was the same procedure every time; and finally, practical repeatability of the tests increases, because there is no doubt about how the tests were done, and they can easily be redone.

An example of this *"profile test"* that was often done in order to study reduced flow regions and surge is shown in Figure 5.1. Figure 5.2 shows some basic definitions relating to this test. The terms are originally derived from the operating program of the discharge valve.

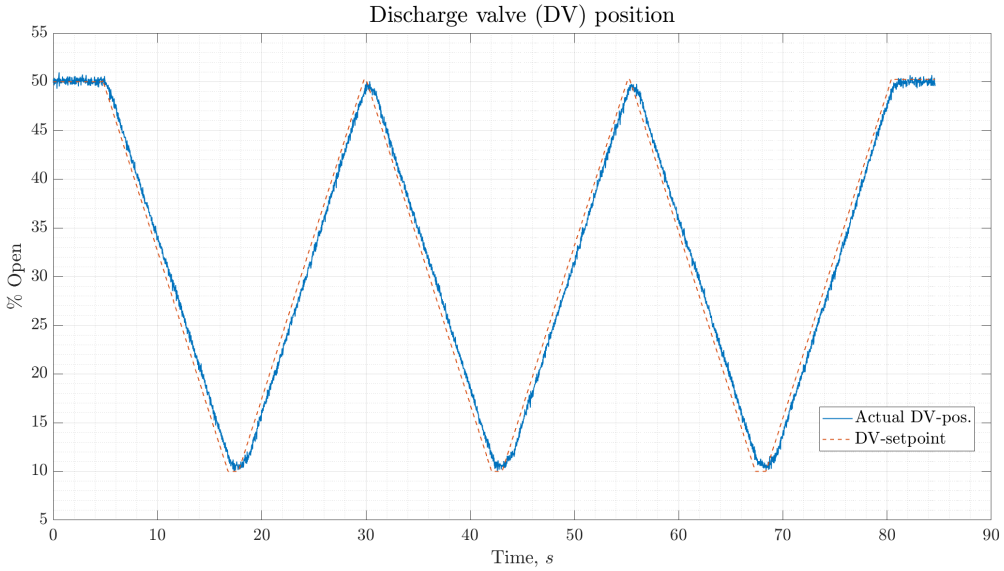

Figure 5.1: Showing how the discharge valve was opened and closed during a typical dynamic test, referred to as the *"profile test"*.

What	Value
Ramp time	30 s
Hold time	5 s
Wait time	1 s
Start	50 %
End	10 %
Repeated	3 times

Table 5.3: Showing the specifications of a standard profile test. All dynamic experiments conducted with a so-called "profile test" was done with these specifications. The "*Repeated*"-row refers to how many dips were created for each time the profile test was run.

The profile test was used extensively when studying reduced flow and surge, because it covered all of the area that was interesting – from *normal* operation in stable regions, to almost zero flow and definite surge – without staying too long in regions potentially harmful for the compressor system. Repeating the trip three times in a row, as the profile test did allowed more data to be gathered from the same test, and made it possible to discover any irregularities that might have occurred in any of the dips.

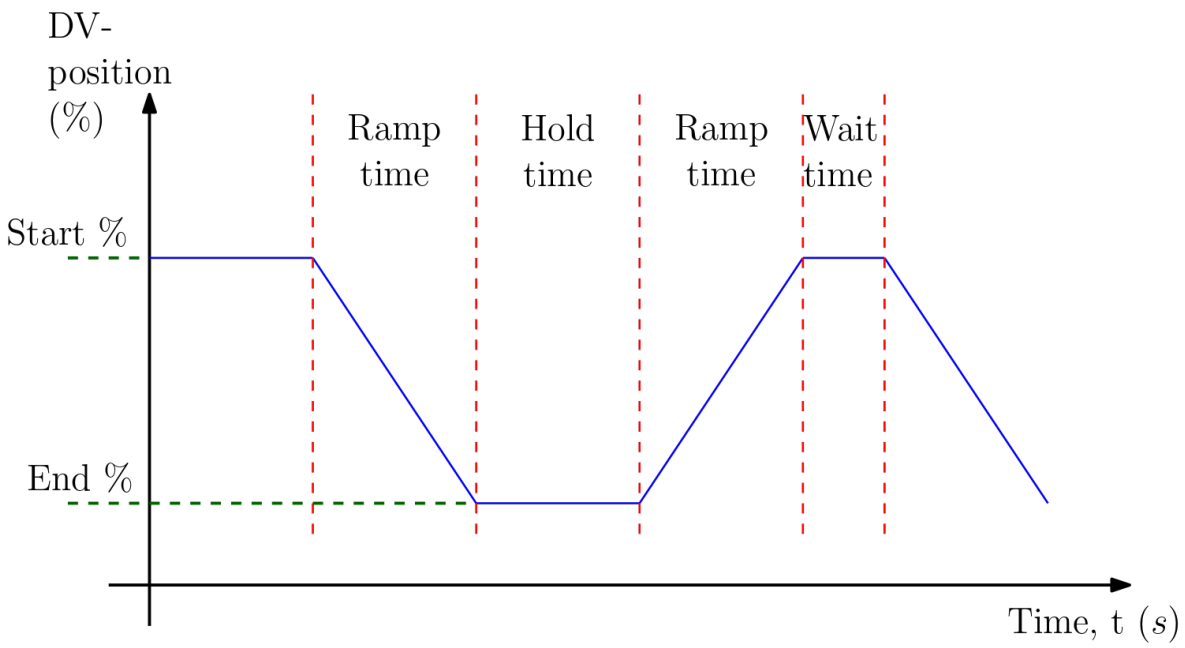

Figure 5.2: Some basic definitions and terminology for specifying profiles, with relation to the position of the discharge valve. Relevant to understand Table 5.3, which provide the experiment specifics.

5.3 Flow regions

[h] To reduce the amount of wording needed to describe the different experiments and parts of a curve, three flow regions are defined. The definition is an arbitrary definition only valid for this thesis. Table 5.4 shows these definitions.

Name	Meaning
Normal flow, or Regular flow	$Q \in (0.5, 1.32]\ \mathrm{m}^3/\mathrm{s}$
Reduced flow	$Q \in [0, 0.5]\ \mathrm{m}^3/\mathrm{s}$
Reversed flow	$Q \in (-\infty, 0)\ \mathrm{m}^3/\mathrm{s}$

Table 5.4: Defining the different flow regions in this thesis. Reversed flow covers the region with any negative (or reversed) flow, Normal flow covers the normal operation range of the compressor, while Reduced flow covers the unstable region between normal flow and reversed flow.

6. Results and Discussion

The results and the discussion will be presented in this chapter. Results and discussions relating directly to an experiment will be put in one of two categories; either as a static experiment, or as a dynamic experiment. The following section will detail efforts to combine different experimental values into one. This is where the continuous compressor curve will be presented. Concluding this chapter will be the most important results of the uncertainty analysis, briefly showing the uncertainty of the different Protran sensors on the second orifice.

6.1 Static Experiments

Static experiments are experiments conducted with conditions as close to static as possible. That means the compressor speed, and the discharge valve position are kept at as static values as possible.

Since dynamic experiments are somewhat different between each "profile", static experiments can be seen as the more repeatable of the two. The small differences between the dynamic profiles can be seen in Figure 6.15 from Subsection 6.2.5, for example. However, static experiments become harder to carry out when flow decreases, without damaging the equipment. And, as uncertainties increase with decreasing flow, as Section 6.4 shows, static tests also become laced with uncertainties.

6.1.1 Regular compressor curve

The aim of the experiments described in this subsection was to verify that the compressor still operates along the curves found by Ueland [10]. To achieve this, a series of static samples were taken along the entire operational range of one of the curves plotted using data from Ueland; from fully open to the onset of instability. The resulting samples were used to plot a curve meant to represent the compressor path.

Samples were gathered at thermal equilibrium in order to get as precise a curve as possible, and because Ueland's curves were found at thermal equilibrium. For the purpose of this experiment, it was decided that thermal equilibrium was achieved when none of the temperature sensors in the entire system experienced more than a $1\,^{\circ}\mathrm{C}$ change in temperature for a period of 10 minutes. When that condition had been met, the sensor output was recorded for a 5 minute period. The results of these recordings are listed in Table 6.1.

Using the samples shown in Table 6.1, the compressor curve for $9000\,\mathrm{RPM}$ was plotted, and Matlab was used to find the second degree regression curve connecting the dots. The resulting plot may be found in Figure 6.1a. Figure 6.1b shows this curve plotted together with the compressor-curves defined by data from Ueland's experiments. There is substantial overlap between these from $Q = 0.6\,\mathrm{m}^3/\mathrm{s}$ to about $Q = 1.3\,\mathrm{m}^3/\mathrm{s}$. They do not overlap all the way, however, which is hardly surprising considering that a compressor curve is defined by its system's characteristics, and the setup is not the exact same as it was during Ueland's experiments. The Venturi-nozzle that existed in Ueland's system has been exchanged for a second orifice. This second orifice is smaller than the first orifice, meaning it is the limiting factor

Test number	Compr. speed (RPM)	DV- position (% of open)	Q (m^3/s)	Pr
1	9019.3	99.8	1.314	1.176
2	9019.3	90.9	1.294	1.179
3	9019.3	76.9	1.216	1.190
4	9019.5	67.9	1.142	1.198
5	9019.6	60.8	1.049	1.208
6	9019.7	56.8	0.957	1.215
7	9019.9	52.9	0.839	1.220
8	9020.1	50.0	0.739	1.225
9	9019.3	45.7	0.627	1.223
10	9019.2	43.5	0.550	1.218

Table 6.1: Showing samples found when the system was running at thermal equilibrium. Each sample is an average reading of a 5 minute recording. Q is the volumetric flow, while $Pr = p_2/p_1$ is the pressure ratio over the compressor. Logging frequency was 2 Hz. It is emphasised that the accuracy of these measurements are not ± 0.001. The numbers are given with these many decimals so calculations and experiments done later can be compared to these values more easily.

in the current system, with regards to volume flow. Evidently seen in Figure 6.1b, this second orifice restricts the flow more than the Venturi-nozzle did, and now $Q_{max} \approx 1.32\,\mathrm{m}^3/\mathrm{s}$.

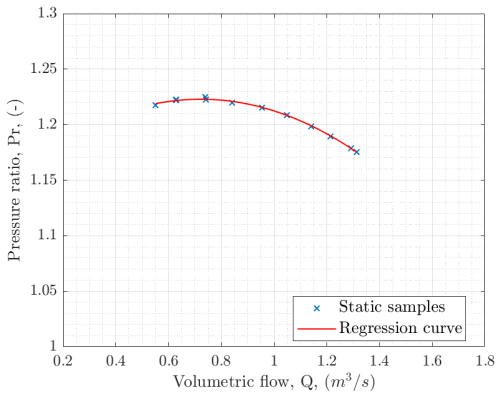

(a) Compressor curve for 9000 RPM. Data from experimental results obtained March 17th, 2022. Regression line calculated by Matlab.

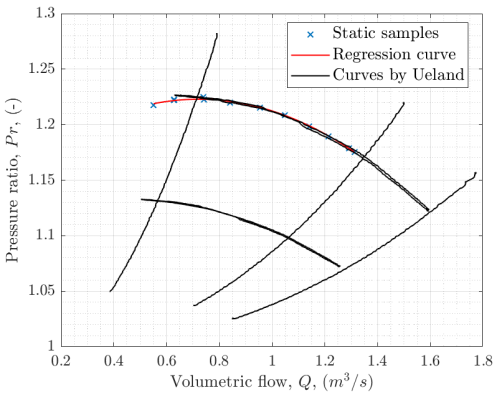

(b) Figure 6.1a with compressor curves made by using experimental data obtained by Ueland in 2021 [10].

Figure 6.1: Showing the compressor curve obtained by recent experiments in a, and how they compare to previous curves in b. Note that the black curves were created based on the old compressor-rig, with a Venturi nozzle instead of a second orifice.

Importantly, however, the new orifice only limits the flow, it seemingly does not change the system behaviour. Since the pressure ratio for a given volumetric flow is the same, it is concluded that the system still respond somewhat similarly to what Ueland mapped. Using the affinity laws mentioned in Subsection 2.1.1, one may then extrapolate the other curves from the curve defined in this thesis. An important distinction between the current system and the one Ueland described, is that the choke line has shifted quite dramatically, and subsequently limited the compressor to a smaller operational area. The curves by Ueland may thus only be used as a guideline, and should not be taken to be describing the current system exactly, especially in high-flow areas.

6.1.2 Reduced flow

With the first compressor line plotted as a baseline, work continued by trying to map the compressor profile in the reduced flow region. Table 6.2 shows all samples collected March 25th, that are defined as static tests in reduced flow. As the table shows, the discharge valve was never completely closed, and that there was a small flow calculated at all times.

Test number	Compr. speed (RPM)	DV- position (% open)	Q (m^3/s)	Time (s)
1	9021.4	50.2	0.765	65.5
2	9021.5	46.8	0.640	62.0
3	9021.4	41.3	0.509	61.5
4	9021.4	38.3	0.424	33.5
5	9021.3	34.3	0.299	19.0
6	9021.3	31.3	0.220	27.5
7	9021.2	15.4	0.050	22.0
8	9021.3	9.2	0.073	27.0

Table 6.2: Showing all static experiments carried out in the reduced flow region for the 25th of March. Logging frequency was set to 2 Hz. It is emphasised that the accuracy of these measurements are not ± 0.001. The time-column shows how long time was used on each test. The numbers are given with these many decimals so calculations and experiments done later can be compared to these values more easily.

An important difference worth noting is that the static samples recorded were not recorded when the system was in thermal equilibrium. Because of the volatile nature of surge, it is potentially harmful for the compressor to operate in these lower-flow conditions for prolonged periods of time. Even smaller periods might be harmful, if the flow is severely reduced. Therefore, the compressor was never kept running with these reduced flows for very long. Generally, the more reduced the flow was, the less time was allocated to recording data in that area, though some exceptions occurred, as can be seen in the time-column of Table 6.2.

The resulting curve of the data obtained in Table 6.2 is shown in Figure 6.2. For a small region, the data points obtained for lower flow regions overlap with the data points obtained in thermal equilibrium during earlier tests. As can be seen in the figure, the pressure ratios for a given volumetric flow are markedly different from each other, illustrating the significance thermal equilibrium – or the lack thereof – is having on the tests.

Figure 6.2 also shows a predicted line, which is an extension of the regression line in the figure. This extended regression line covers whats left of the thermodynamic equilibrium-line, and shows just how much the characteristics of the system can change depending on whether or not thermal equilibrium has been achieved.

Figure 6.3a shows the entire compressor profile for the system when it has not reached thermal equilibrium, and when the downstream pressure tank is connected. It was made some time after Figure 6.2 had been made. Table A4.1.1 in Appendix A4.1 shows the data points used to plot Figure 6.3a. New to this plot – other than the conditions which resulted in this plot – the individual signature of the orifices is shown. Blue shows orifice 1's signature, while red shows orifice 2's signature, with black being the average signature.

As Figure 6.3a shows, the measured response is not the exact same for both orifices. The compressor curve calculated using the second orifice covers a larger range than the first orifice. In areas with reduced

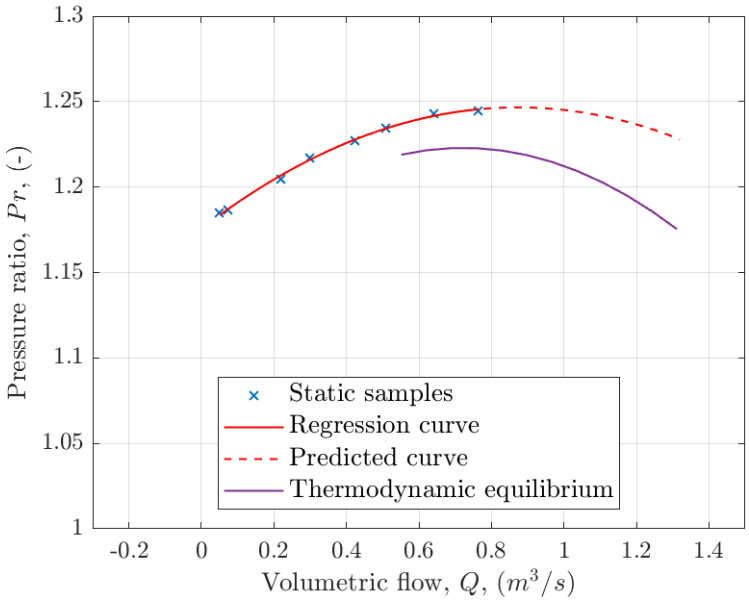

Figure 6.2: Static samples are from Table 6.2, red curve is a regression curve of these samples. The *predicted curve* is an extension of this regression curve. The *thermodynamic equilibrium* curve is a regression curve derived from Table 6.1.

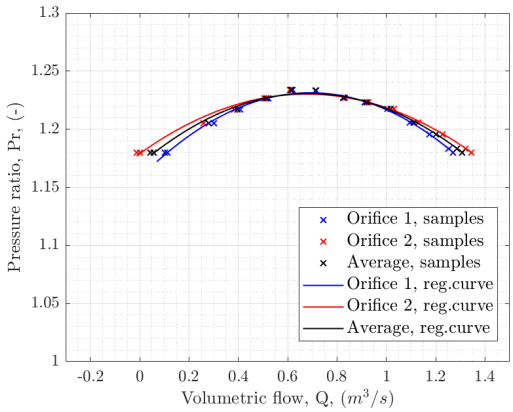

(a) Showing the resulting points and curves derived from Table A4.1.1 in the Appendix A4.1. This experiment was done with the downstream pressure tank connected.

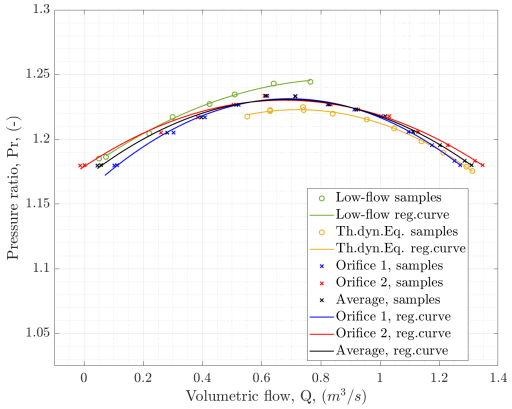

(b) Figure 6.3a is plotted again with the curves from Figure 6.2 for perspective. The green points and curve are the low-flow (or reduced flow data), while the yellow points and curve show the compressor curves when the system is in thermodynamic equilibrium. The red, blue, and black curves are the same as in Figure 6.3a.

Figure 6.3: These figures show the full positive profile of the compressor curve when the compressor is running at 9000 RPM with the downstream pressure tank connected, and how these curves relate to the earlier static compressor curves. Specifically, how they relate to the reduced flow curve, and the thermodynamic equilibrium curve from Figure 6.2.

flow, this is due to orifice 1 hardly registering reversed flow, which was not unexpected, considering how far away the first orifice is from the compressor, and even with the downstream pressure tank connected, the downstream flow volume is relatively small. On the other end of the scale, calculations based on orifice 2 result in slightly larger volume flow, with no obvious explanation. It is worth noting that the disparity is greatest in the reduced flow-region. But, for the most regular flows, both orifices coincide

quite well.

Figure 6.3b shows how this profile fits with the earlier creations. It fits very well, especially on the extremities, and seems to be a good average of the two curves from Figure 6.3. It is interesting to see that the downstream pressure tank produces such a pronounced effect, especially where $Q \approx 0.5\,\mathrm{m}^3/\mathrm{s}$; an area where one would not necessarily expect it to have such a clear impact.

6.1.3 Reversed flow

In this subsection, reversed flow will be closer studied. Specifically, ISO5167-2 will be tested for reversed flow, despite it not being valid in reversed flow, according to itself [14]. This idea has already been discussed in Section 3.2, but will be reiterated in this section, to recontextualize it to how it was done.

Because of the bevelled surface on the orifice, shown in Figure 3.2, the orifices have a distinct "front-side" and "back-side". Equation 2.10 from ISO 5167-2 [14] is really only valid when used to calculate mass flow flowing through the front to the back of the orifice. Since reversed flow is to be expected when operating in the reduced flow conditions already outlined in this thesis, having some means to measure the negative flow accurately is important. Else, creating a faithful digital twin will not be feasible. Unfortunately, no ratified method to determine the negative flow precisely using the equipment available in the NTNU compressor laboratory exist.

However, the current setup in the laboratory consists of two orifices, making it possible to improvise a method for measuring reversed flow. Having two orifices makes it possible to reverse one of them – that is, intentionally installing it the wrong way – and register the reversed signature, in order to compare with the other control-orifice (the other orifice). The plan for developing this method was therefore: examine the difference between the two orifices when oriented the same way, putting emphasis on areas where they overlap so closely that one signature can replace the other. If such an area exists, the orifice nearest the compressor can be reversed without further examining the correlation between the orifices for positive flow, saving some effort. With the second orifice reversed, the exact same experiments are repeated: static samples are collected within the region where the orifices confidently overlap; and some dynamic experiments are also made, though details about these will be clarified later, in Section 6.2.6. Finally, the signature between orifice 1 and 2 may be compared, and a correction factor may be found, using orifice 1 as a reference.

The first part of this process has been presented earlier, in Section 6.1.2. Figure 6.3 shows that the orifices are particularly overlapping in the region where $Q \in [0.5, 0.9]\ \mathrm{m}^3/\mathrm{s}$. Therefore, this region was selected to be the region where static samples would be collected from.

The second orifice was reversed, and static samples were taken over a period of at least $60\,\mathrm{s}$, resulting in Table 6.3. Plotting this data leads to Figure 6.4, which shows, while not perfect, it is clearly possible to use Equation 2.10 from ISO 5167-2 for reversed flow, at least under similar flow conditions as this experiment. The greatest contributing factor to the disparity is probably the bevelled surface on one side of the orifices, though looking into this is not the focus of these experiments.

Figure 6.4 shows that the reversed orifice, orifice 2, consistently underestimates the volumetric flow compared to orifice 1. For a perfect match, the static samples plotted in the figure should be on the

Test number	Compr. speed (RPM)	DV- position (% open)	Q, Or. 1	Q, Or. 2
1	9019.8	53.6	0.862	−0.832
2	9020.3	49.9	0.756	−0.736
3	9020.0	49.7	0.749	−0.727
4	9020.1	45.0	0.640	−0.606
5	9020.2	40.9	0.528	−0.486

Table 6.3: Data points from static tests with a reversed orifice. This data was used to plot Figure 6.4. It is emphasised that the accuracy of these measurements are not ± 0.001. The numbers are given with these many decimals so calculations and experiments done later can be compared to these values more easily.

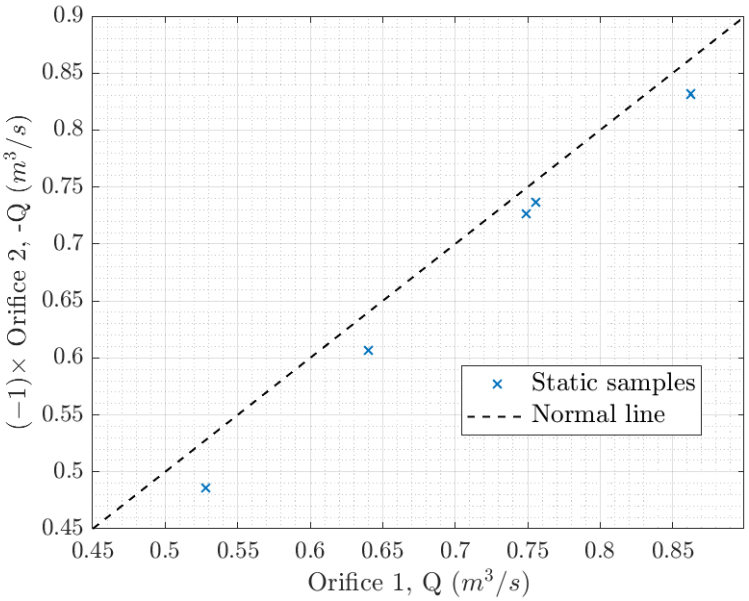

Figure 6.4: Disparity between orifice 1 and orifice 2, from static tests with a reversed orifice. Using data from Table 6.3. Orifice 2 (y-axis) is multiplied with -1 for clarity. Samples taken over a period of at least 60 s. This curve is not normalised to better show that the disparity appears to be quite constant.

dotted normal line. Since the signature from orifice 1 is taken to be the "true" response, shifting orifice 2's signature to line up with that of orifice 1 would be the primary objective of a correction factor in this case. Designing a correction factor to achieve this can be done in more ways than one. The difficulty is creating a correction factor which retains high validity, and that can function well, outside the region it is based upon. Because of the limited samples taken, and the limited region they were recorded in, there is no point contemplating anything more advanced than a quadratic correction factor. Using a cubic correction factor, or more, would just give a false sense of correctness, and is liable to only work inside the small, defined area. This is also assuming that enough equations can be created, so that the unknowns introduced by going for a higher degree equation can be determined.

Based on the signature in Figure 6.4, it seems creating a constant correction factor is the best option, as orifice 2 looks to underestimate the flow with a constant amount. Additionally, using a constant for the correction factor would be the easiest to create, and implement, as opposed to a linear, or a quadratic correction factor. As the name implies, a constant correction factor requires the variations to be somewhat constant for it to be effective, which in this case they were. The constant correction factor was created

by using Equation 6.1.

$$Q_{Or1} = (-Q_{Or2}) + C_{const} \quad \Rightarrow C_{const} = Q_{Or1} + Q_{Or2} \tag{6.1}$$

where C_{const} is the correction factor, and Q_{Or1} and Q_{Or2} is the volumetric flow calculated using Equation 2.15. Since orifice 2 is reversed, it must be written as a negative factor here, because the readings from orifice 1 and orifice 2 should cancel out when added together in an ideal scenario, i.e. $Q_{Or1} + Q_{Or2} = 0$. The answer is displayed in Table 6.4.

Using a linear correction factor would be a bit more comprehensive. Using a linear correction factor is generally a good compromise between the precision of a quadratic correction factor, and the reliability and ease of calculation of the constant correction factor. In order to solve the unknown introduced with going up one degree, it is assumed that when zero flow is measured on one of the orifices, both orifices measure zero flow. A seemingly reasonable assumption – especially for static experiments – which allows the removal of the constant factor in the linear equation, shown in Equation 6.2, simplifying the calculation a great deal. It should be noted, that using an assumption like the one above introduces errors if the assumption is wrong.

$$Q_{Or1} = C_{lin}\, Q_{Or2} + C_{const} = C_{lin}\, Q_{Or2} \quad \Rightarrow C_{lin} = \frac{Q_{Or1}}{Q_{Or2}} \tag{6.2}$$

where C_{lin} is a linear factor, C_{const} is a constant factor (here assumed to be zero), Q_{Or1} and Q_{Or2} is the volumetric flow calculated using Equation 2.15. The average value of Q_{Or1} and Q_{Or2} was used to find C_{lin}. It is unnecessary to use $-Q_{Or2}$ now, because this negative factor is covered by C_{lin} instead.

Using a quadratic correction factor is not possible without making yet another assumption. The problem is that it is not possible to know for certain (with the current data and tools available) which, if any, of the recorded volumetric flows reflect the actual true value. True in the sense that the sensor records the real value, with no error, meaning no correction is needed. Because of this problem, another assumption is needed so that the amount of unknowns equal the amount of equations. Else, it is not possible to iterate confidently. Unfortunately, no assumptions with any merit remain. One could assume one or more of the recorded data values to be correct, but the correction factor would lose credibility, because there is no way to be sure that the data values were actually correct. If more independent tests are made, and they all share some similarities, assumptions as these may be made with some confidence. But, as it stands with the tests already done, this is not possible.

Table 6.4 shows the values of the different factors depending on the type of correction factor selected. Evidently, while both are good, using simply a constant as a correction factor seems to be the best option, by far. This is strange. The only good explanation for it being this mismatched is that the earlier assumption is wrong. Namely, when one orifice registers zero flow, the other also registers zero flow.

And sure enough, Table 6.5 shows the average of the individual sensors during a standstill. While the Protran sensors are close enough to each other and zero, with some exceptions, both PCE-28 sensors record a severely exaggerated response.

Figure 6.5 shows how the different correction factors from Table 6.4 compare. The constant cor-

Correction factor	C_{const}	C_{lin}	**Average disparity from samples** in m^3/s	in $\%$
No correction factor	-	-	$3.4433 \cdot 10^{-2}$	5.6983
Constant	0.02946	-	$-4.0384 \cdot 10^{-16}$	$-5.7125 \cdot 10^{-14}$
Linear	0	-1.0469	$-2.3124 \cdot 10^{-3}$	-0.32709

Table 6.4: Two types of correction factors available for correcting the signature of reversed flow. It is highly recommended to use the constant correction factor, due to the assumption used for the linear correction factor being wrong. The relative average disparity (disparity in %) was calculated in this case with Equation A.6 from Appendix A4.2.

Orifice	**Sensor**	**DP-value** (mbar)	**Q** (m^3/s)
1	Protran DP25	0.0125	0.0207
1	Protran DP250	0.0878	0.0535
1	PCE-28 DP smar	1.2508	0.1985
AVERAGE, Orifice 1		0.4503	0.0909
2	Protran DP25	0.0184	0.0159
2	Protran DP50	0.0483	0.0254
2	Protran DP250	−0.0951	−0.0354
2	PCE-28 DP smar	−1.3694	−0.1323
AVERAGE, Orifice 2		−0.3495	−0.0316

Table 6.5: A standstill test taken before the experiments with reversed flow. The "DP smar" sensor is of the type PCE-28 (A1.2), while the others are Protran-type sensors (A1.1. During a standstill test, the compressor is not running, and all DP-gauges should ideally be zero. It is emphasised that the accuracy of these measurements are not ± 0.001. The numbers are given with these many decimals so calculations and experiments done later can be compared to these values more easily.

rection factor (drawn in red) is equal to, or better than the alternatives in all instances. Using a linear correction factor (drawn in yellow), even based on a faulty assumption, is slightly worse than the constant correction factor, but still better than using the raw data as is, in this region.

While the correction factors are satisfying as they are, it is alluring to try improving them. Particularly the linear correction factor. But, to create a new linear correction factor using data from Table 6.5 is not necessarily the best course of action. Doing so could reduce the legitimacy of the linear correction factor even further. Because the standstill test covers a region where orifice 1 and orifice 2 is known (from previous tests) to not match perfectly when both orifices are installed the correct way, orifice 1 will not work as a perfect substitute for orifice 2. Additionally, uncertainties are severe in this region. Therefore, some deeper prefatory statistical analysis is needed to establish a better substitute for the reversed orifice 2. It is necessary to use this embarrassingly delicate accuracy, because the constant correction factor fits marvellously, and if the "new" linear correction factor cannot outperform the already-fitting constant correction factor, there is little point spending so much effort on it. In order to improve the accuracy and validity of the correction factors further, it is necessary to preform more experiments with reversed flow. Unfortunately, due to time constraints, this was not possible.

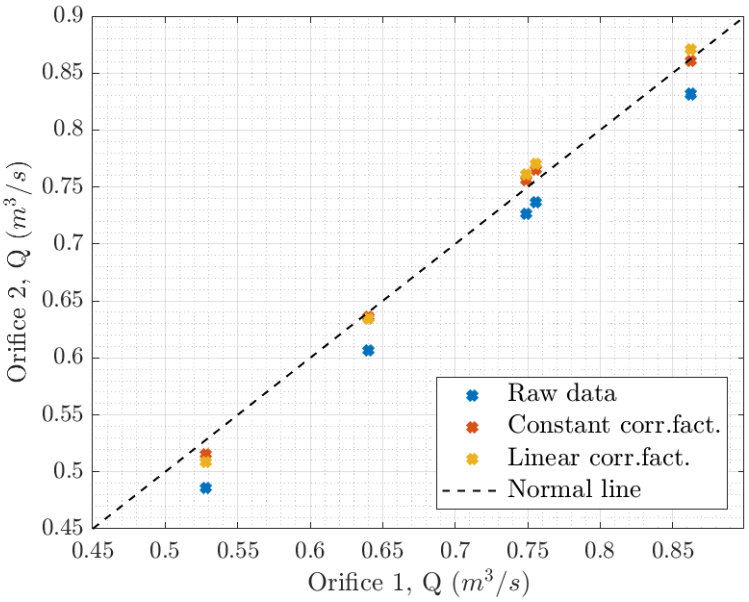

Figure 6.5: Displaying correction factors and how they compare. This curve is not normalised so actual differences between the different correction factors can be properly displayed.

Summarising this subsection, it was examined whether or not ISO 5167-2 could be used for reversed flow as well. It was certainly found to be possible for this compressor rig, albeit not perfectly so. Two correction factors – one a constant correction factor; the second a linear correction factor – was created and introduced to help alleviate the imperfection. Both preform better than the raw data, but surprisingly the constant correction factor best fits the samples studied. It turns out the assumption used to create the linear correction factor was wrong. But, since the constant correction factor preformed so well, it was decided to just use that one instead. Thus, it has been established, with good certainty, that reversed flow deviates from regular flow with a constant factor.

6.2 Dynamic Experiments

Dynamic experiments are experiments conducted with transient operation conditions. For the experiments in this thesis, that means they are experiments of the profile test-type. These tests are the most realistic in describing how the system would normally react to an external change. They give a good insight in the instabilities of the region, and show surge explicitly. However, as mentioned briefly at the start of Section 6.1, there are some small discrepancies between profiles taken mere minutes between each other. This casts some doubt over the stability and repeatability of the dynamic experiments.

The purpose of these dynamic experiments can be summed up to the following points: log the system response so that an approximate compressor curve can be made, showing the probable system response; map the violent tendency of surge; and map the reduced and reversed flow.

6.2.1 Logging frequency

The logging frequency determines how often sensor data is recorded. Determining the correct logging frequency is a fine balance of recording too much, or too little. Record too little, and important signatures

and responses might be lost, or particular to low-flow and surge cases; the violent signature surge has, might seem to be somewhat tranquil, if data is not recorded with high enough frequency. Recording too much results in huge data-files, that might become too large to handle effectively, with little extra information gained.

The PXI logging equipment measures the DP signature of the pressure sensors with an electrical signal. For the sake of brevity, the details will be omitted, but the measuring frequency of the equipment is 20 kHz, allowing for a very high resolution. Recording 20 000 times every second is, however, not at all necessary. Based on earlier experience, a logging frequency of at least 2 Hz - 4 Hz has been found earlier to be adequate in dynamic experiments [25].

During the first few dynamic experiments where surge occurred, the sensor readings were not as violent as expected. Figure 6.6 shows the recorded response of a profile test where this was noted. Summarily it was decided that the logging frequency of the sensor equipment should be further increased. It had already been increased from 2 Hz to 4 Hz before dynamic experimentation started.

By increasing the logging frequency to 10 Hz a typical profile-test produced Figure 6.7. This figure has a signal more typically associated with surge; pronounced fluctuations around zero, or minimal flow.

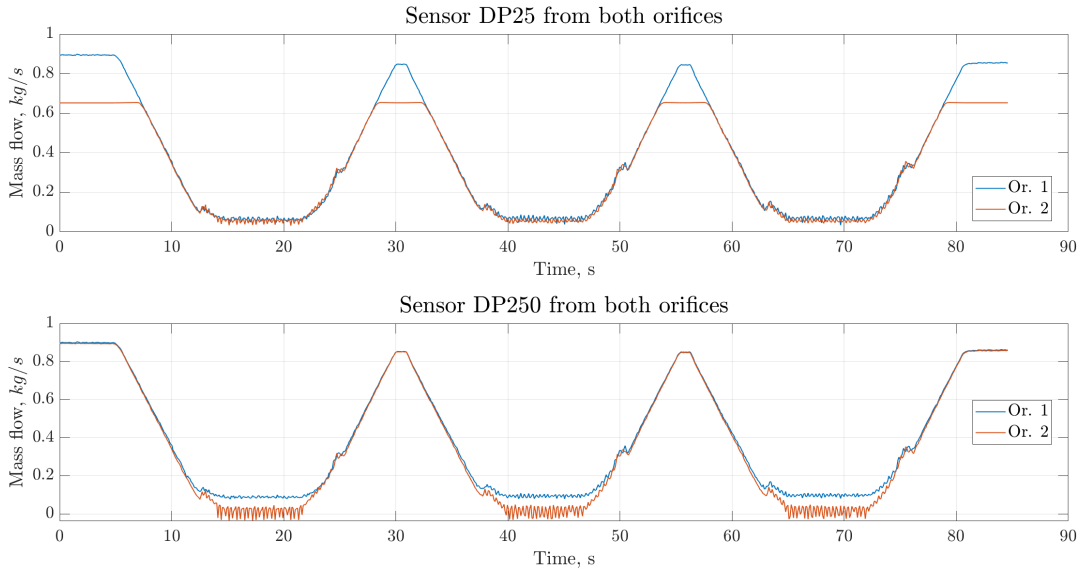

Figure 6.6: Result showing DP sensor readings from a typical profile-test, recorded with a logging frequency of 4 Hz. The upper plot shows sensors with a range of ± 25 mbar, while the lower plot shows sensors with a range of ± 250 mbar. *Or. 1* refers to a sensor at orifice 1, while *Or. 2* refers to a sensor at orifice 2.

In the upper plot of Figures 6.6 and 6.7, the plot showing the calculated mass flow using the ± 25 mbar sensors, orifice 1 and orifice 2 diverges when the flow increases above $\dot{m} \approx 0.6\,\mathrm{kg/s}$. Here, using the data recorded on orifice 2, mass flow will not increase further, and just continue in a straight line. This is because the sensor on orifice 2 becomes saturated, and cannot register any higher differential pressures, leading to a seemingly constant mass flow. This very clearly shows that the DP25 sensor on orifice 2 is only viable for $\dot{m} < 0.6\,\mathrm{kg/s}$, or about $Q < 0.5\,\mathrm{m^3/s}$.

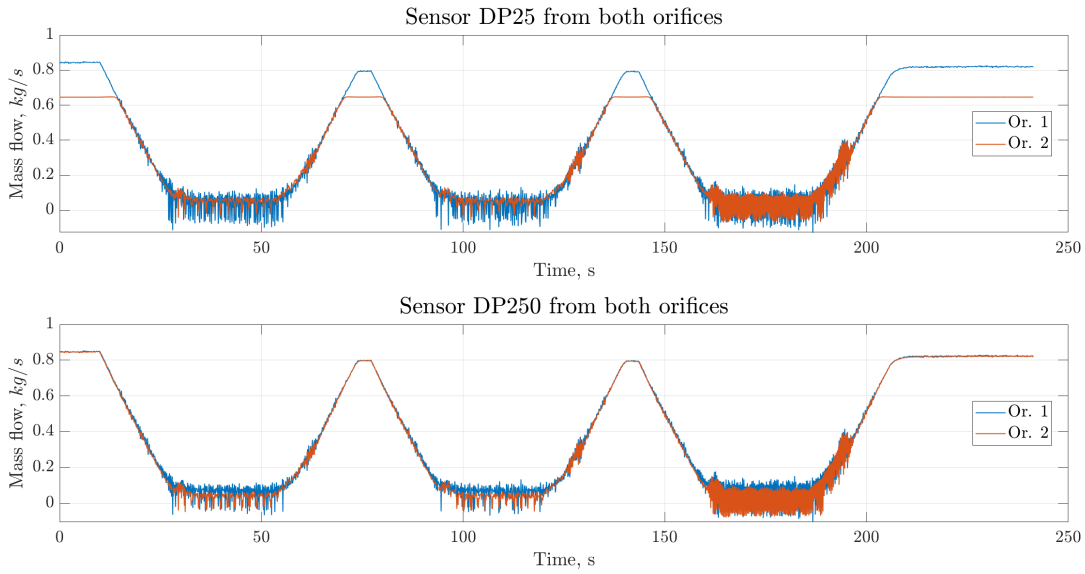

Figure 6.7: Resulting DP sensor readings from a typical profile-test, with logging frequency set to 10 Hz. he upper plot shows sensors with a range of ± 25 mbar, while the lower plot shows sensors with a range of ± 250 mbar. *Or. 1* refers to a sensor at orifice 1, while *Or. 2* refers to a sensor at orifice 2.

6.2.2 Sensor tubing

Even though Figure 6.7 is a substantial improvement over Figure 6.6, it still retains a somewhat strange response. Looking at the first two dips, there is a definite increase in response when $f = 10$ Hz – compared to $f = 4$ Hz – but it is still somewhat contained. Especially strange is the fact that orifice 1 has a more pronounced response than orifice 2. One would expect it to be opposite, considering that orifice 2 is right next to the compressor, while orifice 1 is quite a bit upstream of orifice 2. In contrast, the last dip looks just like one would expect; violent, rapid fluctuation around zero flow. Further increasing the logging frequency does not solve this particular issue. Something else was reducing the pressure fluctuations.

Since the DP sensors on orifice 2 was connected by approximately 1 m long tubes and mounted some distance away from the orifice, it felt natural to examine whether or not this had a significant impact on the overall pressure-reading. With data from the *"long tube"* configuration quickly recorded in a standard profile test, the tube length for one sensor – the DP50 sensor – was shortened to about 15 cm, after which a standard profile test was done to see the impact of this short tube. Figure 6.8 shows the response recorded from that test, and data from a previous test where the DP50 sensor was fitted to a long tube.

And as Figure 6.8 shows, the response was a lot better with short tubes fitted. At all three dips, the response was the same for the short tube; clear fluctuations around zero, a good response. While the long tube showed no significant fluctuations for the first two dips. But, this one data-set provides too little data to draw lasting, conclusive results about the necessity of short sensor tubing. These tests might be an indicator that shorter tubing is needed, though it might also be that the response recorded in this long-tube test was a fluke. However, it must be mentioned that one earlier profile, with the same logging frequency and recorded with the same long-tube configuration, showed a similar, low-response as this long-tube test.

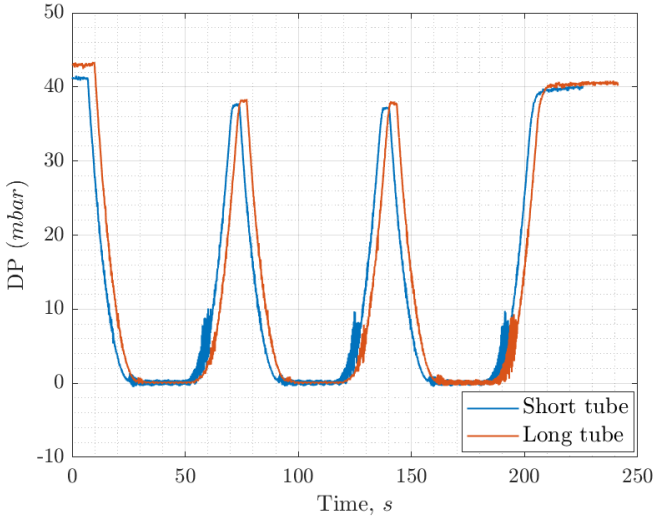

Figure 6.8: Showing the DP recorded by the $\pm 50\,\mathrm{mbar}$ sensor located on Orifice 2. The red line shows the response when the tubes connected to the sensors are long (about $1\,\mathrm{m}$), while the blue shows the response when the tubes are short (about $10\,\mathrm{cm}$).

With no apparent benefits gained at having long tubes, it was decided to shorten the sensor-tubes at orifice 2, to be about $15\,\mathrm{cm}$. Even though there was no clear, definite indication that shorter tubes are necessary, they were shortened because it did not take much time, or effort to do. Doing more tests would have resulted in one of three conclusions: longer tubes would not impact the DP readings; longer tubes does indeed impact DP readings, and tubes must be shortened; or, lastly, no confident conclusion could be drawn. No matter which of those three cases it would end up being, none of them would mean shortening the tubes would negatively impact the results. Therefore, the tubes were shortened.

6.2.3 Disparity between orifices

Earlier in this thesis, the relationship between orifice 1 and orifice 2 has been mostly simplified; they have been treated as if they at all times give the exact same results, with an exception from the latter half of Subsection 6.1.3. There is however a bit more nuance to their relationship, which this subsection will attempt to describe in more detail.

Though very similar, orifice 2 has an ever so slightly a fuller surge-response, as Figure 6.9 shows. Here, orifice 2's response was drawn first to highlight the areas where it is more fleshed out than orifice 1. While not by much, and only showing one of many recorded profiles, Figure 6.9 highlights a recurring theme; orifice 2 has a fuller response near surge than orifice 1. This is particularly visible in the first two trips. Observed in the last trip of this figure, is a small phenomena which is further commented and documented in Section 6.2.5.

This typical response seen in Figure 6.9 is not at all unexpected. For one, orifice 2 is located much closer to the compressor than orifice 1 is, giving less possibility for friction to reduce fluctuation effects, and having a significantly smaller volume between the compressor and itself. As the air-volume between the compressor and the given orifice is compressible, much of the back-flow signature the compressor experiences may be lost by the time the back-flow reaches the orifice in question. This effect is increased

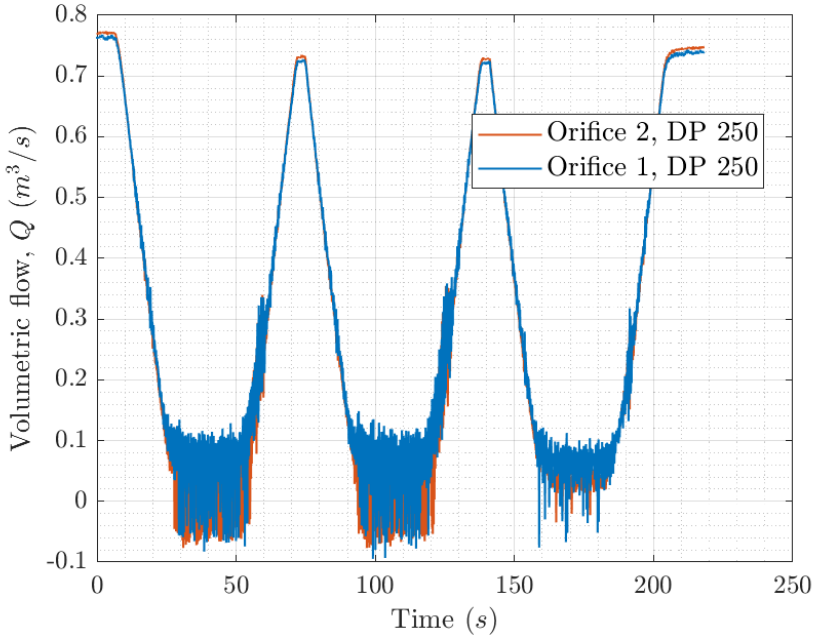

Figure 6.9: The volumetric flow during a standard profile-test, as measured by the DP250 sensors. The sensor located at orifice 1 is in blue, while the one at orifice 2 is in red.

the more volume there is between the orifice and the compressor. Secondly, orifice 2 is the smaller of the two orifice plates, hence it is creating the highest pressure drop, and a higher pressure drop is more accurately read by the sensors.

Figure 6.10a shows a typical result gained when calculating the volumetric flow on both orifices using all sensors, then syncing the answers with respect to time, before plotting the result with orifice 1's calculated Q-value along the x-axis, and orifice 2's calculated Q-value along the y-axis. This plot is a little complicated, so the calculation procedure will be reiterated here. First, Q was calculated for all sensors, regardless of orifice. All sensors were included, because there was no sensor that was decisively off at the lower flows, compared to the other sensors on the same orifice. Since all DP-sensors have the same logging frequency, the vectors containing the DP-data were already synchronised with respect to time. Thus making the *orifice average* easy to calculate. After this orifice average was found, the two remaining vectors – one containing orifice 1's average calculated Q, and one containing orifice 2's average calculated Q – were plotted against each other, resulting in the blue curve seen in Figure 6.10a. If the calculated average of both orifices had been the exact same, each vector element would have corresponded with each other, resulting in the dotted normal line seen in the same figure.

Figure 6.10a shows orifice 2 is better at registering deep surge – or, reversed flow – than orifice 1. Volumetric flow calculated by using DP sensors from orifice 2 fluctuates around zero flow, while by using sensors from orifice 1, it fluctuates around $0.1\,\mathrm{m}^3/\mathrm{s}$, giving the signature shown in Figure 6.10a, where the blue line deviates from the normal line near low flows. The figure also shows when the onset of surge and instability seem to occur. Being mostly calm and consistent for higher flows, tumultuous tendencies really occur when $Q \approx 0.35\,\mathrm{m}^3/\mathrm{s}$ and lower.

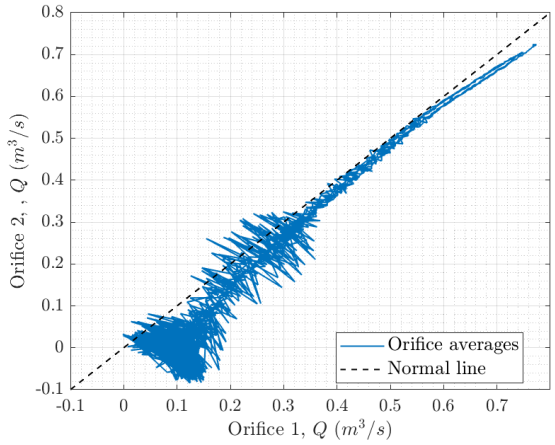

(a) Average volumetric flow (Q) calculated by all sensors on orifice 1, plotted against average volumetric flow calculated by all sensors on orifice 2 for a standard profile-test. The dotted black line is a normal line, showing where the orifice average should have been if both orifices registered the exact same volumetric flow.

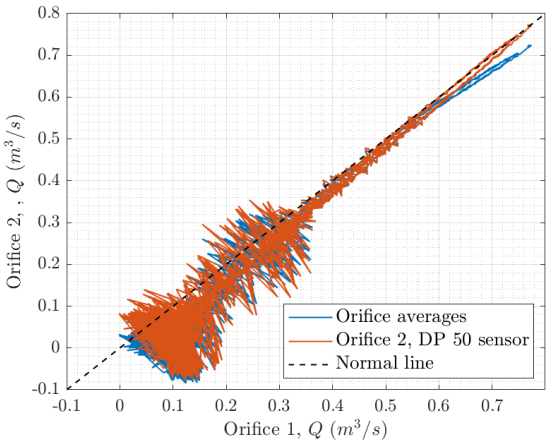

(b) Showing the same as Figure 6.10a, with orifice 2's DP50 sensor drawn on top in red.

Figure 6.10: Figure 6.10a shows the disparity between the average volumetric flow (Q) measured on the two orifice plates. Figure 6.10b shows this also, and additionally how the individual sensor DP50 on orifice 2 is in comparison to the average volumetric flow measured on orifice 1. Both plots are from the same experiment, which was a standard profile-test.

The DP50 sensor located on orifice 2 seems to be the best sensor for orifice 2. This is because it can cover the entire range usually looked at during reduced flow and some regular flow in this thesis, (that is, $Q \in (0, 0.7\,\mathrm{m}^3/\mathrm{s}]$, during a regular profile-test), while also delivering a finer signal – allowing for more detail – than the alternative DP250 sensor on the same orifice. During a regular profile test, all sensors on orifice 2 are extremely similar in the "dips" of the profile, except for the *DP- smar* sensor. This sensor gives a slightly lower response compared to the other three.

Compared to the *DP-smar* sensor, DP50 seems to react more responsively, as the DP smar sensor never has the same amplitude as the other orifice 2 sensors during surge. In Figure 6.10b, the DP50 sensor on orifice 2 is highlighted, because it seems to be best sensor on orifice 2 for recording the differential pressure, when compared to the average signature from orifice 1, and the average for orifice 2. Therefore, DP50 has been selected as the basis-sensor for further examination of reduced and reversed flow. For regular flow, this sensor is saturated before the maximum response is reached. When this happens, the average signature from DP250 and DP smar is used instead.

6.2.4 Bull nose

In this subsection, the attempted use of the bull nose as a secondary means to measure mass flow is described. It includes what the idea was, how it was tested, and at the end, a brief conclusion.

An attempt was made examining whether or not the bull nose of the compressor could be used to determine the mass flow going into the compressor, by looking at changes in the differential pressure over the bull nose. As the bull nose presents a change in geometry in the flow-tube – reducing the overall surface area of the flow in this case – it should theoretically be possible to use it as way of registering any

changes in flow, by registering the differential pressure across this change in geometry. If it turned out to be possible, the bull nose would be even closer to the compressor than the second orifice, and could possibly be used to help confirm any observations made on the second orifice. Depending on the clarity in the observations, the second orifice could also become superfluous if the registered response was clear enough. Summarised, the purpose of this small experiment was to see whether the compressor bull nose could be used to accurately discern flow changes.

In contrast with just using an orifice, there is no accessible standard applicable for measuring flow using this bull nose. However, assuming a different response could be read for different volume flows, it would be possible to create an equation for calculating the volume flow using orifice 1 and 2 as a reference.

A DP sensor of the Protran PR3202 type (Appendix, A1.1) with the range of $\pm 10\,\mathrm{mbar}$ was set up over the bull nose profile, with the first pressure recording some $20\,\mathrm{cm}$ before the start of the nose, and the second pressure recording at the start of the IGVs. A standard profile test with the downstream air tank was done and the response was recorded.

Figure 6.11 shows the resulting profile recorded. It is not at all apparent what happens from just looking at this particular DP response. Other figures are included in the Appendix (A4.3), showing, among other things, how the compressor speed during the same test is a lot more useful at ascertaining a change in operating conditions, compared to this response.

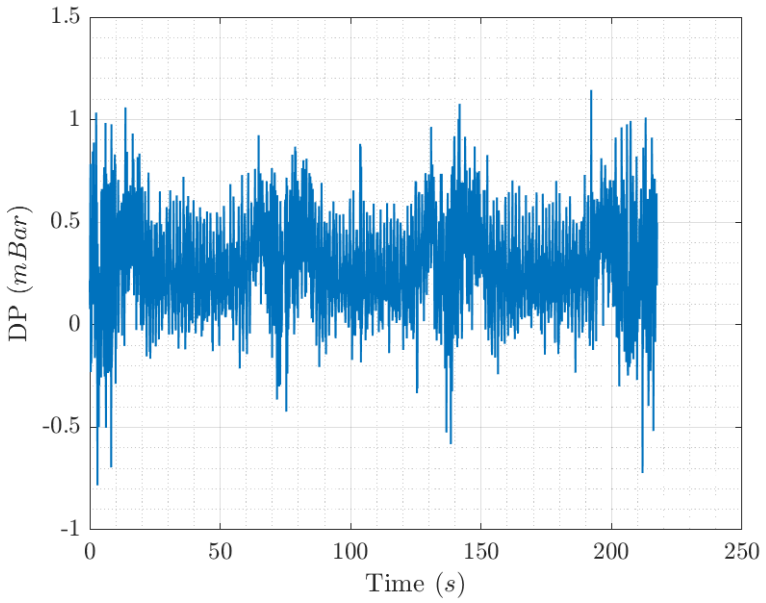

Figure 6.11: Differential pressure signature over the compressor bull nose during a profile test with a pressure tank connected to simulate a large downstream volume.

Granted, some response was detected on the bull nose. Though with this one experiment, it is not possible to confidently determine exactly what happened with the operating conditions by looking at this figure alone. Could it ever be possible? Maybe, but with a lot of effort, and dubious gain. For, if one only looks at what the response fluctuates about – and not the entire response with its varying amplitudes going one way or the other all the time – and enough experiments are made, then maybe it would be possible to confidently say that the volumetric flow increased, or decreased, without considering any

other graphs. But it should be remembered that Figure 6.11 represents the results from a very dramatic change in operating conditions. And if this much doubt is raised for a dramatic change, there is no point trying to pinpoint smaller changes, never mind determining exactly what happened. Since this test was conducted with the downstream pressure tank connected, the test had the best prerequisites for detecting negative flow, or something like a dramatic back-and-forth fluctuation. None of this is any apparent from the figure. Somewhat paradoxically, it seems that there is less violent fluctuation when surge occurs.

In conclusion, it appears to be a good idea on paper, but it is not feasible with the current setup in the laboratory. It might be doable, though on the surface level, the costs outweighs the gains by a considerable margin. Simply using the second orifice alone, or the compressor RPM, or instead the pressure difference across the compressor is a lot less painful and more accurate.

6.2.5 Reduced flow

While most of the difficulties in obtaining data for dynamic flow has been covered earlier, some challenges remain. These challenges will be covered in this section. Additionally, this section will look closer at what the data actually shows, and if it is possible to predict the onset of surge. Towards the end of this subsection, the focus switches to examining how the dynamic response compares to the static tests taken earlier, and some preparations for a combined curve.

Subdued response

A strange phenomenon was observed during multiple dynamic tests. This can be seen in the third "dip" in Figure 6.12, the first two "dips" in Figure 6.7, with some more examples included in the Appendix A4.4. Suddenly, and without any apparent reason, the response "quietens"; transitioning from a violent fluctuation with high frequency and amplitude in the previous dips, to a relatively calm, semi-fluctuating response.

First, it was believed to be a fluke, but as it kept happening, it became clear that was not the case. It happened at least once for all regular profile-tests that were made. The effect however, was anything but regular. Sometimes, as in Figure 6.7, and other experiments that were not recorded, two of the dips were affected. Other times, such as the one in Figure 6.12, only one dip was affected. Sometimes, the first dip had a low response, some other times, the second, or the third had this reduced response.

All temperature sensors, and all other pressure sensors were then examined for irregularities. The temperature sensors showed nothing out of the ordinary; a temperature fluctuating in synchronisation with the opening and closing of the compressor discharge valve, with a total overall temperature increase of around $1\,^{\circ}\mathrm{C}$. All pressure sensors showed the same subdued response as the DP sensors on the orifice for the third dip.

After finding nothing out of the ordinary on the pressure and temperature sensors, the compressor torque was examined. It was conceivable that the subdued signature was because of the system being in some kind of fluid-, or thermodynamic resonance. Figure 6.13 shows the torque for the same profile. There is nothing exceptional about the third dip; nothing out of the ordinary can be observed there.

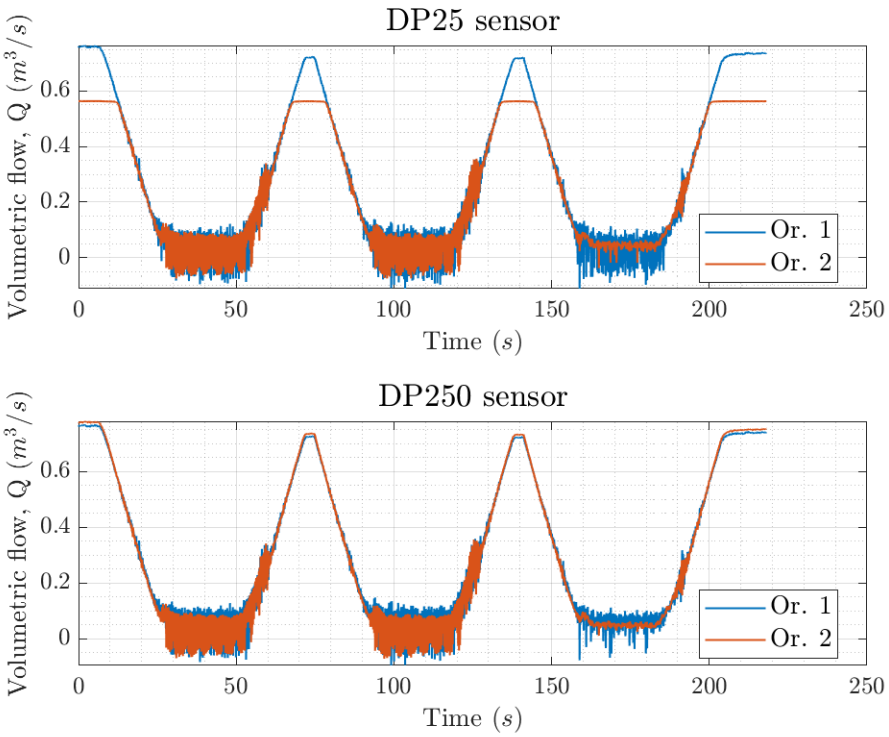

Figure 6.12: Showing the response on a regular profile-test. The upper plot displays the volumetric flow as measured by the DP25 sensor on both orifices. Orifice 2 is saturated for the higher flows, explaining the straight line it reports between the "dips". The lower plot displays the volumetric flow as measured by the DP250 sensor on both orifices. This particular profile is known as Profile 1 form the 05.04 experiments.

In parallel with these regular profile tests, some experiments were made with the downstream pressure tank connected to the system. Experiments with this tank had not been made earlier in relation to this thesis because it had not yet been fully integrated into the compressor system. The downstream pressure tank has been described in Section 3.1 . Importantly for this discussion about the reduced response-phenomena, when the downstream pressure tank was connected, the phenomena disappeared. For all experiments done with the surge-volume connected – that means, with the downstream pressure tank connected – no reduced response was ever observed. As such, no more pursuit after the reason behind the phenomena was given, because it seems rather irrelevant. After all, using the surge-volume is what one should do, because it gives a much nicer, and more realistic response than when not using it. This reduced-response phenomena is just one more argument for always using the surge-volume in dynamic tests.

The Downstream Pressure Tank, *"S-volume"*

As described in Section 3.1, this downstream pressure tank is a tank of $3\,\mathrm{m}^3$, connected to the tube leading away from the compressor discharge valve. It builds a small pressure difference when the compressor is in regular operation, but it helps simulate a more realistic system by providing some much-needed downstream volume.

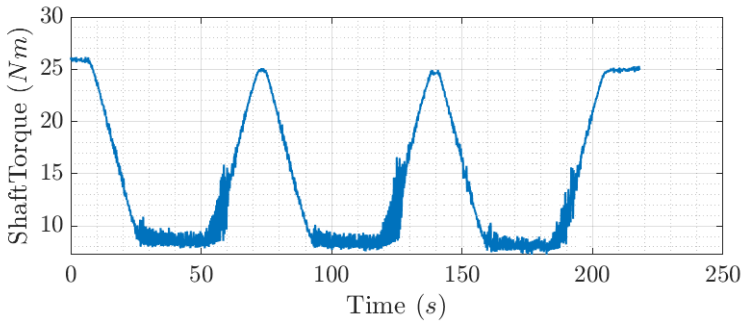

Figure 6.13: Shaft torque during Profile 1 from the 05.04 experiments (same as Figure 6.12).

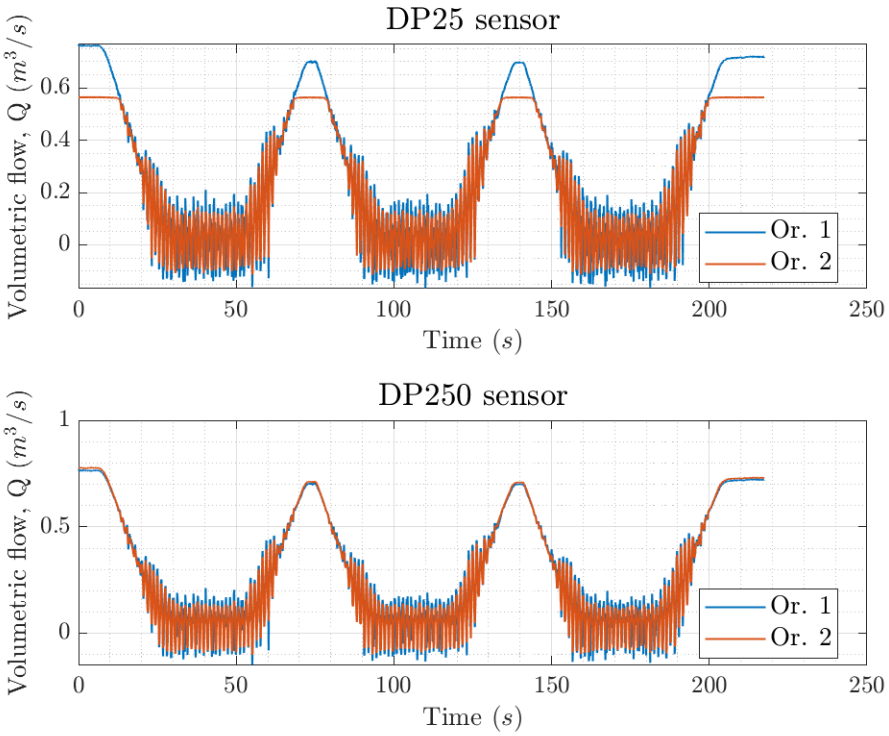

Figure 6.14: A profile test with the downstream pressure tank connected.

When the downstream pressure tank is connected to the system, and the compressor enters surge, this pressure tank provides enough downstream volume to affect the compressor surge substantially. Figure 6.14 is a plot of the volumetric flow of a profile test with the downstream pressure tank connected. It is a lot easier to see when instabilities first occur – around $Q = 0.5\,\mathrm{m}^3/\mathrm{s}$ – and when full surge occurs, compared with regular profile tests, like the one displayed in Figure 6.12.

Scatter Plots of Profile Experiments

The scatter plot of three reduced flow profiles, recorded the 5th of April, is shown in Figure 6.15 with one colour for each profile. Two of the profiles are of the regular profile-test type, while the one called "S-volume" is a profile-test done with the downstream pressure tank connected. All three profiles overlap nicely, but not perfectly; no specific area distinctly separates any of the profiles from each other. That being said, the profile is definitely more violent near zero flow, with the spread of the scatter visibly

increasing in size. Also, the profiles seem to be slightly different, hinting to a low repeatability in the dynamic experiments.

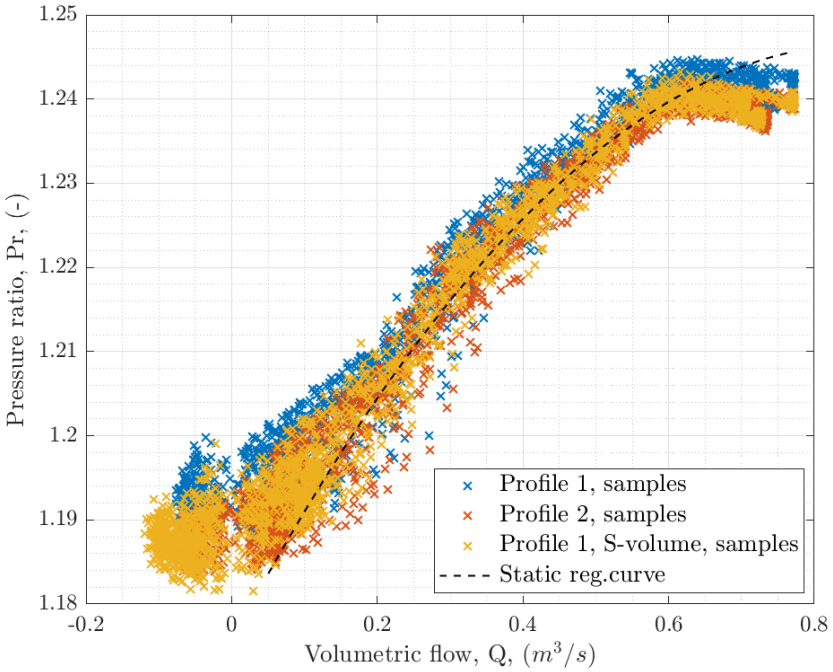

Figure 6.15: Scatter plot showing three different profile tests, separated by colour, and the "*static regression curve*" from earlier experiments, described in Section 6.1.2. "*S-volume*" represents a test where the downstream pressure tank is connected to better simulate a realistic system. The scatter plot is made of data exclusively from the DP50 sensor.

Figure 6.15 also includes the regression curve from earlier static experiments. The scatter plot follows this line very well when $Q > 0.2\,\mathrm{m}^3/\mathrm{s}$, but less well as the static line skewers and overestimate the volumetric flow. This overestimation is probably because the static regression curve consists of the average data from both orifices, and orifice 1 is known to overestimate at lower flows, compared to orifice 2, as discussed before. Unfortunately, the DP50 sensor was not yet mounted for the experiment where the static curve was calculated, and therefore it is not possible to isolate the DP50 response in the static samples. And anyways, the uncertainties of the data when $Q < 0.2\,\mathrm{m}^3/\mathrm{s}$ are huge, as Section 6.4 shows.

Until now, using regression curves of the second degree have been enough to reflect the development well. But, looking at the profile in Figure 6.15, it seems reasonable to discontinue regression curves of the second degree, in favour of third degree regression curves. The curves of Figure 6.16a are second degree regression curves based on the scatter plot. Comparing this figure with the scatter plot, it looks more akin to the regression curve from the static experiments. Therefore, like the static curve, they do not properly capture the curve-development, making the primary objective of creating a continuous compressor curve more arduous, or even impossible.

However, in Figure 6.16b there are instead third degree regression curves of the same scatter plot. Perhaps not surprisingly, these regression curves capture the development better than the second degree curves. Therefore, in order to get a more continuous curve when combining all compressor curves into

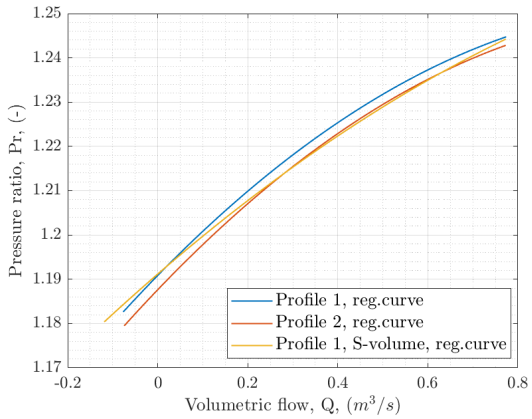

(a) 2nd degree regression curves of the scatter plot in Figure 6.15.

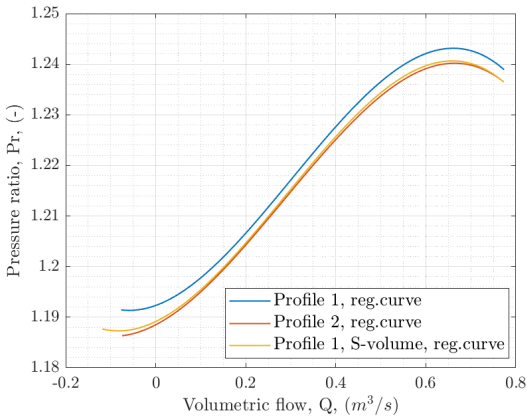

(b) 3rd degree regression curves of the scatter plot in Figure 6.15.

Figure 6.16: Showing regression curves of varying degree, all based on the points in the scatter plot from Figure 6.15.

one, third degree curves have to be selected for this region.

These curves from Figure 6.16b also show what the scatter hinted at; dynamic experiments seem to have low repeatability, since the different profiles are not directly on top of each other. It could probably be the temperature differences in the profiles, since the experiments are taken one after the other, with little chance for the entire system to cool down to the same temperature levels before for all the tests.

6.2.6 Reversed flow

In this subsection, the dynamic experiments taken with the second orifice reversed will be analysed. Results will be compared to the static curves developed in Section 6.1.3.

With the second orifice reversed, and by recording the sensor output from the DP50 sensor through two regular profile-tests, and two profile tests with the downstream pressure tank connected, the plot in Figure 6.17 was obtained. Contrary to the scatter plot created with the reduced flow experiments, this plot is unstable in the middle region of the plot, while being somewhat stable at flows where $Q < -0.4\,\mathrm{m}^3/\mathrm{s}$, with stable fluctuations around zero flow. Despite these instabilities, it is easy to see the overall trend in the data.

Comparing the profile responses to the static regression curve, they match fairly well for the most part. The static regression curve starts in a region that was not tested dynamically, but it has been extended to predict the dynamic profiles. All the way up until the unstable region in the scatter plot, the regression curve matches perfectly. Unfortunately, it drops off too early after entering the stable region, and does not predict the dynamic flow well near zero flow. In hindsight, it is not hard to see that this region lies too far away from where the five static samples were measured to be predicted accurately. Especially as the compressor map does not have a particularly quadratic development when the entire range in Figure 6.15 is considered. It looks more to be a third degree curve, which is another good argument for why the regression lines of this scatter plot are best represented as third degree curves, as

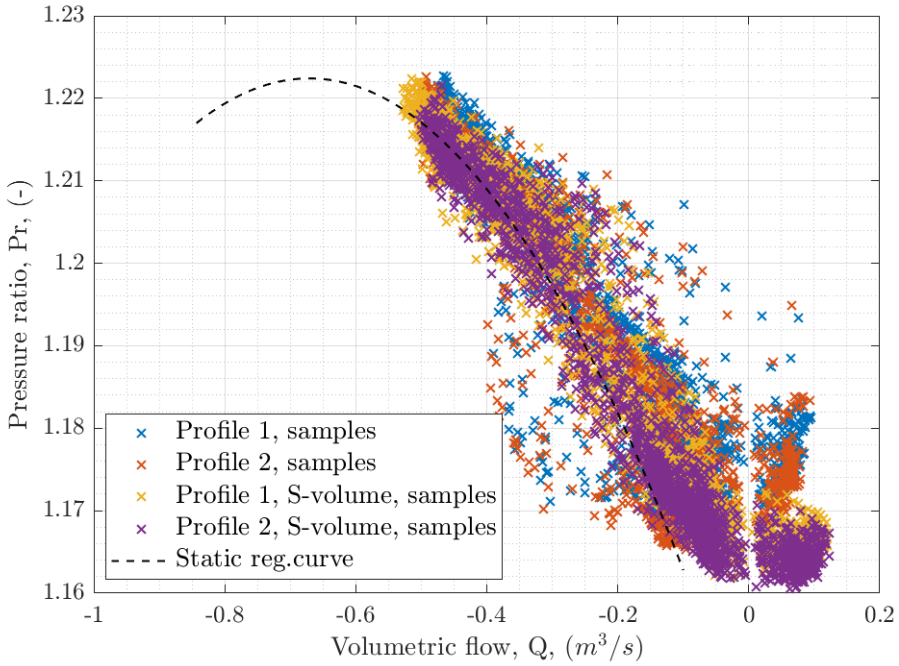

Figure 6.17: Scatter plot showing: two regular profile tests, referred to as *"Profile 1"* and *"Profile 2"*; two profile tests with the downstream pressure tank connected, referred to as *"Profile 1, S-volume"* and *"Profile 2, S-volume"*; and a *"Static regression curve"*, calculated earlier in Section 6.1.3 and extended to cover the current region.

in Figure 6.18.

Because of the instabilities in the scatter plot, it is easier to see the trends from the experiments in Figure 6.18. For example, how well the static regression curve fits some part of the plot, and how this regression curve drops off. Although the regular profile tests and the S-volume tests are mostly consistent, they distinctly separate near zero flow. This is well reflected in Figure 6.18. Near zero flow, the regular profiles have a slightly higher pressure ratio over the compressor when they fluctuate around zero flow, giving the regression curves a sudden up-tick.

Using the static samples from Section 6.1.3, it was attempted to make the static regression curve a third degree curve following the profiles more closely, but alas, the profiles are too far outside the valid region of the regression curve. The result from that attempt was a curve which fit the profiles far worse than the current regression curve.

Worth noting about the scatter plot and its apparent instability; regular profiles experience the most disturbance. The resulting profiles from tests where the downstream pressure tank was connected are very stable, in comparison. In Figure 6.19, the regular profiles have been separated from the S-volume profiles to better show this difference in stability. Proving that using the downstream pressure tank gives more stable results.

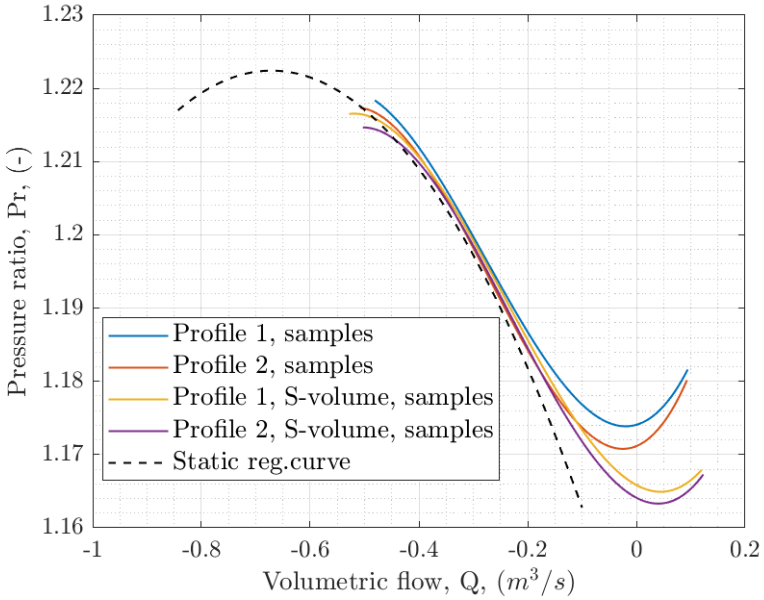

Figure 6.18: Regression curves for the scatter plot based on the reversed orifice. These curves are regression curves of the third degree, same as the regression curves for the reduced flow. Also shown is the static regression curve calculated in Section 6.1.3 and extended to fit the region.

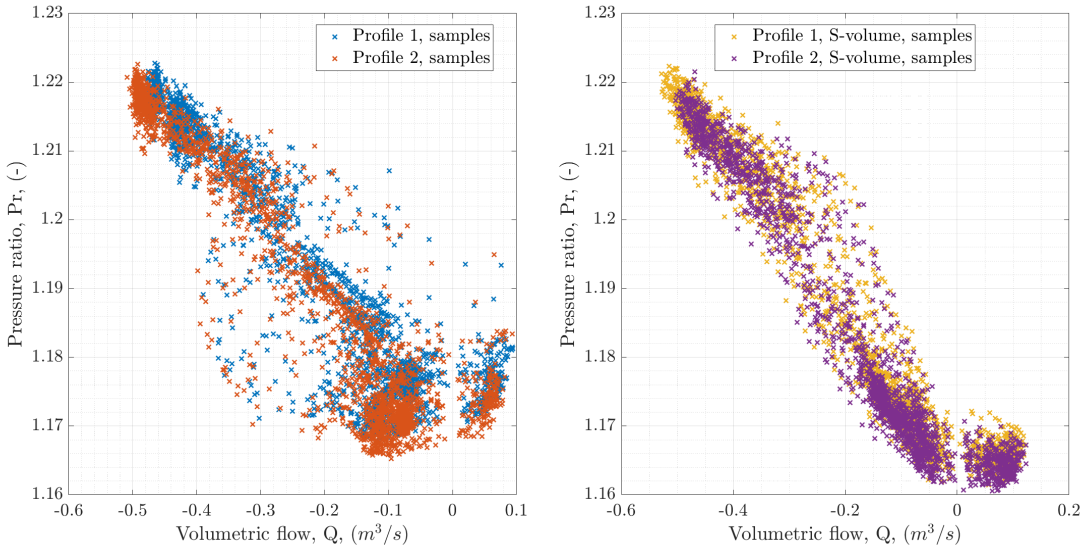

Figure 6.19: Same as Figure 6.17, except regular profiles and profiles with the downstream pressure tank connected have been separated in two different plots, to further emphasise the stability difference. Additionally, the static regression curve has also been removed.

6.3 Combined compressor curve

In this section, data from both static and dynamic experiments will be combined, and analysed together. The attempt to create one complete, continuous compressor curve will be made in this section. Additionally, an attempt at refining the raw signature of some dynamic profiles, to remove unwanted regions in the data, will be made.

6.3.1 Continuous compressor curve

Combining all previous compressor curves into one plot yields Figure 6.20. The different curves in the figure are added directly, with no correction factors yet applied. From the figure, it seems as the middle curves, the curves representing reduced flow, is situated a bit too high compared to the other curves.

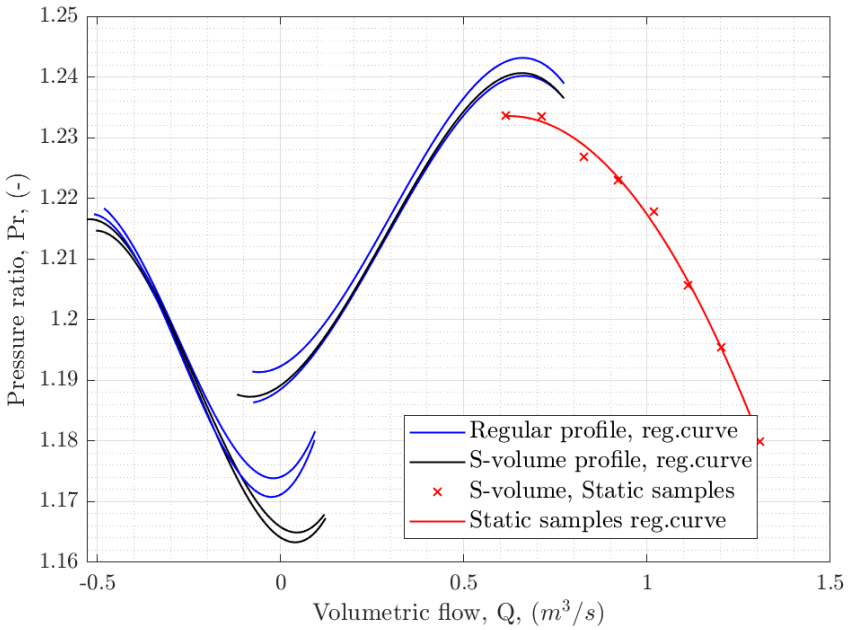

Figure 6.20: All regression curves from the compressor added in one plot. The four curves in $Q \in [-0.5, 0.1]\mathrm{m}^3/\mathrm{s}$ form the *"reversed flow"* region, the remaining three blue and black curves in $Q \in [-0.1, 0.6]\mathrm{m}^3/\mathrm{s}$ form the *"reduced flow"* region, while the red curve forms the *"regular flow"* region. The curves from the figure are defined in the Appendix in Table A4.5.1.

Expecting continuity between the reduced flow and reversed flow regions is far-fetched. Around zero flow the stability and repeatability is low, making uncertainties high. This low stability is evident in the scatter plots from Figures 6.15 and 6.19, and the repeatability is low because of the low-response phenomenon described in Section 6.2.5, and because the different profiles seem to vary somewhat, as the scatter in Figure 6.15 show.

Figure 6.21 shows a highlight of the region around zero flow. The scatter points are everywhere, especially for the plot from the reversed orifice tests. There, the regular profiles are particularly unstable, showing more difference within one profile, than there is between the different profiles. It should be noted, that some of the extreme points from these regular profile tests are not properly shown in this plot. They can be seen in Figure 6.19, where $Q < -0.2\,\mathrm{m}^3/\mathrm{s}$. Due to all this instability, expecting the

regression curves based on these scatter plots to be continuous is unrealistic. However, all is not yet lost, as the S-volume tests were more contained and although they were also quite unstable, they showed a clear tendency, which could be useful, especially if a proper correction factor can be found to link them together with the signature form the reduced flow tests.

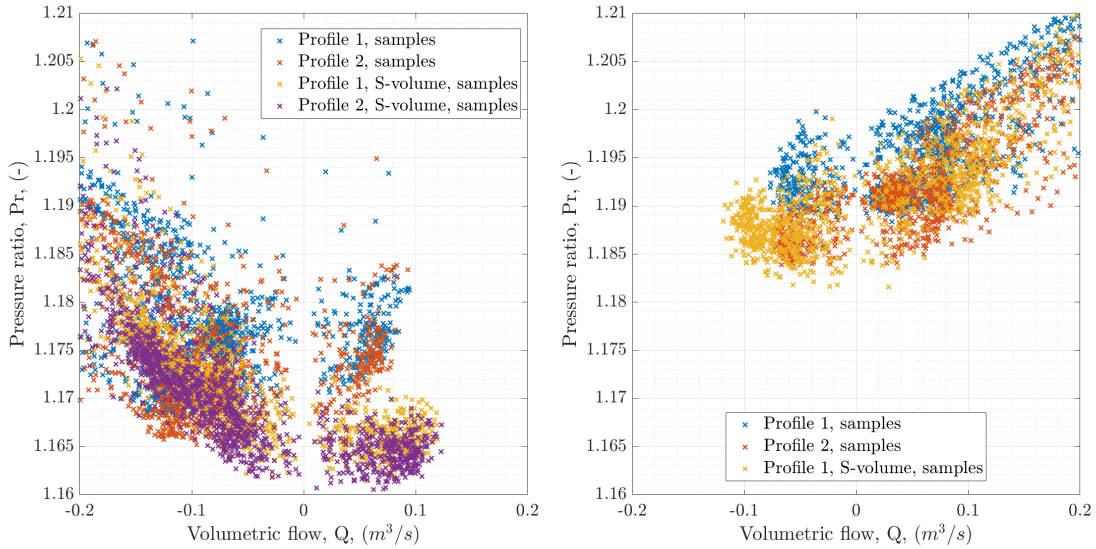

Figure 6.21: Highlighting the region around zero flow to emphasise its inherent instability. The left side plot is made with data from the reversed orifice tests, while the right side plot is made with data from the reduced flow tests.

In Figure 6.22, the static correction factor from Section 6.1.3 has been added to the region with reversed flow. As a result, the curves representing S-volume tests line up quite well. Meanwhile, the regular profile tests are even farther from uniting in one continuous curve. Though, as earlier discussed, the S-volume curves should be treated with priority, as they are more stable and realistic, while the regular profile curves may be ignored. Therefore, the loss of cohesion for the regular profile tests is of little concern. The equations for the resulting curve may be found in the Appendix A4.5, in Table A4.5.2.

As nothing has been changed to confront the disparity between the static and the dynamic data, the mismatch from earlier remains unaddressed. Figure 6.22 is a good step, but it is not perfect. The link between the regular flow and reduced flow regions could be improved. Specifically, by introducing a constant "correction factor" as with the reversed flow. Though in this case, the "correction factor" would have little basis in reality; more work is needed to properly determine the link between dynamic experiments and static experiments. Unfortunately, due to time-constraints, it was not possible to do this analysis for this thesis. The "correction factor" – or, rather more appropriately, the "tweak" – introduced to the static data set is displayed in Figure 6.23 and was calculated using Equation A.8 from Appendix A4.5. The tweak is adjusting the static compressor curve less than $0.5\,\%$ upwards, showing only a minuscule adjustment was needed.

While sounding fairly improvised, a correction factor for the static curve is not necessarily too far fetched. As discussed in Subsection 6.1.2, there is a substantial difference between the different static tests. It could be that a mistake has been made during the experimentation of one of the tests, which

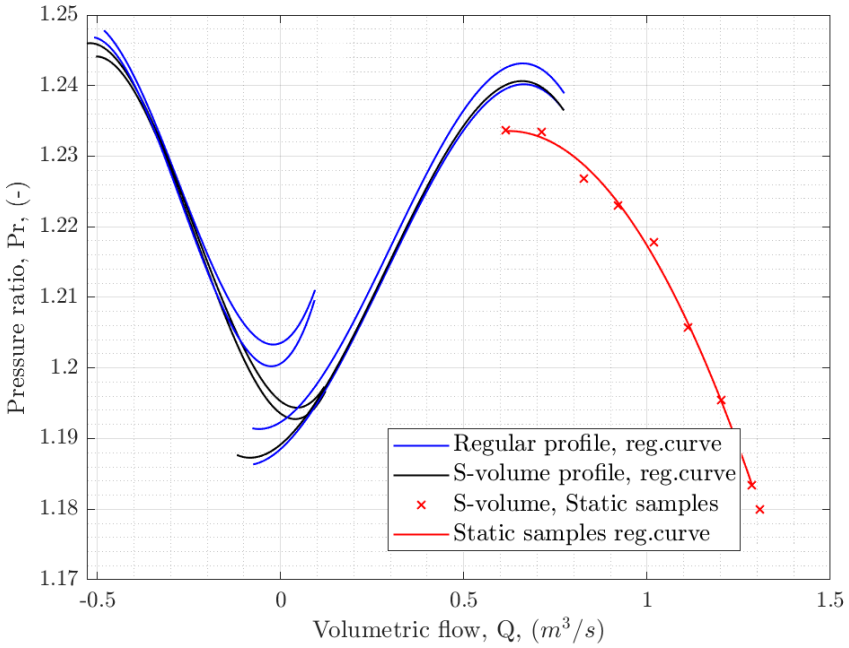

Figure 6.22: Figure 6.20 with the constant correction factor, found in Section 6.1.3, added to the reversed flow region. The regular flow is still a little too low. The curves from the figure are defined in the Appendix in Table A4.5.2.

have not been discovered. If that is the case, more tests would probably discover this. Alternatively, it could be that some parameter that was not analysed impacted the compressor pressure ratio, just enough to disrupt the tests. Whatever the case, there is too little data to say confidently why the regular-, and reduced- curves do not match.

6.3.2 Refining data

In Section 6.2.5, it was mentioned that there was a severely reduced response for some of the "dips" in most regular profile-tests. These dips could be a potential explanation for why the blue curves in Figure 6.22 do not match better with each other.

A quick examination was carried out to determine how much these regions of reduced response affect the scatter plots and in turn the regression curves. Expectations were that the blue curves would diversify, but not dramatically so. Though that statement sounds confident, there were no confident expectations prior to the examinations, as it could conceivably go either way – the reduced flow just limited the fluctuations about zero, or a point close to zero. Removing the low-response dips would therefore remove the somewhat stable parts around zero flow for the regular flow profiles. Predicting how the new regression curves will be shaped with these stable parts gone is not intuitive. Therefore, expectations were not confident. Admittedly, the stable parts were not a good reflection of reality, and consequently the integrity of the data improves when this data is filtered out.

Figure 6.24 is the result of the examination. Here, all dips with low response in reversed and reduced flow-regions have been removed, before the regression curves were calculated, and plotted. The scatter plots that form the basis for these regression curves are shown in Figure A4.5.1 and Figure A4.5.2, in the

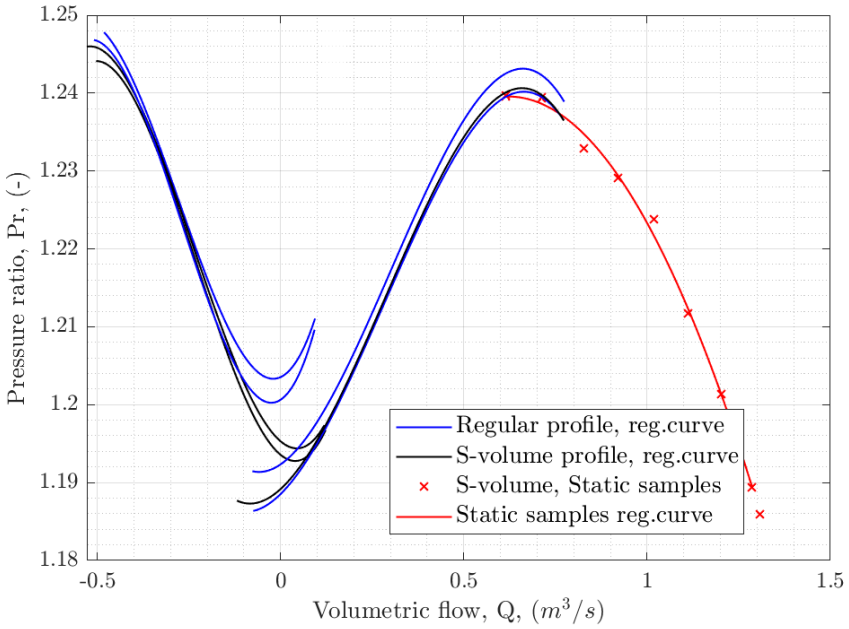

Figure 6.23: Figure 6.22 with a "tweak"-factor added to the normal flow region. The "tweak" factor is displayed in ... . This tweak-factor is a tweak of $\approx 0.5\,\%$ added to all points on the normal curve. The curves from the figure are defined in the Appendix in Table A4.5.3.

Appendix A4.5.

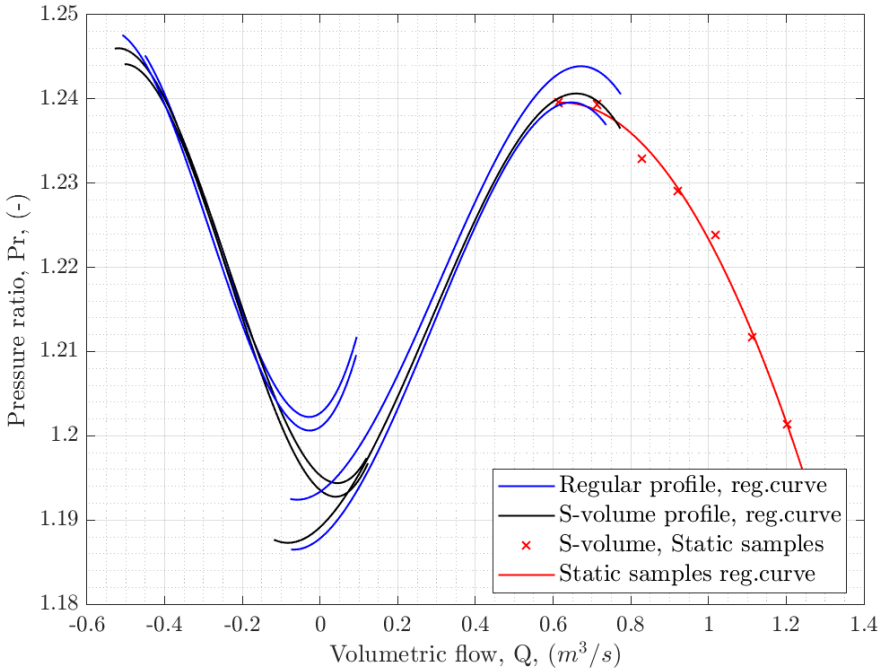

Figure 6.24: Same as Figure 6.23, except data is solely based on "refined data", as described in Section 6.3.2.

6.4 Uncertainty Analysis

This section highlights some of the results from the uncertainty analysis. Only some results are highlighted, because the response is almost the same, irrelevant of profiles and experiment. The main point this section should illustrate is how quickly the uncertainties become too large for most data-analysis based on values near zero flow, and how most analysis lose all meaning if one is only concerned with these uncertainties.

Figure 6.25 shows the relative expanded uncertainty of Q. It should be noted that the data is from a reduced-flow profile, therefore, little data exist for negative values. Consequently, the reversed flow side is not shown well in the figure. However, it is underlined that the uncertainty-signature is mirrored about the y-axis. All other profiles have the same uncertainties for a given Q, which is not surprising, as the conditions were the same. Because of this, only this one figure is shown.

As the figure shows, the relative expanded uncertainties grow fast. This is because the relative expanded uncertainty, U_Q/Q approaches infinity when Q approaches zero. It clearly also shows that while DP25 is the most accurate, DP50 is not too far behind, but DP250 is hopelessly skewed, even long before the unstable area is reached. It has been commented earlier in this thesis, and it is clearly shown here; when $Q < 0.2\,\mathrm{m}^3/\mathrm{s}$, the uncertainties become very large, with DP50's uncertainty surpassing $20\,\%$ near $Q \approx 0.25\,\mathrm{m}^3/\mathrm{s}$. With so high uncertainties, one cannot help but ask whether the creating a continuous compressor curve through this region is at all relevant.

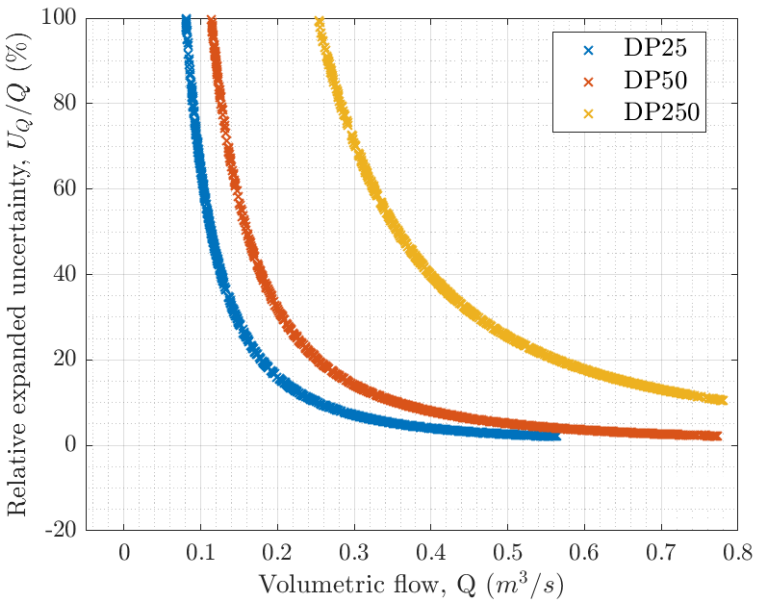

Figure 6.25: Relative expanded uncertainty of Q, for "S-volume", profile 1 from the 05.04 experiments.

However, these uncertainties contain a lot of uncertainty in themselves. And because of the way relative expanded uncertainty is defined, it will always approach infinity when Q approaches zero. Because of this, the analysis breaks down, and cannot be easily used for practical purposes near zero flow.

If one instead focuses on Figure 6.26, which shows the expanded uncertainties instead, it becomes a

bit more understandable. Though, just changing it from a relative expanded case to a relative one is a bit silly, the same problem still remains; this too, makes no sense to do.

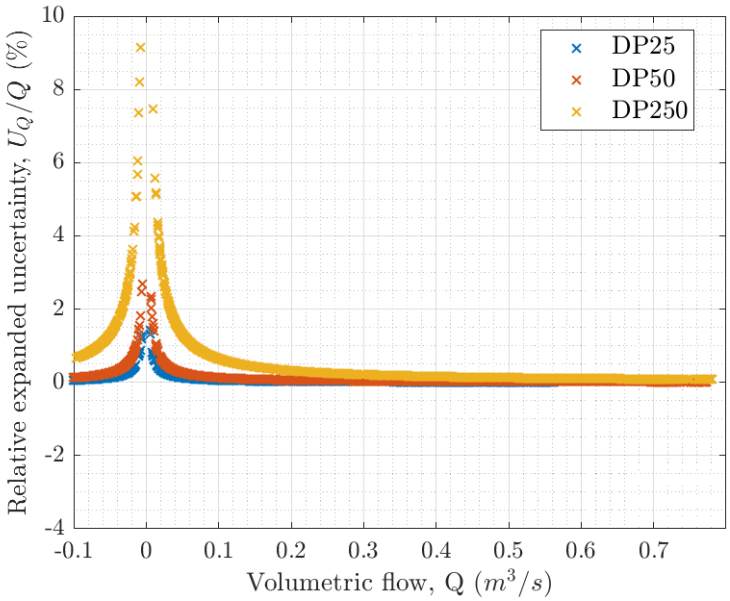

Figure 6.26: Same as Figure 6.25, except this figure shows the expanded uncertainty of Q, and not the relative expanded uncertainty.

Instead, these uncertainties should not really be looked at as an isolated case. They should be seen in context with other sensors, and the overall situation. Yes, the uncertainty of the sensors is such that the volumetric flow could be 100 times higher than the recorded value. Yes, there is no way to be certain of any values recorded near zero. However, it is simply not possible for the flow to rapidly increase to the values shown in Figure 6.26, as the compressor can not go above $Q \approx 1.32\,\mathrm{m}^3/\mathrm{s}$, because that is the choke line.

If one supposes that it is possible for the volumetric flow to suddenly reach this choke-line from complete surge for the argument's sake, then the operators of the compressor would have surely heard it, and shut it down. But, if that too, is disregarded for the argument's sake, one must remember that the operating point of the compressor is limited to following the compressor curve, when the compressor maintains the same speed (which it does in these regions), and the discharge valve is kept steady (which it is, for some time at least). This would then require the conditions which led to surge quickly fixing itself, and returning to regular operation. If this happens, one would move out of the troublesome region, and into a region where it is possible to trust the instruments again.

But none of this happens. Instead, the compressor is following the compressor curve defined in Section 6.3 loosely; with some fluctuations due to the nature of surge, of course. Therefore, developing the compressor line was still very useful, because the compressor follows this line, seemingly despite all the uncertainty of the measurements.

7. Conclusion and Further Work

The long-term ambition of NTNU turbomachinery research is to create a digital twin of their full-scale single-stage centrifugal compressor. This thesis has been one step of many needed to achieve this ambition. Since the digital model was unavailable in time to be validated by this thesis, focus was put on gathering experimental results. Therefore, the primary objective was designed with a purely experimental focus; to create a complete, continuous compressor curve from negative flow to compressor choke. Through the work in this thesis, the primary objective has been achieved with two remarks. First, uncertainties near zero flow are so high, it is not possible to be certain in this region. Second, the static and dynamic parts of the curve did not match immediately; a small tweak had to be made to the static curve.

In order to ensure the validity of this goal, two secondary objectives were also created. The first of the secondary objectives was about evaluating recommendations and standards for flow measurements at transient conditions. This has been done by examining the flow response during transient experiments, comparing results against each of the orifices, and against earlier results. The second of the secondary objectives was to utilise the compressor test rig to validate transient flow measurements. This was achieved through a basic uncertainty analysis, some comparison to earlier experiments, and an in-depth analysis of the different responses for reduced and reversed flow measurements.

There are some other conclusions that can be drawn from the experimental results regarding this thesis. Firstly, it is absolutely essential to use the downstream pressure tank when conducting experiments in the lab, with a volumetric flow $Q < 0.5\,\mathrm{m}^3/\mathrm{s}$. If the tank is not used, especially when analysing surge, deviations from what is considered the "true" compressor path will occur, and instead of a clear frequency and high amplitudes seen in tests with the downstream volume connected, the sensor readings will look more like noise. Another conclusion is that while both orifices match each other rather well for most of the time, they diverge near zero flow. Orifice 1 will hardly measure backflow, even with the downstream pressure tank connected, while the second orifice will fluctuate around zero, just as the theory suggests. It is hard to say which of the two orifices measures "correct" near zero flow. It is easy to imagine the difference is due to the massive volume between the two plates, and both then measure "correct" in their specific region. So, because orifice 2 is much closer to the compressor, it is very likely it reflects the compressor characteristics best. Yet another conclusion is that most measurements where $Q \in (-0.2, 0.2)\ \mathrm{m}^3/\mathrm{s}$ can only be considered suggestive, because the uncertainties are so high.

But there are also some smaller conclusions that can be drawn. One of them is that with the current setup in the laboratory, and the current testing conditions – air at near-atmospheric conditions – the compressor bull-nose is not practically usable for confidently detecting changes in volumetric flow by measuring the DP over the bull nose. Nothing but the most dramatic changes were at all detectable, and then with little indication as to whether flow increased or decreased. Another smaller conclusion is the fact that logging frequency should be at least $10\,\mathrm{Hz}$ for dynamic flows in reduced-, or reversed-flow conditions. Furthermore, another smaller conclusion that can be drawn form the experiments done

is that removing low-response regions from regular profile tests without the downstream pressure tank connected does not seemingly affect results in any substantial way. The last smaller conclusion to be drawn from this thesis, is that it could be beneficial to use as short tubing between the orifice plate and the sensors – particularly the DP-sensors – as is possible, for a more erratic, and expected response during surge. The last of these smaller conclusions is the least definitive of them, because it was felt the work needed to assert the impact of the tubing was not worth it, when the shorter tubing had already replaced the earlier, longer tubing.

7.1 Further work

Since this is only a small step of a larger march, there is a lot more work to be done, before the end goal has been reached. With this in mind, the following list provides some suggestions for ways in which development may be furthered, and the digital model can come one step closer to a digital twin:

- Implement compressor curve in HYSYS dynamics – Requires access to the source code of HYSYS dynamics, either directly, or indirectly. This would be the best way to directly enhance the current dynamic model without much work, as the equations for the curves may be found in the appendix.
- Conduct experiments with $GMF < 1$ – Gather data, prepare extensive analysis, and simulate wet gas experiments. The Matlab code developed for this thesis could also manage this, with some minor tweaks (adding certain constants for the fluid, changing GMF to be calculated dynamically, and not by being a set number).
- Implement direct, two-way communication between the digital model and the experimental laboratory.
- Polytropic and Isentropic analysis – Expand the matlab codes to calculate and report polytropic and isentropic values. This would be the next logical step, after mass flow has been secured.
- Standstill function – Expand the Matlab codes by creating a function in *"TransientResponse_LABEQ"* which automatically reads the relevant standstill file for the current experiment, and adding a correction factor based on the sensor-points in this file automatically. Of course, the user should be notified whenever raw data is changed, like when a correction factor is mixed in.

Bibliography

[1] Harari, Yuval Noah. *Sapiens – A brief history of humankind*. Dvir Publishing House Ltd. (Israel) Random House Harper, 2011.

[2] Åsgard subsea compressors deliver high availability. Offshore Magazine, online article, accessed 05.05.2022. Accessible at https://www.offshore-mag.com/subsea/article/14183945/sgard-subsea-compressors-deliver-high-availability.

[3] Ingrid Schølberg, Morten Hyllseth, Gunleiv Skofteland, and Håvard Nordhus. 'Dynamic analysis of compressor trips in the Snøhvit LNG refrigerant circuits'. 53rd ASME Turbo Expo 2008, Berlin, June 9-13, Vol. 7, pp. 679-688.

[4] Sander Kynell Arstad. Digital Twin Model for Compressor Systems – Project Work. December, 2021, Trondheim, NTNU.

[5] S.L. Dixon and C.A. Hall. Chapter 7 - Centrifugal Pumps, Fans, and Compressors. In S.L. Dixon and C.A. Hall, editors, *Fluid Mechanics and Thermodynamics of Turbomachinery (Seventh Edition)*, pages 265–317. Butterworth-Heinemann, Boston, seventh edition edition, 2014.

[6] John M. Schultz. The Polytropic Analysis of Centrifugal Compressors. *Journal of Engineering for Power*, 84(1):69–82, 01 1962.

[7] L. E. Bakken, *Thermodynamics, compression and expansion processes*, TEP04 – Gas Turbines and Compressors, 2021.

[8] Sigurd Ueland. Digital Compressor Modelling – Project Work, 12 2020.

[9] Martin Bakken. *Transient analysis of wet gas compressor systems*. PhD thesis, Norwegian University of Science and Technology (NTNU), 2019.

[10] Sigurd Ueland. Digital Compressor Modelling – Master's thesis in Mechanical Engineering, 06 2021.

[11] Niketas Choniates. Hysys Unit Operations v10 Reference Guide. Aspen Technology, Inc, June, 2018.

[12] Randen, Erlend. Condition monitoring - Validation of flowmeters, 2021. Master Thesis.

[13] Bakken, Lars E. Bakken, Lars E., Lectures in course *TEP04 – Gas Turbines and Compressors*, attended Autumn of 2021, at NTNU, Trondheim.

[14] CEN Comité Européen de Normalisation (European Committee for Standardization). Measurement of fluid flow by means of pressure differential devices inserted in circular cross-section conduits running full - Part 2: Orifice plates (ISO 5167-2:2003), 2003.

[15] Peter J. Mohr, David B. Newell, Barry N. Taylor, and E. Tiesinga. Uncertainty of Measurement Results. National Institute of Standards and Technology (NIST), Fundamental Physical Constants, online website, accessed 04.03.2022. Accessible at: https://physics.nist.gov/cuu/Uncertainty/index.html.

[16] NIST/SEMATECH e-Handbook of Statistical Methods, https://doi.org/10.18434/M32189, accessed 04.03.2022.

[17] Hogan, Richard. How to Calculate Sensitivity Coefficients for Measurement Uncertainty. ISO budgets, online article, accessed 08.03.2022. Accessible at: https://www.isobudgets.com/how-to-calculate-sensitivity-coefficients-for-measurement-uncertainty/.

[18] S. Gapta, Measurement Uncertainties: Physical parameters and calibration of instruments, Springer, 2012.

[19] G. Steele and H. Coleman, Experimentation, validation, and uncertainty analysis for engineers, John Wiley and sons, 2009.

[20] NEK ISO/IEC GUIDE 98-1, "Uncertainty of measurement - Part 1: Indtroduction to the expression of uncertainty in measurement," Standard Norge, 2009.

[21] *Integrated Wet Gas Compressor Test Facility*, volume 9: Oil and Gas Applications; Supercritical CO2 Power Cycles; Wind Energy of *Turbo Expo: Power for Land, Sea, and Air*, 06 2015.

[22] CEN Comité Européen de Normalisation (European Committee for Standardization). Measurement of fluid flow by means of pressure differential devices inserted in cuircular cross-section conduits running full Part 1: General principles and requirements (ISO 5167-1:2003), 2003.

[23] ESI Technology Limited. Manufacturer of Protran PR3202 DP-sensors. Sensor House, Wrexham Technology Park, Wrexham, LL13 7YP, United Kingdom. Online website: https://www.esi-tec.com/.

[24] Elisa Wilde. How BFSL is related to pressure transducer accuracy, 2015. Automation Products Group, Inc., accessible at https://www.apgsensors.com/about-us/blog/how-bfsl-is-related-to-pressure-transducer-accuracy.

[25] The indispensable experience of Erik Langørgen, the laboratory chief at the NTNU compressor laboratory, and co-supervisor of this thesis.

A. Appendices

A1 Datasheets

A1.1 Protran PR3202

Technical Data

Type:	PR3202	PR3203	PR3204
Sensor Technology:	Piezoresistive Silicon		
Output Signal:	4-20 mA (2 wire)	0-5 V (3 wire)	0-10 V (3 wire)
Supply Voltage:	10-36 VDC	13 – 30 VDC	13 – 30 VDC
Pressure Reference:	Differential		
Protection of Supply Voltage:	Protected against supply voltage reversal up to 50 V		
Standard Pressure Ranges (bar):	0-5 mbar; 0-10 mbar; 0-20 mbar; 0-50 mbar; 0-100 mbar; 0-250 mbar; 0-500 mbar; 0-1,000 mbar (other options available)		
Standard Pressure Ranges (psi):	0-2 inH2O; 0-4 inH2O; 0-8 inH2O; 0-10 inH2O; 0-12 inH2O; 0-20 inH2O; 0-1 psi; 0-1.5 psi; 0-3 psi; 0-4 psi; 0-7.5 psi; 0-15 psi (other options avialable)		
Overpressure Safety:	25 mbar max. for ranges 0-5 mbar to 0-10 mbar; 200 mbar max. for ranges 0-20 mbar to 0-100 mbar; 1,200 mbar max. for ranges 0-150 mbar to 0-1,000 mbar		
Common Mode (Static line pressure):	375 mbar equal to both ports for ranges 0-5 to 0-10 mbar; 2 bar max. equal to both ports for ranges 0-20 mbar to 0-1,000 mbar		
Load Driving Capability:	4-20 mA: RL < [UB - 13 V] / 20 mA (e.g. with supply voltage (UB) of 36 V, max. load (RL) is 1150 Ω)		
Accuracy NLHR:	≤ ±0.3 % of span BFSL		
Zero Offset and Span Tolerance:	±1.0% FS at room temperature ±5% FS (approx.) adjustment via trimming potentiometers located beneath the enclosure lid		
Operating Ambient Temperature:	-20 °C to +70 °C (-4 °F to +158 °F)		
Operating Media Temperature:	-20 °C to +70 °C (-4 °F to +158 °F)		
Storage Temperature:	+5 °C to +40 °C (+41 °F to +104°F) Recommended Best Practice		
Temperature Effects:	±2.0% FS total error band for -20 °C to +70 °C. Typical thermal zero and span coefficients ±0.04% FS/ °C		
ATEX/IECEx Approval Option (4-20 mA version only):	Ex II 1 G Ex ia IIC T4 Ga (zone 0) Ex II 1 D Ex ia IIIC T135 °C Da (zone 20) Ex I M 1 Ex ia I Ma (group 1 M1)	N/A	
ATEX/IECEx Safety Values:	Ui = 28 V Ii = 119 mA Pi = 0.65 W Li = 0.1 µH Ci = 74 nF Temperature Range = -20 °C to +70 °C Max. cable length = 45 m	N/A	
Electromagnetic Compatibility:	Emissions: EN61000-6-3; Immunity: EN61000-6-2; Certification: CE Marked		
Insulation Resistance:	> 100 MΩ @ 50 VDC		
Response time 10-90 %:	1 mS		
Wetted Parts:	Nickel plated brass, silicone tubing, silicon diaphragm, glass filled polyamide		
Pressure Media:	Non-corrosive media such as non-ionic fluids, air and dry gases		
Pressure Connection:	4 mm I.D. hose (other options available)		
Electrical Connection:	Screw terminals for conductor sizes 0.2-2 mm2 are located beneath the enclosure lid. Cable entry is via IP66 cable gland with compression seal for cable sizes 7-10.5 mm		
Net. Weight (Kg):	0.3 Kg		

A1.2 PCE-28

APLISENS®

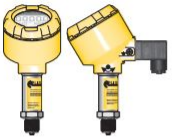

ALW type

ALM type

ALW and ALM type

Aluminum casing with programable local display. The design of the casing enables the use of a local display, rotation of the display, rotation of the casing by 0–345° relative to the sensor. Electrical connection DIN EN 175301-803, IP65 (special verison with cable electrical connection and IP67).

Display with backlight allows to read:
- measured pressure in user units or % of measuring range
- current in output loop in mA

Application and construction

The PCE-28 pressure transmitter is applicable to the measurement of the pressure, underpressure and absolute pressure of gases, vapours and liquids. The active sensing element is a piezoresistant silicon sensor separated from the medium by a diaphragm and by specially selected type of manometric liquid. The electronics is placed in a casing with a degree of protection from IP 65 to IP 68, depending on the type of electrical connection applied.

Calibration

Potentiometers can be used to shift the zero position and the range by up to ±10%, without altering the settings (not possible with ALM and SG casing).

Installation

The transmitter is not heavy, so it can be installed directly on the installation. When the pressure of steam or other hot media is measured, a siphon or impulse line should be used. The needle valve placed upstream the transmitter simplifies installation process and enables the zero point adjustment or the transmitter replacement.
When the special process connections are required for the measurement of levels and pressures (e.g. at food and chemical industries), the transmitter is provided with an Aplisens diaphragm seal. Installing accessories and a full scope of diaphragm seals are described in detail in the further part of the catalogue.

Measurements under explosion hazard

ATEX Intrinsic safety version is available for taking measurements in zones under explosion hazard. The installation of the transmitter in a zone under explosion hazard requires the use of a Ex power supply. We recommend the use of the Aplisens ZS-30/1Ex power supply and separator.

Technical data

Any measuring range 0...25 mbar ÷ 0...1000 bar (over pressure, under pressure); 400 mbar ÷ 80 bar (absolute pressure)
Measurement of lower pressure ranges, possible using transmitter PRE-50G with GP process connection.

	Measuring range				
	25 mbar	100 mbar	400 mbar	0…1 bar ÷ 160bar	0…160 bar ÷ 1000bar
Overpressure Limit (repeated, without hysteresis)	1 bar	1 bar	2,5 bar	4 x range	2 x range; max. 1200 bar
Damaging Overpressure	2 bar	2 bar	5 bar	8 x range; max. 2000 bar	
Accuracy	0,6%	0,3%	0,2% (0,16% - special version)		
Long term stability	0,6% / year	0,2% / year	0,1% / year		
Thermal error	Typically 0,5% / 10°C Max 0,6% / 10°C	Typically 0,3% / 10°C Max 0,4% / 10°C		Typically 0,2% / 10°C Max 0,3% / 10°C	

Hysteresis, repeatability 0,05%
Response time < 120 ms
version TR: < 30 ms
Thermal compensation range -10...80°C
Operating temperature range (ambient temp.) -40...80°C
Medium temperature range -40...130°C

over 130°C – measurement with use an impulse line or diaphragm seals

CAUTION: the medium must not be allowed to freeze in the impulse line or close to the process connection of the transmitter

Output signal 4...20 mA, two wire transmission
0..10V
Material of wetted parts 316Lss, Hastelloy C 276, Au
Material of casing 304ss, 316Lss
Power supply
output 4..20mA
8…36 V DC (Ex 9...28 V DC)
version TR, version Safety: 10,5…36 V DC (Ex 12...28 V DC)
ALW and ALM version: (11…36V DC)
output 0..10V
13…30 VDC
Error due to supply voltage changes 0,005%/ V
Load resistance $R[\Omega] \le \frac{U_{sup}[V] - 8V}{0{,}02A}$

A1.3 Reference Thermometer Model CTP5000, and Precision Thermometer CTR5000

Specifications	Model CTP5000-200
Specific probe data [1]	
Temperature range	-50 … +200 °C [-58 ... +392 °F]
Resistance at 0 °C [32 °F]	100 Ω
Temperature coefficient	0.00385
R(Ga)/R(TPW)	Ratio less than 1.11807
Annual drift [2]	±10 ... ±20 mK
Recommended measurement current	0.5 mA or 1 mA
Self heating error in water at 0 °C [32 °F]	2 ... 5 mK
Sheath material	Stainless steel
Dimensions	
Probe diameter	d = 3 mm [0.12 in]
Probe length	l = 30 mm [1.18 in], fully immersible
Cable	
Length	3 m [9.84 ft]
Connection	Bare wire, DIN plug or SMART connector

1) Specifications may deviate; they depend on the use of the thermometer. The specified values are typical values for use in laboratories.
2) Previous ageing is required. Recommendation = T_{max} + 10 K over 20 h

Specifications
Model CTR5000

Hand-held thermometer	
Probe types	Industrial platinum resistance thermometers (PRTs) and standard platinum resistance thermometers (SPRTs) with R_0 = 25 Ω and 100 Ω up to an alpha of 0.00392
Measuring inputs	2 (front panel), 4 or 6 (rear panel) Expandable up to an additional 64 channels with CTS5000 multiplexers
Data entry format	ITS 90 and CVD for calibrated probes; or EN 60751 for uncalibrated probes Optional: coefficient generation from data pairs
Measuring ranges	
Probe current	1 mA (Pt100); optional auto-select 1 mA, 2 mA
Temperature range	-200 ... +962 °C, depending on thermometer probe
Accuracy [1]	0.01 K, optional 0.005 K

1) The accuracy in K defines the deviation between the measured value and the reference value. (Only valid for indicating instruments.)

A2 Sensitivity coefficients

This section contains some sensitivity coefficients from the uncertainty analysis, that was left out of the main text to save space, and because they are not very relevant; the process for calculating them is the same, always.

Equation A.1a and Equation A.1b are sensitivity coefficients for β.

$$\frac{\partial \beta}{\partial d} = \frac{1}{D} \tag{A.1a}$$

$$\frac{\partial \beta}{\partial D} = \frac{-d}{D^2} \tag{A.1b}$$

Equation A.2 show the sensitivity coefficients for the expansibility factor ϵ.

$$\frac{\partial \epsilon}{\partial \beta} = 7.440\ (0.138 \cdot \beta^3 + 0.138 \cdot \beta^7)\ \left(\left(1 - \frac{\Delta p}{p_1} \right)^{1/\kappa} - 1 \right) \tag{A.2a}$$

$$\frac{\partial \epsilon}{\partial p_1} = \frac{(0.351 + 0.256\ \beta^4 + 0.93\beta^8)\ \Delta p\ \left(1 - \frac{\Delta p}{p_1} \right)^{1/\kappa}}{\kappa\ p_1\ (p_1 - \Delta p)} \tag{A.2b}$$

$$\frac{\partial \epsilon}{\partial \Delta p} = -\frac{(0.351 + 0.256\beta^4 + 0.93\beta^8)\ \left(1 - \frac{\Delta p}{p_1} \right)^{\frac{1}{\kappa - 1}}}{\kappa\ p_1} \tag{A.2c}$$

Equation A.3 show the sensitivity coefficients for the discharge coefficient C.

$$\frac{\partial C}{\partial \beta} = 0.0522\ \beta - 1.728\ \beta^7 + 3.647 \cdot 10^{-4} \beta^{-0.3}\ \left(\frac{10^6}{Re_D} \right)^{0.7} + (0.0658 + 0.0221\ A)\ \beta^{2.5} \left(\frac{10^6}{Re_D} \right)^{0.3} \tag{A.3a}$$

$$\frac{\partial C}{\partial D} = 0 \tag{A.3b}$$

$$\frac{\partial C}{\partial Re_D} = -3.6470 \cdot 10^{-4}\ \left(10^6\ \beta \right)^{0.7} Re_D^{-1.7} - (0.0056 + 0.0019\ A)\ \beta^{3.5}\ (10^6)^{0.3}\ Re_D^{-1.3} \tag{A.3c}$$

where the A and other parameters are defined in Section 2.2.1. Since the sensitivity coefficient in Equation A.3b is zero, that element falls away from Equation 4.9, and Equation 4.9 simplifies to Equation A.4.

$$U_C = \kappa \sqrt{\left(\frac{U_\beta}{\kappa} \frac{\partial C}{\partial \beta} \right)^2 + \left(\frac{U_{Re_D}}{\kappa} \frac{\partial C}{\partial Re_D} \right)^2 + \left(0.5\ C\ \frac{1}{\kappa}\ \frac{1}{100} \right)^2} \tag{A.4}$$

A3 Automatic Data-Cleaner – Matlab script

This section contains a description from the project work [4], about the automatic data-cleaner function, reiterated here.

As mentioned before, the Matlab code created for the project work features an automatic function for removing experimental data that is clearly faulty. There is a very fine line one must walk when starting to discriminate experimental data, so much care must be taken when doing this. Especially as the altered data was used for further calculations, while the raw data was not.

Figure A3.0.1 shows the experimental raw-data obtained during one of the transient tests. Notice how five temperature recordings from temperature sensor 16 suddenly jump a couple of degrees before returning to near-previous values. None of the other sensors recorded any similar behaviour, suggesting that this is just a quirk.

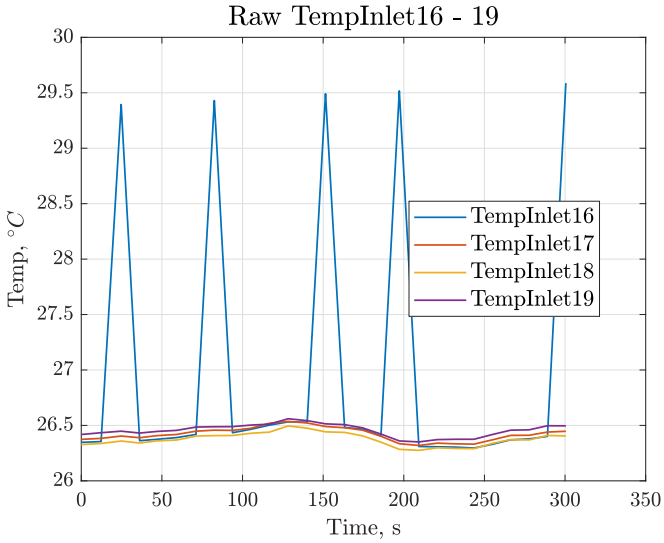

Figure A3.0.1: Showing the unedited, *raw*-data obtained for the experiment where the discharge valve was slowly closed and reopened.

The data-cleaning function also noticed these spikes and produced Figure A3.0.2 as a result. At first glance it does not look much better, but the y-axis in the plot shows that the entire variation observed in the figure is well within 0.5 °C, the same as the rest of the data points seen in Figure A3.0.1.

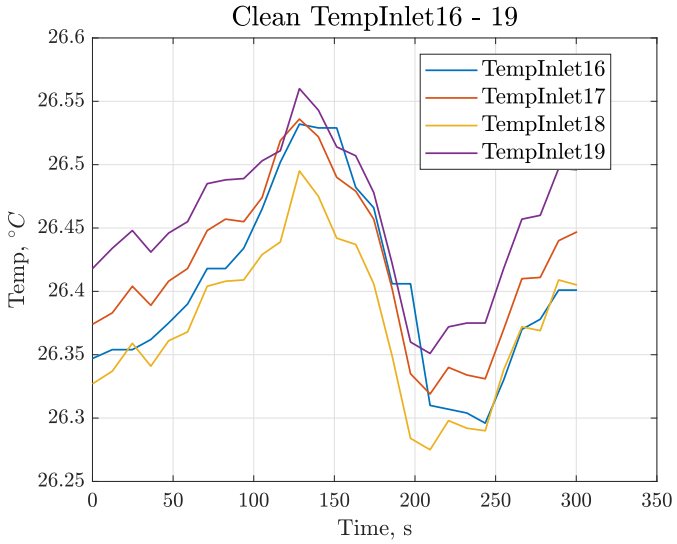

Figure A3.0.2: Showing the edited, *cleaned*-data obtained for the experiment where the discharge valve was slowly closed and reopened.

The cleaning-function works by looking for variations higher than a certain level, determined by the user, in a vector containing all data measured by one sensor. When a variation exceeding the limit specified is found, it is set to the same as the previous recorded data value. In the case mentioned above for example, the cleaning-function found those five points to be more than 2 °C different from the

previous value, and they were promptly removed.

This function is not without weaknesses, and therefore both the raw and the clean data plots will be shown when a cleaning operation has taken place. Additionally, an output message will mention where data points were removed, along with how many. That way, the user will always be the one to make the final call to remove some, or keep all data. It is also always possible to change the criteria for removing data, or disable the function completely.

A4 Selected experimental data

This section contains some selected experimental data that might be interesting to look at for further details, but which ultimately are not as relevant.

A4.1 Static, reduced flow

This section includes some extra data from static experiments concerning reduced flow. In particular, Table A4.1.1 summarises one of the later experiments where the entirety of the compressor curve was mapped, with the downstream pressure tank volume connected. The table shows the average values of the samples, taken over a period of at least $50\,\mathrm{s}$. Because of the wide range, many sensors were at some point saturated, and therefore a varying amount of sensors was used to map the average response. Care was taken so that saturated sensors were excluded from the data presented in the table. Figure 6.3a from subsection 6.1.2 shows a figure where the data from the table was used. The disparity was calculated using Equation A.5.

Q			**Pr**	**Disparity**	**Sensors used**	
Average	**Orifice 1**	**Orifice 2**	(p_2/p_1)	**(%)**	**Orifice 1**	**Orifice 2**
1.2858	1.2512	1.3203	1.1834	-5.24	DP250, DP smar	DP250
1.3087	1.2715	1.3460	1.1799	-5.54	-	-
1.2025	1.1760	1.2289	1.1954	-4.31	-	-
1.0175	1.0036	1.0315	1.2178	-2.71	-	DP250, DP smar
1.1123	1.0961	1.1285	1.2057	-2.88	-	-
0.9198	0.9128	0.9268	1.2231	-1.51	-	-
0.8283	$0,8231$	$0,8335$	$1,2269$	$-1,25$	All sensors available	-
0.7134	0.7144	0.7123	1.2334	0.30	-	DP250, DP smar, DP50
0.6142	0.6194	0.6090	1.2337	1.67	-	-
0.5137	0.5225	0.5049	1.2268	3.36	-	All sensors available
0.3960	0.4082	0.3838	1.2169	5.97	-	-
0.2811	0.3025	0.2598	1.2053	14.12	-	-
0.0448	0.1021	-0.0126	1.1798	112.32	-	-
0.0567	0.1118	0.0016	1.1800	98.53	-	-

Table A4.1.1: Showing the average values of static samples taken over a time period of at least $50\,\mathrm{s}$. The experiment was conducted with the downstream pressure tank connected. The disparity is in $\%$, and was calculated using Equation A.5. The line in the *sensors used*-columns indicate the statement above the line was true for the test. Not all sensors were used at all times, because they were saturated, and would skew the results unnecessary.

$$Disparity = \frac{Q_{orifice\ 1} - Q_{orifice\ 2}}{MAX(Q_{orifice\ 1}, Q_{orifice\ 2})} \tag{A.5}$$

The max-function in Equation A.5 uses the maximum value of the two elements.

A4.2 Static, reversed flow

Equation A.6a was used to find the average relative disparity (in %) for the constant correction factor. Since the average of Q_{Or1} provided the largest factor, and was the same value, independent of the correction factor used, it was selected for calculating the relative disparity. Indeed, it was after all the average disparity from orifice 1 that was examined anyways. Similarly, Equation A.6b was used for the same purpose and in the same way, but using the equation for the linear correction factor instead.

$$Disp._{constant} = \frac{average(Q_{Or1} + Q_{Or2} - C_{lin})}{average(Q_{Or1})} \cdot 100\% \tag{A.6a}$$

$$Disp._{linear} = \frac{average(Q_{Or1} - Q_{Or2}\, C_{const}}{average(Q_{Or1})} \cdot 100\% \tag{A.6b}$$

A4.3 Dynamic, Bull nose

Figure A4.3.1 illustrates that the bull nose did not provide a clear enough signature to be easily understood. As the figure text says, it is easier to see surge and a change in operating condition by looking at the shaft speed, than the bull nose DP.

Figure A4.3.2 shows that the pattern seen in the bull nose response seems to be repeated across the compressor. Albeit this ”repetition” is a lot clearer, with more distinct ”ups and downs”, and differences in general. It is therefore better to use the pressure difference across the compressor, than trying to see sense through the distortion of the bull nose.

A4.4 Dynamic, reduced flow

More examples of the low response can be seen in Figure A4.4.1, and Figure A4.4.2. The first shows the responses of the DP25 and DP250 sensors for the second profile recorded for reduced flow, the second shows the plots of the DP50 sensor from both profiles.

A4.5 Complete compressor profile

In this subsection, tables with equations describing all the regression curves in the different *“complete compressor profile”*-plots can be found. Using Equation A.7 and inserting the equation parameters from the tables will give a function for the curves from the figures in Section 6.3.

$$y = p_1 \cdot x^3 + p_2 \cdot x^2 + p_3 \cdot x + p_4 \tag{A.7}$$

The *“tweak”*-factor mentioned in Section 6.3 is used to change the raw data for the compressor pressure ratio into a value that is more inline with the response from the dynamic tests. The factor was

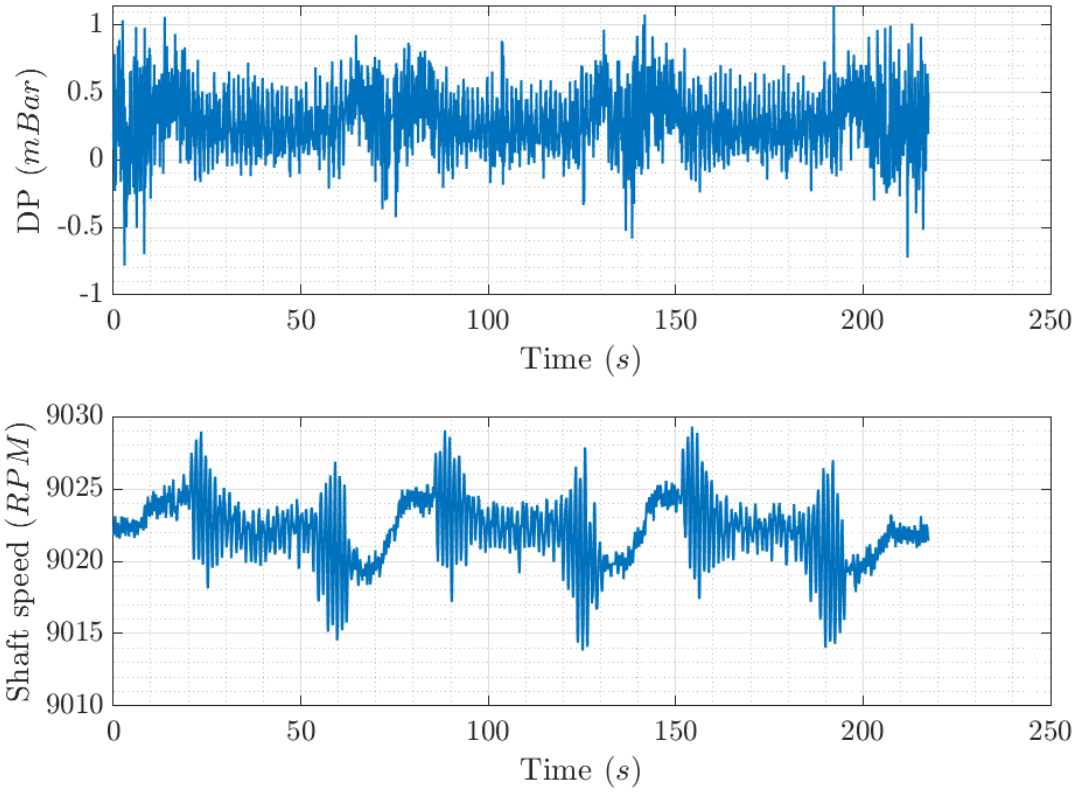

Figure A4.3.1: Top plot showing the differential pressure recorded in a typical profile test with a pressure tank connected to simulate large downstream volume. Lower plot showing the RPM of the compressor shaft speed. Interestingly, it is easier to see surge and a change in operating condition by looking at the shaft speed, than the bull nose DP.

estimated by eye, and is not meant to be very accurate, as it is just arbitrarily added. How it is used, along with its value is shown in Equation A.8.

$$Pr_{new} = Pr_{raw} + C_{tweak}, \qquad \Rightarrow C_{tweak} = 0.006\,\mathrm{m}^3/\mathrm{s} \tag{A.8}$$

Figure A4.5.1 is a scatter plot exactly the same as Figure 6.15, but with “refined data”. Refined data is discussed in Section 6.3.2.

Figure A4.5.2 is a scatter plot exactly the same as Figure 6.19, but with “refined data”. Refined data is discussed in Section 6.3.2. Notice the small differences between Figure A4.5.2 and Figure 6.19.

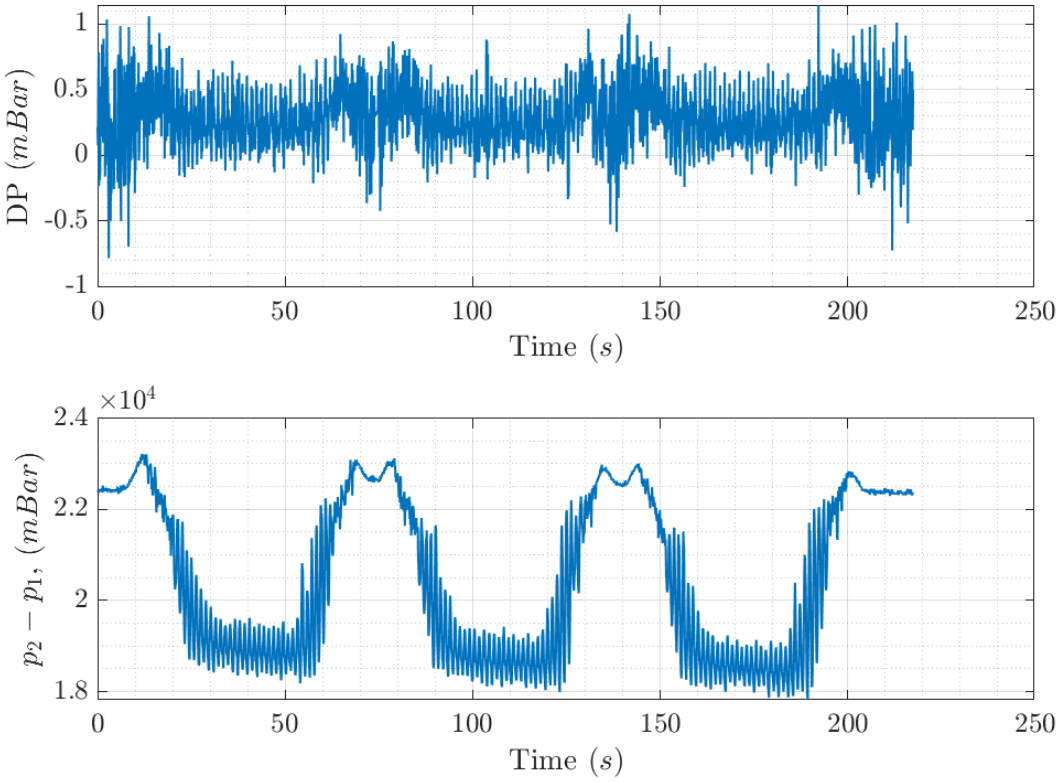

Figure A4.3.2: Upper plot showing the differential pressure recorded in a typical profile test with a pressure tank connected to simulate a large downstream volume. Lower plot shows the differential pressure over the compressor (outlet − inlet). It seems the upper plot is a distorted and scaled-down version of the lower plot.

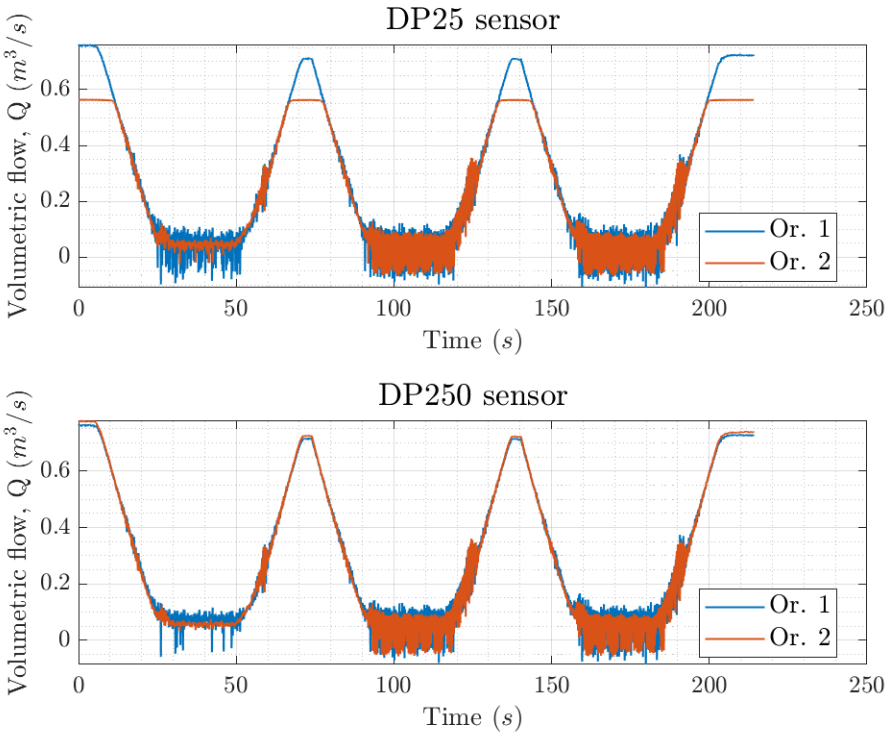

Figure A4.4.1: Another example of low response. Here, the first dip has a lower response.

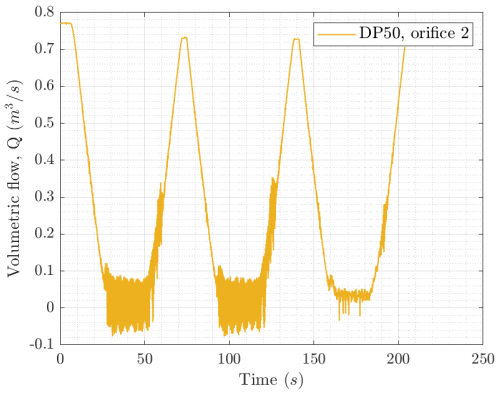

(a) Profile 1, low response.

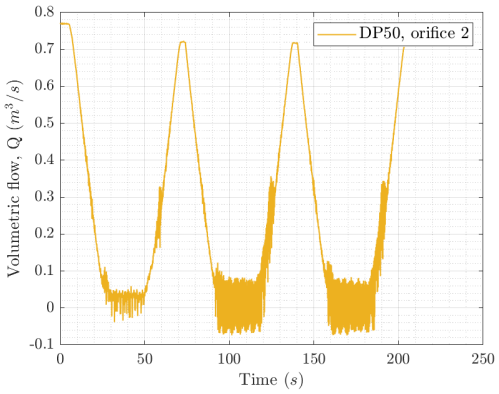

(b) Profile 2, low response.

Figure A4.4.2: More examples of low response. Showing that all DP sensors experience the same lowered response. It is not an isolated sensor that reports this.

From region	Type	Equation parameters
Reversed flow	Regular profile	$p_1 = 0.6679;\ p_2 = 0.5571;\ p_3 = 0.0260;\ p_4 = 1.1726$
	S-volume	$p_1 = 0.6089;\ p_2 = 0.4277;\ p_3 = -0.03948;\ p_4 = 1.1650$
Reduced flow	Regular profile	$p_1 = -0.2634;\ p_2 = 0.2321;\ p_3 = 0.0393;\ p_4 = 1.1904$
	S-volume	$p_1 = -0.2611;\ p_2 = 0.2255;\ p_3 = 0.0430;\ p_4 = 1.189$
Regular flow	Static profile	$p_1 = 0;\ p_2 = -0.1303;\ p_3 = 0.1784;\ p_4 = 1.1697$

Table A4.5.1: Equation A.7 must be used with the *"equation parameters"*. This table describes the average of the different type of curves curves from Figure 6.20.

From region	Type	Equation parameters
Reversed flow	Regular profile	$p_1 = 0.6679;\ p_2 = 0.5571;\ p_3 = 0.0260;\ p_4 = 1.2021$
	S-volume	$p_1 = 0.6089;\ p_2 = 0.4277;\ p_3 = -0.03948;\ p_4 = 1.1944$
Reduced flow	Regular profile	$p_1 = -0.2634;\ p_2 = 0.2321;\ p_3 = 0.0393;\ p_4 = 1.1904$
	S-volume	$p_1 = -0.2611;\ p_2 = 0.2255;\ p_3 = 0.0430;\ p_4 = 1.189$
Regular flow	Static profile	$p_1 = 0;\ p_2 = -0.1303;\ p_3 = 0.1784;\ p_4 = 1.1697$

Table A4.5.2: Equation A.7 must be used with the *"equation parameters"*. This table describes the average of the different type of curves curves from Figure 6.22.

From region	Type	Equation parameters
Reversed flow	Regular profile	$p_1 = 0.6679;\ p_2 = 0.5571;\ p_3 = 0.0260;\ p_4 = 1.2021$
	S-volume	$p_1 = 0.6089;\ p_2 = 0.4277;\ p_3 = -0.03948;\ p_4 = 1.1944$
Reduced flow	Regular profile	$p_1 = -0.2634;\ p_2 = 0.2321;\ p_3 = 0.0393;\ p_4 = 1.1904$
	S-volume	$p_1 = -0.2611;\ p_2 = 0.2255;\ p_3 = 0.0430;\ p_4 = 1.189$
Regular flow	Static	$p_1 = 0;\ p_2 = -0.1303;\ p_3 = 0.1784;\ p_4 = 1.1757$

Table A4.5.3: Equation A.7 must be used with the *"equation parameters"*. This table describes the average of the different type of curves curves from Figure 6.23.

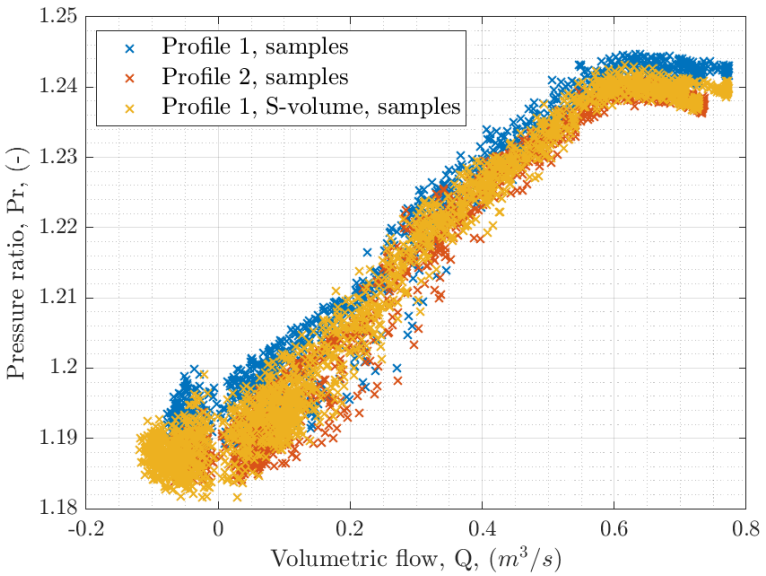

Figure A4.5.1: Scatter plot showing the data points recorded for reduced flow. This scatter plot contains refined data; that is, the "dips" with reduced response, mentioned in Section 6.2.5 has been removed.

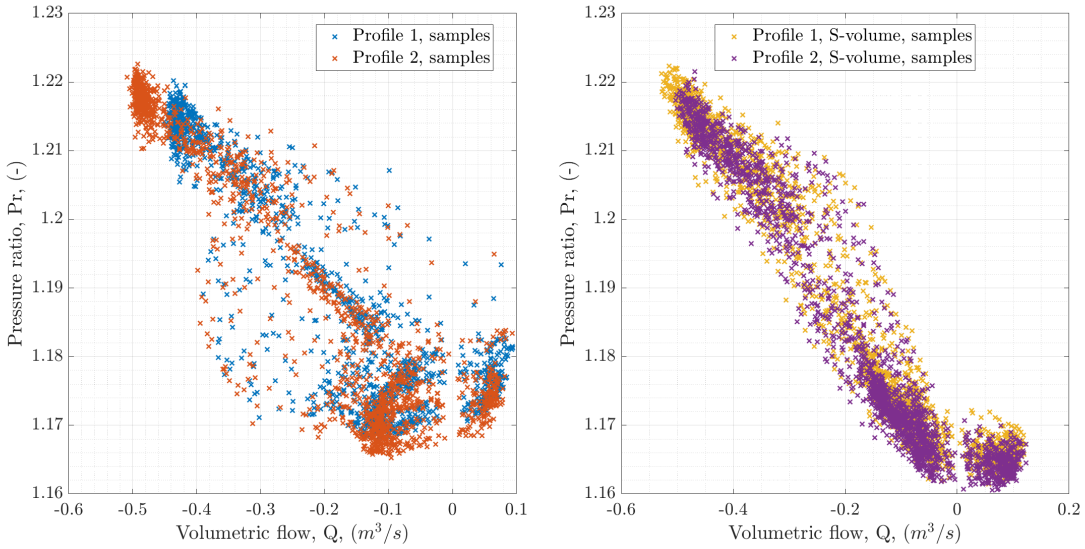

Figure A4.5.2: Scatter plot showing the data points recorded for reversed flow. The figure shows the two regular profile tests on the left, and two "S-volume" tests on the right. This scatter plot contains refined data; that is, the "dips" with reduced response, mentioned in Section 6.2.5 has been removed.

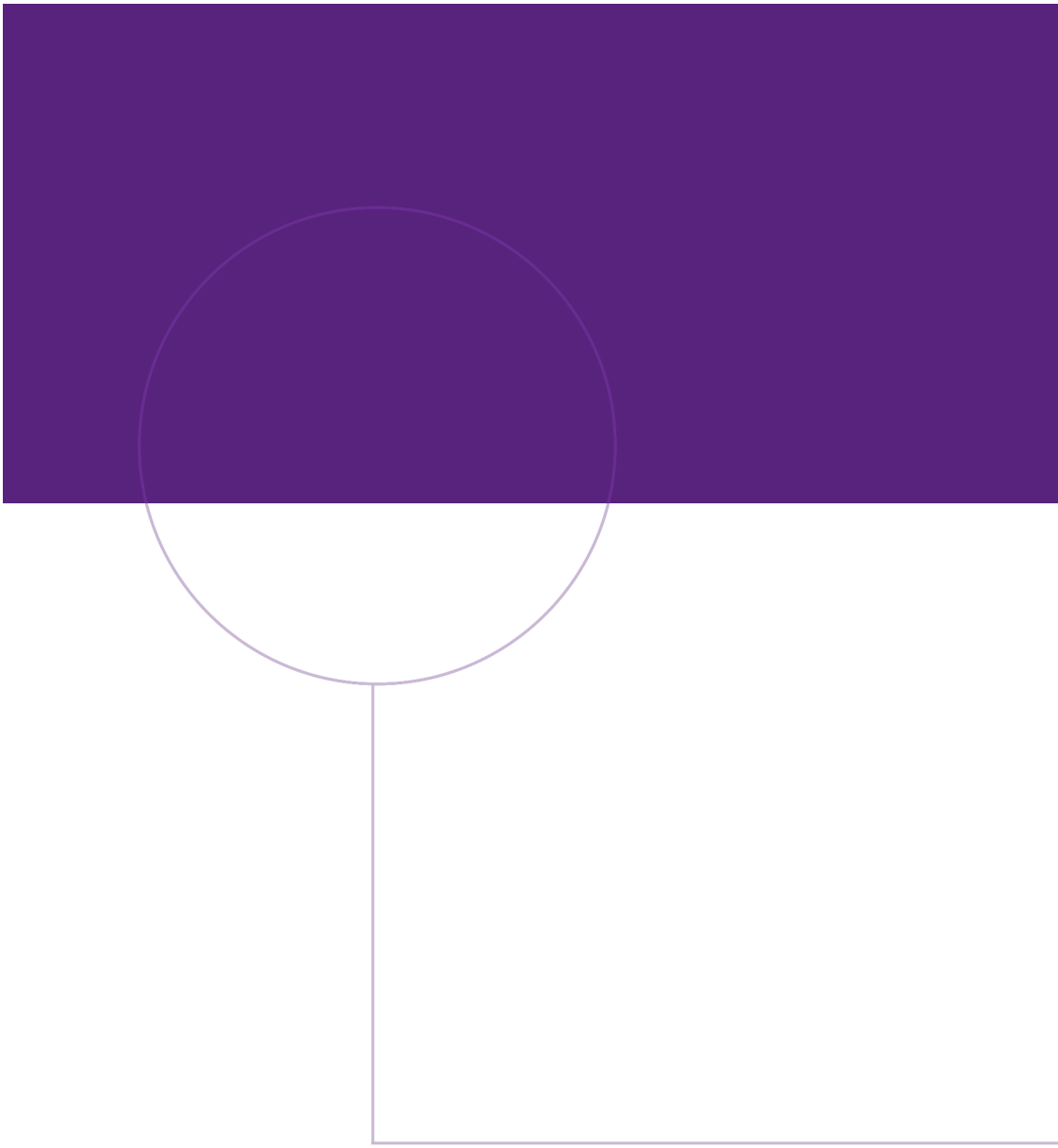

NTNU

Norwegian University of
Science and Technology